

# International Journal of Physical Sciences

Volume 8 Number 32 30 August, 2013

ISSN 1992-1950



*Academic  
Journals*

## ABOUT IJPS

The **International Journal of Physical Sciences (IJPS)** is published weekly (one volume per year) by Academic Journals.

**International Journal of Physical Sciences (IJPS)** is an open access journal that publishes high-quality solicited and unsolicited articles, in English, in all Physics and chemistry including artificial intelligence, neural processing, nuclear and particle physics, geophysics, physics in medicine and biology, plasma physics, semiconductor science and technology, wireless and optical communications, materials science, energy and fuels, environmental science and technology, combinatorial chemistry, natural products, molecular therapeutics, geochemistry, cement and concrete research, metallurgy, crystallography and computer-aided materials design. All articles published in IJPS are peer-reviewed.

## Submission of Manuscript

Submit manuscripts as e-mail attachment to the Editorial Office at: [ijps@academicjournals.org](mailto:ijps@academicjournals.org). A manuscript number will be mailed to the corresponding author shortly after submission.

For all other correspondence that cannot be sent by e-mail, please contact the editorial office (at [ijps@academicjournals.org](mailto:ijps@academicjournals.org)).

The International Journal of Physical Sciences will only accept manuscripts submitted as e-mail attachments.

Please read the **Instructions for Authors** before submitting your manuscript. The manuscript files should be given the last name of the first author.

## Editors

### **Prof. Sanjay Misra**

*Department of Computer Engineering, School of Information and Communication Technology  
Federal University of Technology, Minna,  
Nigeria.*

### **Prof. Songjun Li**

*School of Materials Science and Engineering,  
Jiangsu University,  
Zhenjiang,  
China*

### **Dr. G. Suresh Kumar**

*Senior Scientist and Head Biophysical Chemistry  
Division Indian Institute of Chemical Biology  
(IICB)(CSIR, Govt. of India),  
Kolkata 700 032,  
INDIA.*

### **Dr. Remi Adewumi Oluyinka**

*Senior Lecturer,  
School of Computer Science  
Westville Campus  
University of KwaZulu-Natal  
Private Bag X54001  
Durban 4000  
South Africa.*

### **Prof. Hyo Choi**

*Graduate School  
Gangneung-Wonju National University  
Gangneung,  
Gangwondo 210-702, Korea*

### **Prof. Kui Yu Zhang**

*Laboratoire de Microscopies et d'Etude de  
Nanostructures (LMEN)  
Département de Physique, Université de Reims,  
B.P. 1039. 51687,  
Reims cedex,  
France.*

### **Prof. R. Vittal**

*Research Professor,  
Department of Chemistry and Molecular  
Engineering  
Korea University, Seoul 136-701,  
Korea.*

### **Prof Mohamed Bououdina**

*Director of the Nanotechnology Centre  
University of Bahrain  
PO Box 32038,  
Kingdom of Bahrain*

### **Prof. Geoffrey Mitchell**

*School of Mathematics,  
Meteorology and Physics  
Centre for Advanced Microscopy  
University of Reading Whiteknights,  
Reading RG6 6AF  
United Kingdom.*

### **Prof. Xiao-Li Yang**

*School of Civil Engineering,  
Central South University,  
Hunan 410075,  
China*

### **Dr. Sushil Kumar**

*Geophysics Group,  
Wadia Institute of Himalayan Geology,  
P.B. No. 74 Dehra Dun - 248001(UC)  
India.*

### **Prof. Suleyman KORKUT**

*Duzce University  
Faculty of Forestry  
Department of Forest Industrial Engineering  
Beciyorukler Campus 81620  
Duzce-Turkey*

### **Prof. Nazmul Islam**

*Department of Basic Sciences &  
Humanities/Chemistry,  
Techno Global-Balurghat, Mangalpur, Near District  
Jail P.O: Beltalpark, P.S: Balurghat, Dist.: South  
Dinajpur,  
Pin: 733103,India.*

### **Prof. Dr. Ismail Musirin**

*Centre for Electrical Power Engineering Studies  
(CEPES), Faculty of Electrical Engineering, Universiti  
Teknologi Mara,  
40450 Shah Alam,  
Selangor, Malaysia*

### **Prof. Mohamed A. Amr**

*Nuclear Physic Department, Atomic Energy Authority  
Cairo 13759,  
Egypt.*

### **Dr. Armin Shams**

*Artificial Intelligence Group,  
Computer Science Department,  
The University of Manchester.*

## Editorial Board

**Prof. Salah M. El-Sayed**

*Mathematics. Department of Scientific Computing,  
Faculty of Computers and Informatics,  
Benha University. Benha ,  
Egypt.*

**Dr. Rowdra Ghatak**

*Associate Professor  
Electronics and Communication Engineering Dept.,  
National Institute of Technology Durgapur  
Durgapur West Bengal*

**Prof. Fong-Gong Wu**

*College of Planning and Design, National Cheng Kung  
University  
Taiwan*

**Dr. Abha Mishra.**

*Senior Research Specialist & Affiliated Faculty.  
Thailand*

**Dr. Madad Khan**

*Head  
Department of Mathematics  
COMSATS University of Science and Technology  
Abbottabad, Pakistan*

**Prof. Yuan-Shyi Peter Chiu**

*Department of Industrial Engineering & Management  
Chaoyang University of Technology  
Taichung, Taiwan*

**Dr. M. R. Pahlavani,**

*Head, Department of Nuclear physics,  
Mazandaran University,  
Babolsar-Iran*

**Dr. Subir Das,**

*Department of Applied Mathematics,  
Institute of Technology, Banaras Hindu University,  
Varanasi*

**Dr. Anna Oleksy**

*Department of Chemistry  
University of Gothenburg  
Gothenburg,  
Sweden*

**Prof. Gin-Rong Liu,**

*Center for Space and Remote Sensing Research  
National Central University, Chung-Li,  
Taiwan 32001*

**Prof. Mohammed H. T. Qari**

*Department of Structural geology and remote sensing  
Faculty of Earth Sciences  
King Abdulaziz UniversityJeddah,  
Saudi Arabia*

**Dr. Jyhwen Wang,**

*Department of Engineering Technology and Industrial  
Distribution  
Department of Mechanical Engineering  
Texas A&M University  
College Station,*

**Prof. N. V. Sastry**

*Department of Chemistry  
Sardar Patel University  
Vallabh Vidyanagar  
Gujarat, India*

**Dr. Edilson FERNEDA**

*Graduate Program on Knowledge Management and IT,  
Catholic University of Brasilia,  
Brazil*

**Dr. F. H. Chang**

*Department of Leisure, Recreation and Tourism  
Management,  
Tzu Hui Institute of Technology, Pingtung 926,  
Taiwan (R.O.C.)*

**Prof. Annapurna P.Patil,**

*Department of Computer Science and Engineering,  
M.S. Ramaiah Institute of Technology, Bangalore-54,  
India.*

**Dr. Ricardo Martinho**

*Department of Informatics Engineering, School of  
Technology and Management, Polytechnic Institute of  
Leiria, Rua General Norton de Matos, Apartado 4133, 2411-  
901 Leiria,  
Portugal.*

**Dr Driss Miloud**

*University of mascara / Algeria  
Laboratory of Sciences and Technology of Water  
Faculty of Sciences and the Technology  
Department of Science and Technology  
Algeria*

# Instructions for Author

**Electronic submission** of manuscripts is strongly encouraged, provided that the text, tables, and figures are included in a single Microsoft Word file (preferably in Arial font).

The **cover letter** should include the corresponding author's full address and telephone/fax numbers and should be in an e-mail message sent to the Editor, with the file, whose name should begin with the first author's surname, as an attachment.

## Article Types

Three types of manuscripts may be submitted:

**Regular articles:** These should describe new and carefully confirmed findings, and experimental procedures should be given in sufficient detail for others to verify the work. The length of a full paper should be the minimum required to describe and interpret the work clearly.

**Short Communications:** A Short Communication is suitable for recording the results of complete small investigations or giving details of new models or hypotheses, innovative methods, techniques or apparatus. The style of main sections need not conform to that of full-length papers. Short communications are 2 to 4 printed pages (about 6 to 12 manuscript pages) in length.

**Reviews:** Submissions of reviews and perspectives covering topics of current interest are welcome and encouraged. Reviews should be concise and no longer than 4-6 printed pages (about 12 to 18 manuscript pages). Reviews are also peer-reviewed.

## Review Process

All manuscripts are reviewed by an editor and members of the Editorial Board or qualified outside reviewers. Authors cannot nominate reviewers. Only reviewers randomly selected from our database with specialization in the subject area will be contacted to evaluate the manuscripts. The process will be blind review.

Decisions will be made as rapidly as possible, and the journal strives to return reviewers' comments to authors as fast as possible. The editorial board will re-review manuscripts that are accepted pending revision. It is the goal of the IJPS to publish manuscripts within weeks after submission.

## Regular articles

All portions of the manuscript must be typed double-spaced and all pages numbered starting from the title page.

**The Title** should be a brief phrase describing the contents of the paper. The Title Page should include the authors' full names and affiliations, the name of the corresponding author along with phone, fax and E-mail information. Present addresses of authors should appear as a footnote.

**The Abstract** should be informative and completely self-explanatory, briefly present the topic, state the scope of the experiments, indicate significant data, and point out major findings and conclusions. The Abstract should be 100 to 200 words in length. Complete sentences, active verbs, and the third person should be used, and the abstract should be written in the past tense. Standard nomenclature should be used and abbreviations should be avoided. No literature should be cited.

Following the abstract, about 3 to 10 key words that will provide indexing references should be listed.

A list of non-standard **Abbreviations** should be added. In general, non-standard abbreviations should be used only when the full term is very long and used often. Each abbreviation should be spelled out and introduced in parentheses the first time it is used in the text. Only recommended SI units should be used. Authors should use the solidus presentation (mg/ml). Standard abbreviations (such as ATP and DNA) need not be defined.

**The Introduction** should provide a clear statement of the problem, the relevant literature on the subject, and the proposed approach or solution. It should be understandable to colleagues from a broad range of scientific disciplines.

**Materials and methods** should be complete enough to allow experiments to be reproduced. However, only truly new procedures should be described in detail; previously published procedures should be cited, and important modifications of published procedures should be mentioned briefly. Capitalize trade names and include the manufacturer's name and address. Subheadings should be used. Methods in general use need not be described in detail.

**Results** should be presented with clarity and precision.

The results should be written in the past tense when describing findings in the authors' experiments. Previously published findings should be written in the present tense. Results should be explained, but largely without referring to the literature. Discussion, speculation and detailed interpretation of data should not be included in the Results but should be put into the Discussion section.

**The Discussion** should interpret the findings in view of the results obtained in this and in past studies on this topic. State the conclusions in a few sentences at the end of the paper. The Results and Discussion sections can include subheadings, and when appropriate, both sections can be combined.

**The Acknowledgments** of people, grants, funds, etc should be brief.

**Tables** should be kept to a minimum and be designed to be as simple as possible. Tables are to be typed double-spaced throughout, including headings and footnotes. Each table should be on a separate page, numbered consecutively in Arabic numerals and supplied with a heading and a legend. Tables should be self-explanatory without reference to the text. The details of the methods used in the experiments should preferably be described in the legend instead of in the text. The same data should not be presented in both table and graph form or repeated in the text.

**Figure legends** should be typed in numerical order on a separate sheet. Graphics should be prepared using applications capable of generating high resolution GIF, TIFF, JPEG or Powerpoint before pasting in the Microsoft Word manuscript file. Tables should be prepared in Microsoft Word. Use Arabic numerals to designate figures and upper case letters for their parts (Figure 1). Begin each legend with a title and include sufficient description so that the figure is understandable without reading the text of the manuscript. Information given in legends should not be repeated in the text.

**References:** In the text, a reference identified by means of an author's name should be followed by the date of the reference in parentheses. When there are more than two authors, only the first author's name should be mentioned, followed by 'et al'. In the event that an author cited has had two or more works published during the same year, the reference, both in the text and in the reference list, should be identified by a lower case letter like 'a' and 'b' after the date to distinguish the works.

Examples:

Abayomi (2000), Agindotan et al. (2003), (Kelebeni, 1983), (Usman and Smith, 1992), (Chege, 1998;

1987a,b; Tijani, 1993,1995), (Kumasi et al., 2001)

References should be listed at the end of the paper in alphabetical order. Articles in preparation or articles submitted for publication, unpublished observations, personal communications, etc. should not be included in the reference list but should only be mentioned in the article text (e.g., A. Kingori, University of Nairobi, Kenya, personal communication). Journal names are abbreviated according to Chemical Abstracts. Authors are fully responsible for the accuracy of the references.

Examples:

Ogunseitun OA (1998). Protein method for investigating mercuric reductase gene expression in aquatic environments. *Appl. Environ. Microbiol.* 64:695-702.

Gueye M, Ndoye I, Dianda M, Danso SKA, Dreyfus B (1997). Active N<sub>2</sub> fixation in several *Faidherbia albida* provenances. *Ar. Soil Res. Rehabil.* 11:63-70.

Charnley AK (1992). Mechanisms of fungal pathogenesis in insects with particular reference to locusts. In: Lomer CJ, Prior C (eds) *Biological Controls of Locusts and Grasshoppers: Proceedings of an international workshop held at Cotonou, Benin.* Oxford: CAB International, pp 181-190.

Mundree SG, Farrant JM (2000). Some physiological and molecular insights into the mechanisms of desiccation tolerance in the resurrection plant *Xerophyta viscata* Baker. In Cherry et al. (eds) *Plant tolerance to abiotic stresses in Agriculture: Role of Genetic Engineering*, Kluwer Academic Publishers, Netherlands, pp 201-222.

### Short Communications

Short Communications are limited to a maximum of two figures and one table. They should present a complete study that is more limited in scope than is found in full-length papers. The items of manuscript preparation listed above apply to Short Communications with the following differences: (1) Abstracts are limited to 100 words; (2) instead of a separate Materials and Methods section, experimental procedures may be incorporated into Figure Legends and Table footnotes; (3) Results and Discussion should be combined into a single section.

**Proofs and Reprints:** Electronic proofs will be sent (e-mail attachment) to the corresponding author as a PDF file. Page proofs are considered to be the final version of the manuscript. With the exception of typographical or minor clerical errors, no changes will be made in the manuscript at the proof stage.

**Copyright: © 2013, Academic Journals.**

All rights Reserved. In accessing this journal, you agree that you will access the contents for your own personal use but not for any commercial use. Any use and or copies of this Journal in whole or in part must include the customary bibliographic citation, including author attribution, date and article title.

Submission of a manuscript implies: that the work described has not been published before (except in the form of an abstract or as part of a published lecture, or thesis) that it is not under consideration for publication elsewhere; that if and when the manuscript is accepted for publication, the authors agree to automatic transfer of the copyright to the publisher.

**Disclaimer of Warranties**

In no event shall Academic Journals be liable for any special, incidental, indirect, or consequential damages of any kind arising out of or in connection with the use of the articles or other material derived from the IJPS, whether or not advised of the possibility of damage, and on any theory of liability.

This publication is provided "as is" without warranty of any kind, either expressed or implied, including, but not limited to, the implied warranties of merchantability, fitness for a particular purpose, or non-infringement. Descriptions of, or references to, products or publications does not imply endorsement of that product or publication. While every effort is made by Academic Journals to see that no inaccurate or misleading data, opinion or statements appear in this publication, they wish to make it clear that the data and opinions appearing in the articles and advertisements herein are the responsibility of the contributor or advertiser concerned. Academic Journals makes no warranty of any kind, either express or implied, regarding the quality, accuracy, availability, or validity of the data or information in this publication or of any other publication to which it may be linked.



## ARTICLES

### Review

- Effect of stabilizers on stiffness modulus of soil layers: A review** 1602  
Dariush Moazami, Zainuddin Md. Yusoff, Ratnasamy Muniandy  
and Hussain Hamid

### CHEMISTRY

- Synthesis and characterization of polyindole with liquid  
crystalline azobenzene as side chains** 1611  
Seyed Hossein Hosseini and Maryam Ashjari

### MATHEMATICS

- Almost quaternionic integral submanifolds and totally umbilic  
integral submanifolds** 1623  
Fatma Özdemir

### COMMUNICATION TECHNOLOGY

- Multiband fractal based reconfigurable antenna with introduction  
of RF MEMS switches for next generation devices** 1628  
Paras Chawla and Rajesh Khanna

### MATERIAL SCIENCE

- Synthesis and characterization of nano-hydroxyapatite (n-HAP)  
using the wet chemical technique** 1639  
Aruneshan Chandrasekar, Suresh Sagadevan and Arivuoli  
Dakshnamoorthy



## Review

# Effect of stabilizers on stiffness modulus of soil layers: A review

Dariush Moazami\*, Zainuddin Md. Yusoff, Ratnasamy Muniandy and Hussain Hamid

Department of Civil Engineering, University Putra Malaysia, 43400 UPM Serdang, Selangor, Darul Ehsan, Malaysia.

Accepted 15 August, 2013

**Subgrade layer has a significant contribution in the pavement structure, and the quality of this layer has a great impact on the subsequent pavement design. Pavement design guide as specified in the AASHTO (2002), incorporates engineering properties of unbound and stabilized subgrade soils, since in many cases fatigue or rutting failure in pavements are due to insufficient stiffness modulus in soil layers. Subgrade materials are characterized by common engineering properties including stiffness and strength. Appropriate treatment using different additives is considered an effective way to achieve a more durable pavement structure and also to increase the stiffness modulus. In this paper, the importance of using proper stiffness for underlying layers and the effects of common additives such as lime, cement and fly ash on improving the strength and stiffness modulus of soil layers are highlighted.**

**Key words:** Stiffness modulus, cementitious stabilization, soil properties.

## INTRODUCTION

Subgrade in pavement design and construction is a very important layer since it must provide a stable platform for the subsequent top layers. In addition, pavement design is greatly influenced by the quality of this layer. Subgrade materials should be characterized by their engineering properties such as strength and stiffness (stress-strain relationship under traffic loading) in order to control pavements damage. Providing sufficient stiffness for subgrade cannot be easily obtained all the time; hence, reinforcing the subgrade layer is inevitable and it is necessary to improve the existing stiffness modulus by using various stabilizers. Therefore, improving the engineering properties of subgrade soils using cementitious stabilizations is widely used.

Resilient modulus ( $M_r$ ) and Unconfined Compressive Strength (UCS) are the essential values of stabilized soils in the new Mechanistic Empirical Pavement Design Guide (MEPDG, 2004) when designing a new pavement. However, only limited studies have specified these

parameters (Solanki et al., 2009). This paper presents a comprehensive review on the importance of using adequate stiffness for underlying layers and utilizing common additives with their percentages. Furthermore, the associated improvement in the engineering properties of the subgrade is reviewed.

### Importance of appropriate subgrade stiffness

Studies conducted on pavement structural design indicates that pavement layer thickness is governed by the stiffness of subgrade and granular layers. Thus information on the stiffness modulus of subgrade and granular layers are required before performing any pavement design. In a pavement structure; base, subbase and subgrade layers with high stiffness values possess higher stress distribution ability than those with low stiffness. Thus the required thickness of the

\*Corresponding author. E-mail: [dariush.moazami@yahoo.com](mailto:dariush.moazami@yahoo.com). Tel: (+60)123507016 or (+98)9153015206.

pavement can be reduced when stiffer layer components are used in the pavement structure. Accordingly, considerable reduction in the construction cost can be achieved beside the optimum design.

On the other hand, pavement layers with low stiffness values exhibit weak performance and in order to improve their properties, it may be required to either increase the asphalt final thickness or to improve the stiffness of the soil layers using appropriate additives. Increased stiffness causes the traffic load to spread over a greater area.

Furthermore, numerous studies have indicated that many cases of fatigue or rutting failures in pavements are due to inadequate stiffness of soil layers (Van Zyl and Maree, 1983; Wright and Paquette, 1987; Barksdale and Itani, 1989; Zakaria and Leest, 1996; Jegede, 2000; Giroud and Han, 2004; Mulungye et al., 2007; Xu and Huang, 2011; Cardone et al., 2011).

Barksdale and Itani, (1989) indicated that uncrushed gravels have a lower stiffness modulus than crushed stones making them more susceptible to rutting. In addition, Zakaria and Leest (1996) stated that aggregate type, fines percentage, moisture content, compaction and load applications are influential factors in the induced strains in a pavement structure. Giroud and Han (2004) stated that bearing capacity failure, after repeated traffic loading, in the base or subgrade layer is the main cause of surface rutting.

Xu and Huang (2011) concluded that most of rutting in pavement layers is related to the weakness in the middle and lower layers. Based on studies done by Wright and Paquette, (1987), roughly 25% of the rutting is related to subbase, 50% to the base and 25% to the asphalt concrete surface. Since in the MEPDG, the total rut depth is equal to sum of the rut depths in each layer, the rutting of underlying layers should not be overlooked. In terms of fatigue failure, Mulungye et al. (2007) stated that even in weak soil layers, fatigue cracking normally occurs before rutting. According to the studies done by Cardone et al. (2011), the stiffness of soil and granular layer must be sufficiently high to avoid fatigue cracking.

In order to overcome the problem of rutting in pavement layers, Jegede (2000) stated that stabilization could improve the California Bearing Ratio (CBR) when facing poor soil properties. His suggestion agrees with Van Zyl and Maree (1983) who noted that when the density of soil is increased (increased stiffness), the plastic deformation of soils is reduced significantly. The suggestion of Van Zyl and Maree (1983) clearly indicates that using appropriate stiffness for underlying pavement layers is very important. In addition, since providing sufficient stiffness for subgrade cannot be easily obtained all the time at the site, it is imperative that reinforcing and/or improving the stiffness modulus of subgrade or any of pavement layers using different stabilizers is inevitable.

## STIFFNESS MODULUS OF VARIOUS SOILS

The stiffness of unbound pavement materials is characterized by the resilient modulus ( $M_r$ ). AASHTO (1986) design guide has recommended the resilient modulus for characterizing subgrade stiffness in both flexible and rigid pavements.

In resilient modulus test, repeated axial cyclic stress of a fixed magnitude, loading time and frequency is applied to the top of the cylindrical soil specimen. From the surroundings, it is under a static confining pressure provided by the triaxial pressure chamber. In fact, this test is the triaxial compression test under cyclic stress. Resilient modulus can be estimated from soil classification and soil unit weight as well. For instance, Table 1 summarizes the resilient modulus of different soils based on their classification.

### Effect of additives on increasing stiffness modulus

Cement stabilization has been widely used to enhance the performance of subgrade layer in pavement structures (Houry et al., 2006). Stabilization process consists of mixing stabilizing agents such as lime, fly ash, and cement with raw soil in which cementing compounds are the key elements for strength and stiffness improvement. The degree of effectiveness varies from one stabilizing agent to the other.

Although several studies have been conducted in the past to evaluate the performance of stabilized soils and aggregates in pavement construction (McManis and Arman, 1989; Zaman et al., 1992; Puppala et al., 1996; Misra, 1998; Little, 2000; Miller and Zaman, 2000; Senol et al., 2002; Houry and Zaman, 2007), only a few studies (Edil et al., 2006; Chauhan et al., 2008; Mohammad and Saaheh, 2008; Li et al., 2009; Solanki et al., 2009; Singh et al., 2010; Solanki and Zaman, 2011; Tastan et al., 2011; Rout et al., 2012), have determined the required inputs for stabilized soils in the new MEPDG (2004). These inputs include the resilient modulus ( $M_r$ ) and unconfined compressive strength (UCS), when designing a new pavement. Common additives and the associated results of the soil stabilization process are summarized as follows:

### Lime

Since lime chemically changes the plasticity properties of the soil, it is frequently used to treat clays. Although lime stabilization is effective to some extent, the strength and stiffness enhancement is moderate.

In a study by Solanki et al. (2009), specimens were prepared by adding 3, 6, and 9% of lime (by dry weight of soil) to the raw soils that were classified as CL-ML with a

**Table 1.** Default  $M_R$  values for unbound granular and subgrade materials at optimum moisture content and density conditions (NCHRP 1-37A, 2004).

AASHTO soil class	Resilient modulus range (psi)	Typical resilient modulus (psi)
A-1-a	38,500 - 42,000	40,000
A-1-b	35,500 - 40,000	38,000
A-2-4	28,000 - 37,500	32,000
A-2-5	24,000 - 33,000	28,000
A-2-6	21,500 - 31,000	26,000
A-2-7	21,500 - 28,000	24,000
A-3	24,500 - 35,500	29,000
A-4	21,500 - 29,000	24,000
A-5	17,000 - 25,500	20,000
A-6	13,500 - 24,000	17,000
A-7-5	8,000 - 17,500	12,000
A-7-6	5,000 - 13,500	8,000

liquid limit (LL) of 27 and a plasticity index (PI) of 5 and CL with LL = 37 and PI = 11. The additive and soil were blended manually to become uniform. After the mixing process, desired amount of water was added to obtain the optimum moisture content (OMC). The mixture was then compacted in a mold with a diameter of 101.6 mm (4.0 in) and a height of 203.2 mm (8.0 in) to obtain approximately 95 to 100% of the maximum dry density (MDD). After compaction, extruded specimens were cured in a moisture-controlled room with  $23.0 \pm 1.7^\circ\text{C}$  temperature and a relative humidity of approximately 96% for a period of 28 days. AASHTO T 307-99 was used for  $M_r$  tests, and the UCS tests were performed in accordance with the ASTM D1633 test method. Their study concluded that there is an increase in  $M_r$  value with increase in the percentage of lime content since more cementing compounds were constituted. For the raw soil, the  $M_r$  value was found to be 153 MPa, while for samples with 3, 6 and 9% of lime, the  $M_r$  values were 5.6, 7.1, 7.3 times more than the control sample, respectively. The UCS was 227 kPa for the raw soil. Addition of 3, 6, and 9% of lime increased the UCS values by a factor of 1.7, 1.7 and 2, compared to the control sample, respectively.

Rout et al. (2012) investigated the resilient modulus (according to AASHTO T-307) behavior of three subgrade soils. Based on unified classification, the tested soils were CH with various plastic properties. The soils were stabilized using lime-cement to evaluate the efficiency in enhancing the resilient characteristics. Furthermore, effects of confining and deviator stresses were investigated. In their study, laboratory specimens were compacted in such a way that the sample's height is two times greater than its diameter (for instance 142 mm in height and 71 mm in diameter). The soil was air dried and mixed with 6% of lime and 3% of cement. The soil specimens were prepared at the moisture content of 3%

more than the OMC. After initial blending of soil with lime and cement, the mixture was maintained in the room temperature for at least 72 h before compaction. Both control and treated samples were cured in a humidity room for duration of two and seven days, respectively. Resilient Modulus values for untreated soils ranged between 30 to 50 MPa, whereas for the same treated soil, it was up to three times more especially for the soil with highest plastic property. It was observed that in untreated subgrade soil, increasing the deviator stress resulted in resilient modulus reduction for all the three tested confining pressures (13.8, 27.6, 41.4 KPa). This phenomenon is due to the strain softening behavior in clayey soils. On the other hand, in treated soils, increasing the deviator stress resulted in an increase in resilient modulus; this could be because of strain hardening behavior of granular materials. This is due to the fact that the treated soils exhibit non-plastic behavior and their modulus depends on confining stresses as expected by granular materials.

Mohammad and Saadeh (2008) investigated stabilization of A-4 clay soil with 10% of lime. Cylindrical soil specimens ( $D = 71.1$  mm and  $H = 142.2$  mm) were compacted with an impact compactor in five layers on which the repeated load triaxial resilient modulus (AASHTO T 307, 2003) and material property tests were conducted. The untreated specimens were immediately tested after the compaction, while the compacted lime-treated samples were covered with polythene bags and kept in the humidity room for a duration of 7, 14, and 28 days for curing. The lowest resilient modulus in untreated subgrade soil was 35 MPa, while for the lime-treated soils it was 2.25 to 3.25 times more based on different cyclic stresses ranges from 12 to 62 KPa with 41 KPa of confining pressure.

Singh et al. (2010) evaluated the effectiveness of lime in a sulfate containing soil, that was characterized as CL

**Table 2.** Effect of lime stabilizer on improving  $M_r$  and UCS in soils.

Authors' name	Soil type	Additive type	Stabilizer percentage (%)	Moisture (%)	Curing time (days)	Measuring parameter	Initial Value (Mpa)	Rate of increase
Solanki et al. (2009)	CL-ML, CL	Lime	3	OMC	28	$M_r$	153	5.6
			3			UCS	227	1.7
			6			$M_r$	153	7.1
			6			UCS	227	1.7
			9			$M_r$	153	7.3
			9			UCS	227	2.0
Rout et al. (20120)	CH	Lime-cement	6-3	OMC+3	7	$M_r$	30-50	3.0
Mohammad and Saadeh (2008)	A-4	Lime	10	-	28	$M_r$	35	2.25-3.25
Singh et al. 2010	CL	Lime	5	OMC	28	$M_r$	58	4.9
Solanki and Zaman 2011	CL-ML	Lime	6	OMC	28	$M_{rt}$	65	12
	CL	Lime	6	OMC	28	$M_{rt}$	29	22

type (Unified-based classification) or A – 7 - 6 (AASHTO-based classification). In their study, the optimum lime content was selected based on the strength and pH tests. Harvard miniature compacted specimens with 3, 6, and 9% of lime were cured for 28 days in a moisture-controlled room at  $23.0 \pm 1.7^\circ\text{C}$  temperature and 96% humidity. Samples were then subjected to UCS test with 0.6 mm/min increment based on the ASTM D 1632-96. The UCS results showed an increase for up to 4% of lime, after which only a minor change was observed in UCS value. Among various tested percentages of lime (0, 1, 3, 5, 7, 9 and 100%); the pH value increased significantly until 5% in the pH test (ASTM D 6276-99). Finally, 5% of lime was chosen as the optimum content. The resilient modulus test (AASHTO T 307-99) was performed on the compacted samples with a diameter of 101.6 mm and a height of 203.2 mm at OMC. The  $M_r$  result

for the lime stabilized soil improved up to 284 MPa compared to the raw soil with a modulus of 58 MPa when tested at a deviator stress of 42 kPa and confining pressure of 13 kPa; meaning that adding lime had increased the  $M_r$  value by a factor of 4.9 compared to the control samples. In their study, the  $M_r$  values were based on unsaturated condition, and suction or degree of saturation were not incorporated.

Solanki et al. (2011) evaluated the indirect tensile characteristics of lime stabilized mixtures. According to the USCS, two types of soils including CL - ML (silty clay with sand; LL = 27 and PI = 5) and CL (lean clay; LL = 37 and PI = 11) were selected with 6% of lime. For the resilient modulus in tension mode ( $M_{rt}$ ), 101.6 mm (4 in) cylindrical specimens were compacted by the use of Superpave gyratory to a height of 63.5 mm (2.5 in). Specimens were cured in a controlled environment ( $23.0 \pm 1.7^\circ\text{C}$  temperature and 96%

humidity) for 28 days after compaction, as recommended by the ASTM D 1632 test method.  $M_{rt}$  values were improved for the lime stabilized specimens. In addition, the  $M_{rt}$  decreased as the stress ratio (Deviator stress/ Maximum Tensile Stress) increased. For instance at a stress ratio of 0.36, 6% of lime resulted in approximately 12 and 22 times increase for (CL - ML) and CL, respectively relative to the initial values of 65 MPa for CL - ML and 29 MPa for CL. Effects of lime stabilizer on improving the engineering properties of raw soil are summarized in Table 2.

### Cement

In Solanki et al. (2009), while using the same procedure of stabilization for lime, they added 5, 10, and 15% of Cement kiln Dust (CKD) to CL - ML raw soil. CKD is an industrial waste gathered

**Table 3.** Effect of cement stabilizer on improving  $M_r$  and UCS in soils.

Authors' name	Soil type	Additive type	Stabilizer percentage (%)	Moisture (%)	Curing time (days)	Measuring parameter	Initial value (Mpa)	Rate of increase
Solanki et al. (2009)	CL-ML	CKD	3	OMC	28	$M_r$	153	4.8
			3			UCS	227	1.3
			6			$M_r$	153	15.7
			6			UCS	227	4.8
			9			$M_r$	153	16.7
			9			UCS	227	6.0
Mohammad and Saadeh (2008)	A-4	Cement	8	-	28	$M_r$	35	10-15

during the production process of Portland cement. Based on their results, the  $M_r$  value was 153 MPa for the raw soil, while for the specimens stabilized with 5, 10 and 15% of CKD, the  $M_r$  values increased as much as 4.8, 15.7, 16.7 times, respectively. In addition, the UCS value was found to be 227 kPa for the raw soil and increased by a factor of 1.3, 4.8, and 6 for 5, 10, and 15% of CKD, respectively.

Mohammad and Saadeh (2008), using the same procedure of stabilization for lime, added 8% of cement for stabilization of A - 4 clay soil. They concluded that the resilient modulus of cement-treated subgrade soil increased 10 to 15 times (based on different cyclic stresses) relative to the control samples with resilient modulus of 35 MPa. Effects of cement stabilizer on improving the engineering properties of raw soil are summarized in Table 3.

### **Fly ash**

Fly ash is a non-crystalline pozzolanic and slightly cementitious material. It is an environmentally hazardous solid waste, produced mostly from the

burning of coal in thermal power plants. Solanki et al. (2009), using the same procedure of stabilization for lime and cement, prepared specimens by adding 5, 10, and 15% of a class C Fly Ash (CFA) to the CL - ML soil. They concluded that, the  $M_r$  values was 153 MPa before stabilization and increased by a factor of 1.7, 4.2 and 14.1 when 5, 10, and 15% of CFA stabilizing agent was used. One of the reasons for the higher  $M_r$  values is related to the high percentage of pozzolans in CFA, which is responsible for the constitution of cementitious products. The UCS value was 227 kPa for the control sample. Addition of 5, 10 and 15% of CFA increased the UCS by a factor 1.3, 2.4 and 4, respectively as they noted.

Li et al. (2009) evaluated the ability of Fly Ash to increase the unconfined compressive strength and stiffness of the subgrade soils both in the laboratory and in the field. Twelve percent of class C Fly Ash, by dry weight, was mixed with the subgrade soil, which consisted of lean clay (CL), clayey sand (SC), and silty sand (SM) (using Unified Soil Classification) or A-7-6 with a group index (GI) > 10, A - 6 with GI > 2 and A - 2 - 6 with GI < 1 (using AASHTO Soil Classification).

The  $M_r$  tests (AASHTO T292, 1991) were performed immediately after compaction with optimum water content, or after 14 days of curing while sealed in plastic wrap and kept in a room with 100% humidity. Since, there is no UCS standard method for Fly Ash stabilized materials, in their study a strain rate of 0.21% per min was used for the UCS tests based on the ASTM D 5102 for compacted soil - lime mixtures. In the field, strength and stiffness of the stabilized soils were evaluated by means of Soil Stiffness Gauge (SSG), Dynamic Cone Penetrometer (DCP), after 7 days of curing, and Falling Weight Deflectometer (FWD). Results indicated that initial  $M_r$  of the subgrade varied between 34 and 42 MPa (with a mean = 38 MPa) while, the  $M_r$  for laboratory - mix Fly Ash stabilized soils ranged from 115 to 167 MPa (with a mean = 139 MPa). On the other hand, the field-mixed Fly Ash stabilized soil had  $M_r$  of 60 to 129 MPa (with a mean = 82 MPa). Their results indicated that the addition of 12% of Fly Ash to the raw soil increased the  $M_r$  value by a factor of 3.7 in the laboratory and 2.2 in the field, respectively. Their results also showed that by adding Fly Ash to the subgrade UCS increased significantly. The UCS

of the subgrade ranged from 92 to 138 kPa (with a mean = 112 kPa), the laboratory stabilized samples had UCS between 360 and 1120 kPa (with a mean = 663 kPa), and the UCS of field stabilized soils ranged from 110 to 410 kPa (with a mean = 183 kPa). Thus it is clearly shown that addition of 12% of type C Fly Ash to the subgrade soil improved the  $M_r$  value by a factor of 5.9 in the laboratory and 1.6 in the field, respectively. Furthermore, they reported that mixing condition and type of mixing had caused these differences.

In a study by Edil et al. (2006), seven soft fine-grained soils (six inorganic soils and one organic soil) were mixed with four types of Fly Ashes and subjected to California Bearing Ratio (CBR) and resilient modulus ( $M_r$ ) tests. The soils were CL, CH, OH (Unified Soil Classification) or A-7-5, A-7-6, A-6 (AASHTO Soil Classification) with the plasticity indices ranging between 15 and 38. Two of the Fly Ashes were selected from high quality class, while the others did not fulfill the requirements of class C or class F based on the ASTM C 618 specification. Tests were conducted on soils and soil–Fly Ash mixtures prepared with optimum water content, 7% more than optimum content as well as a very wet *in situ* condition (9–18% more than optimum water content). Unsoaked CBR tests were performed both on the raw soils and soil–Fly Ash mixtures according to ASTM D 1883 specification. For the resilient modulus, AASHTO T 292-91 procedure was followed. For compaction procedure, standard proctor was selected after 1 to 2 h delay from mixing. Compacted soil–Fly Ash specimens were cured at 25°C and 100% relative humidity. The CBR tests were conducted after 7 days of curing. However, for resilient modulus test, specimens were cured for 14 and 56 days. Adding 10 and 18% of Fly Ash increased CBR by a factor of 4 and 8, respectively. At 7% wet of optimum,  $M_r$  of the raw soil ranged between 3 and 15 MPa. Mixtures with 10 and 18% of Fly Ash had  $M_r$  of 12 to 60 MPa and 51 to 106 MPa, respectively. They reported that Fly Ashes with higher CaO/SiO<sub>2</sub> ratio constituted mixtures with higher CBR and  $M_r$ . Furthermore, finer grained or more plastic soils have smaller CBR or  $M_r$  values before stabilization, while greater CBR ratio and  $M_r$  ratio were obtained after stabilization. The resilient modulus did not increase significantly after 7 and 14 days of curing, while the increase was noticeable between 14 and 28 days. After 28 days, little further increase occurred in the resilient modulus. Among the four tested Fly Ashes, type C exhibited the maximum improvement. The effect of Fly Ash on the CBR and  $M_r$  was much lower for the organic soil compared to inorganic soils.

Solanki and Zaman (2011), using the same procedure of stabilization for lime, evaluated the indirect tensile properties of soil specimens (CL - ML and CL) stabilized with class C of Fly Ash. Results indicated improvement in  $M_{rt}$  values for CFA stabilized specimens. Moreover, increasing the stress ratio (Deviator stress/Maximum

Tensile Stress) resulted in  $M_{rt}$  decline. For instance, at a stress ratio of 0.36, adding 10% of CFA provided approximately 7.5 and 24.9 times of increase for (CL - ML) and CL, respectively.

Singh et al. (2010), using the same procedure of stabilization for lime, evaluated the effectiveness of CFA (12, 15 and 18%) for CL or A-7-6 type soil. The UCS increased up to 16% of CFA, after which minor change was observed in the UCS strength. Among various percentages of additive (0, 6, 8, 10, 12, 14, 16, 18 and 100%), the pH value had significant increase until 4%. Finally, the use of 16% CFA was recommended for subsequent testing. The  $M_r$  results for the CFA stabilized soil indicated 4.5 times increase compared to those of the raw soils which had ranged from 26 to 58 MPa.

Tastan et al. (2011) evaluated the efficiency of different percentages of Fly Ash (up to 30% content) in stabilizing organic soils. Three soft organic soils with different organic contents including silty, sandy peat (Pt, A-8(0)), low plasticity organic sandy clay (OL-OH, A-7-5(32)), and moderately plastic organic clay (OL, A-4(5)), were used in this study. Unconfined compression tests were conducted following ASTM D5102 (ASTM 2009b) with the strain rate of 0.21% per min. The compaction effort was adjusted in such a way that the same impact energy per unit volume as in the standard Proctor effort [ASTM D698 (ASTM 2007)], was experienced. Compacted samples were cured for seven days to simulate the early curing conditions during construction at 100% relative humidity and 25°C. Specimens for the resilient modulus and unconfined compression tests were prepared in a mold with a diameter of 102 mm and a height of 203 mm. Compaction effort was as the same compaction energy per unit volume in the standard Proctor compaction method (600 kN/m<sup>3</sup>). They concluded that, for clayey soils with an Organic Content (OC) of less than 10%, UCS value increases noticeably (from 30 kPa without Fly Ash to more than 400 kPa with Fly Ash). On the other hand, for a highly organic sandy silty peat with OC = 27%, lower increases in UCS value were observed (from 15 kPa without Fly Ash to more than 100 kPa with Fly Ash). For instabilized organic soils, resilient modulus test could not be performed at wet conditions since the specimens were too soft. Addition of Fly Ash (up to 30%) to OL - OH and OL (OC = 5 and 6%, respectively) resulted in  $M_r$  values between 10 to 100 MPa (this depends on the type and percentage of the Fly Ash used). Furthermore,  $M_r$  improved up to 120 MPa at Optimum Water Content (OWC). However, for Pt (OC = 27%), the stabilized mixture never produced  $M_r$  greater than 30 MPa no matter which Fly Ash type and percentage was used. Finally, they conclude that increase in the organic content decreases the strength of the mixture exponentially. They also reported that the maximum UCS and  $M_r$  were obtained when the CaO content was greater than 10% and the CaO/SiO<sub>2</sub> ratio

**Table 4.** Effect of Fly Ash stabilizer on improving  $M_r$  and UCS in soils.

Authors' name	Soil type	Additive type	Stabilizer percentage (%)	Moisture (%)	Curing time (days)	Measuring parameter	Initial value	Rate of increase	
Solanki et al. (2009)	CL-ML	Fly ash	3	OMC	28	$M_r$	153 Mpa	1.7	
			3			UCS	227 KPa	1.3	
			6			$M_r$	153 Mpa	4.2	
			6			UCS	227 KPa	2.4	
			9			$M_r$	153 Mpa	14.1	
			9			UCS	227 KPa	4.0	
Li et al. (2009)	CL, SC, SM	Fly ash	12	OMC	14	$M_r$	38 Mpa	3.7	
						UCS	112 KPa	5.9	
			-	7	$M_r$	38 Mpa	2.2		
					UCS	112 KPa	1.6		
Edil et al. (2006)	CL-CH	Fly ash	10	$\geq$ OMC	14	$M_r$	9 MPa	4	
			18					8.7	
			10			7	CBR	-	4
			18						8
Solanki and Zaman (2011)	CL-ML CL	Fly ash	10	OMC	28	$M_{rt}$	65 MPa	7.5	
			10			$M_{rt}$	29 MPa	24.9	
Singh et al. (2010)	CL	Fly ash	16	OMC	28	$M_r$	26-58 MPa	4.5	
Tastan et al. (2011)	OL, OL- OH, PEAT (OC<10) OC>27	Fly ash				$M_r$	10 Mpa	12	
						UCS	30	13.4	
		Fly ash	Up to 30%	OWC	7	$M_r$	<1	<30	
						UCS	15	6.7	

ranges from 0.5 to 0.8.

Chauhan et al. (2008) mixed 30% of Fly Ash and 70% of silty sand which yielded the maximum

UCS value. They stated that as the number of load cycles and deviator stress increases, the resilient modulus decreases. However, increasing

confining pressure resulted in resilient modulus increase. Table 4 summarizes different studies on the Fly Ash stabilizer.



## CONCLUSION

A stable subgrade layer is a key component of a pavement structure. Engineering properties such as strength and resilient modulus of subgrade are influential parameters on the overall performance of the pavement structure, since in many cases fatigue or rutting failure in pavements are because of insufficient stiffness modulus in soil layers. The new Mechanistic-Empirical Pavement Design Guide (AASHTO, 2004) incorporates engineering properties of subgrade soils (unbound or stabilized) in the design procedure because of its importance.

Providing sufficient stiffness for subgrade cannot be easily obtained all the time; hence, reinforcing the subgrade layer is inevitable and it is necessary to improve the existing stiffness modulus by using various stabilizers. The following conclusions were derived:

1. In treated soils, increasing the deviator stress resulted in an increase in resilient modulus since treated soils exhibit non-plastic behavior and their modulus depends on confining stresses as expected by granular materials.
2.  $M_{rt}$  values were improved for the lime and Fly Ash stabilized specimens. In addition, the  $M_{rt}$  decreased as the stress ratio (Deviator stress/Maximum Tensile Stress) increased.
3.  $M_r$  value increases with increase in the percentage of lime content. This is especially true for the soil with higher plastic property.
4. CFA increases the resilient modulus and CBR, the reasons for the higher  $M_r$  values is related to the high percentage of pozzolans in CFA. Therefore, Fly Ashes with higher CaO/SiO<sub>2</sub> constituted mixtures with higher CBR and  $M_r$ .

Furthermore, the amount of resilient modulus increase differs for laboratory and *in situ* conditions because of differences in mixing conditions and type of mixing. Moreover, finer grained or more plastic soils have smaller CBR or  $M_r$  values before stabilization, while greater CBR ratio and  $M_r$  ratio were obtained after stabilization as follows:

1. For CFA stabilized soils, curing time is influential in improving the resilient modulus. The resilient modulus did not increase significantly after 7 and 14 days of curing, while the increase was noticeable between 14 and 28 days. After 28 days, little further increase occurred in the resilient modulus. Among Class C, Class F, and non classic Fly Ashes, type C exhibited the maximum improvement.
2. Fly Ash improves the resilient modulus and UCS, while the amount of this improvement reduces with increase in the organic content. The maximum UCS and  $M_r$  were obtained when the CaO content was greater than 10% and the CaO/SiO<sub>2</sub> ratio ranges between 0.5 and 0.8.
3. For treated soils, as the number of load cycles and

deviator stress increases, the resilient modulus decreases. However, increasing confining pressure resulted in resilient modulus increase.

## REFERENCES

- AASHTO T 292 (1991). Resilient Modulus of Subgrade Soils and Untreated Base/Subbase Materials.
- AASHTO (2002). Standard Method of Test for Resilient Modulus of Subgrade Soils and Untreated Base/Subbase Materials, AASHTO Designation 307, Standard Specifications for Transportation Materials and Methods of Sampling and Testing, Part II Tests. American Association of State Highway and Transportation Officials, Washington, DC.
- ASTM C618 (2012). Standard Specification for Coal Fly Ash and Raw or Calcined Natural Pozzolan for Use in Concrete.
- ASTM D698 (2007). Standard test methods for laboratory compaction characteristics of soil using standard effort.
- ASTM D1632 (1996). Standard Practice for Making and Curing Soil-Cement Compression and Flexure Test Specimens in the Laboratory.
- ASTM D1633 (2007). Standard Test Methods for Compressive Strength of Molded Soil-Cement Cylinders.
- ASTM D1883 (2007). Standard Test Method for CBR (California Bearing Ratio) of Laboratory-Compacted Soils.
- ASTM D5102 (1996). Standard Test Method for Unconfined Compressive Strength of Compacted Soil-Lime Mixtures.
- ASTM D5102 (2009). Standard test method for unconfined compressive strength of compacted soil-lime mixtures.
- ASTM D6276 (1999). Standard Test Method for Using pH to Estimate the Soil-Lime Proportion Requirement for Soil Stabilization.
- Barksdale RD, Itani SY (1989). Influence of Aggregate Shape on Base Behavior; In Transportation Research Record 1227, Transportation Research Board, National Research Council, Washington, D. C., pp 173-182.
- Chauhan MS, Mittal S, Bijayananda Mohanty B (2008). Performance evaluation of silty sand subgrade reinforced with Fly Ash and fibre. Geotextiles and Geo-membranes 26, ASCE. pp. 429-435.
- Cardone F, Cerni G, Virgili A, Camilli S (2011). Characterization of permanent deformation behaviour of unbound granular materials under repeated triaxial loading. J. Constr. Build. Mater. Elsevier 28:79-87.
- Edil TB, Acosta HA, Benson CH (2006). Stabilizing Soft Fine-Grained Soils with Fly Ash. J. Mater. Civ. Eng. ASCE pp. 283-294.
- Giroud JP, Han J (2004). Design method for geogrid-reinforced unpaved roads. I. Development of design method, II. Calibration and Applications Journal of Geotechnical and Geo-environmental Engineering, American Society of Civil Engineers, ASCE 130:787-797.
- Jegade G (2000). Effect of soil properties on pavement failures along the F209 highway at Ado-Ekiti, south-western Nigeria. J. Constr. Build. Mater. 14, Elsevier pp. 311-315.
- Khoury N, Zaman M, Laguros J (2006). Semi-quantification of cementing products using X-ray diffraction technique in stabilized aggregate. J. X-Ray Sci. Technol. 14(1):39-54.
- Khoury N, Zaman M (2007). Environmental effects on durability of aggregates stabilized with cementitious materials. J. Mater. Civ. Eng. 19(1):41-48.
- Lin LM, Tastan O, Benson CH, Edil TB (2009). Field Evaluation of Fly Ash Stabilized Subgrade in US 12 Highway. International Foundation Congress and Equipment Expo. ASCE. pp. 385-392.
- Little DL (2000). Evaluation of structural properties of lime stabilized soils and aggregates. Report Prepared for National Lime Association.
- McManis KL, Arman A (1989). Class C fly ash as a full or partial replacement for portland cement or lime. Transportation Research Record. 1219, Transportation Research Board, National Research Council, Washington, D. C.
- Miller GA, Zaman M (2000). Field and laboratory evaluation of cement kiln dust as a soil stabilizer. Transportation Research Record. 1714,

- Transportation Research Board, National Research Council, Washington, D.C.
- Misra A (1998). Stabilization characteristics of clays using class C fly ash. Transportation Research Record. 1611, Transportation Research Board, National Research Council, Washington, D.C.
- Mohammad L, Saadeh S (2008). Performance Evaluation of Stabilized Base and Subbase Material. Geo Congress, ASCE. pp 1073-1080.
- Mulungye RM, Owende PMO, Mellon K (2007). Finite element modeling of flexible pavements on soft soil subgrades, Elsevier J. Mater. Design 28:739-756.
- NCHRP (2004). Guide for Mechanistic-Empirical Design of New and Rehabilitated Pavement Structures. Final Report, Project 1-37A, TRB, National Cooperative Highway Research Program, Washington, D.C..
- Puppala AJ, Mohammad LN, Allen A (1996). Engineering behavior of lime-treated Louisiana subgrade soil. Transportation Research Record. 1546, Transportation Research Board, National Research Council, Washington, D.C.
- Rout RK, Ruttanapornmakul P, Valluru S, Puppala AJ (2012). Resilient Moduli Behavior of Lime-Cement Treated Subgrade Soils. Geo Congress, ASCE. pp. 1428-1437.
- Senol A, Bin-Shafique Md S, Edil TB, Benson CH (2002). Use of class C fly ash for stabilization of soft subgrade. Proceeding of 5<sup>th</sup> International Congress on Advances in Civil Engineering, Istanbul Technical University, Turkey.
- Singh D, Ghabchi R, Laguros JG, Zaman M (2010). Laboratory Performance Evaluation of Stabilized Sulfate Containing Soil with Lime and Class C Fly Ash. GeoFlorida, Advances in Analysis, Modeling & Design, ASCE. pp. 757-766.
- Solanki P, Khoury N, Zaman MM (2009). Engineering Properties and Moisture Susceptibility of Silty Clay Stabilized with Lime, Class C Fly Ash, and Cement Kiln Dust. J. Mater. Civ. Eng. ASCE. pp. 749-757.
- Solanki P, Zaman M (2011). Characterization of Lime and Fly Ash-Stabilized Soil By Indirect Tensile Testing. ASCE. Pp. 4438-4448.
- Tastan EO, Edil TB, Benson CH, Aydilek AH (2011). Stabilization of Organic Soils with Fly Ash. Journal of Geotechnical and Geoenvironmental Engineering, ASCE. pp. 819-833.
- Van Zyl NJW, Maree JH (1983). The behaviour of high standard crushed stone base pavement during heavy vehicle simulator test. Civ. Eng. S. Africa 25(7):745-753.
- Wright PH, Paquette RJ (1987). Highway Engineering, 5th edition, John Wiley, New York.
- Xu T, Huang X (2011). Investigation into causes of in-place rutting in asphalt pavement. J. Constr. Building Mater. Elsevier 28:525-530.
- Zakaria M, Leest G (1996). Rutting characteristics of unbound aggregate layers, Constr. Build. Mater. Elsevier 10(3):185-189.
- Zaman M, Laguros JG, Sayah AI (1992). Soil stabilization using cement kiln dust. Processing of 7<sup>th</sup> International Conference on Expansive Soils, Vol. I. Texas Technology University, Lubbock, Texas. pp. 347-351.

Full Length Research Paper

# Synthesis and characterization of polyindole with liquid crystalline azobenzene as side chains

Seyed Hossein Hosseini<sup>1\*</sup> and Maryam Ashjari<sup>2</sup>

<sup>1</sup>Department of Chemistry, Faculty of Science, Islamic Azad University, Islamshahr Branch, Tehran-Iran.

<sup>2</sup>Department of Chemistry, Faculty of Science and Engineering, Islamic Azad University, Saveh Branch, Saveh-Iran.

Accepted 8 August, 2013

In this study, a series of azobenzene-functionalized liquid crystalline (LC) polyindole derivatives: poly{2-[N-ethyl-N-[4-[4'-(nitrophenyl)azo]phenyl]amino]ethyl-3-indolyl acetate}, poly(In3AA-RedI), poly{2-[N-ethyl-N-[4-[4'-(nitrophenyl)azo]phenyl]amino]ethyl-3-indolyl acetate-co-indole}, poly(In3AA-RedI-co-In), poly{2-[N-ethyl-N-[4-[4'-(nitrophenyl)azo]phenyl] amino]ethyl-3-indolyl acetate-co-pyrrole}, and Poly(In3AA-RedI-co-py) were synthesized. Novel 3-substituted indole with liquid crystalline side chain (In3AA-RedI) was synthesized by the direct reaction of indole-3-acetic acid with 2-[N-ethyl-N-[4-[4'-(nitrophenyl)azo]phenyl] amino]ethanol (RedI). Chemical polymerization of (In3AA-RedI), and its copolymerization with indole and pyrrole were carried out by using ferric perchlorate as oxidizing agent. The composition, structure and thermal property of these LC polyindole derivatives were fully characterized by FTIR, <sup>1</sup>H, <sup>13</sup>C-NMR and UV-Visible spectroscopic methods, and its LC behavior and photoresponsive property were also investigated by polarized optical microscope and differential scanning calorimetry (DSC). The results show that poly(In3AA-RedI) exhibited the smectic A (S<sub>A</sub>) and nematic (N) liquid crystalline behavior. Conclusion shifted phase transition temperatures of the poly(In3AA-RedI) in the heating process are as follows: C → S<sub>A</sub> (161°C), S<sub>A</sub> → N (184°C) and N → I (231°C). Electrical conductivity of polymer [poly(In3AA-RedI)] and two of its copolymers [poly(In3AA-RedI-co-In) and poly(In3AA-RedI-co-Py)], has been studied by four probe methods and produced  $8.3 \times 10^{-4}$ ,  $6.4 \times 10^{-4}$  and  $4.7 \times 10^{-3}$  Scm<sup>-1</sup> conductivities, respectively.

**Key words:** Conducting polymers, electrical conductivity, liquid crystalline polymer, optical properties, optical materials, polyindole.

## INTRODUCTION

Conjugated polymers are well-known for their excellent electrical conductivities in oxidized (doped) state. The recent development of processable conducting polymers has opened the way for large-scale industrial applications. Conjugated polymers have been used widely in many areas such as rechargeable batteries (Heinze, 1991; Roth and Graupner, 1993), condensators (Mohammadi et al., 1986), diodes (Turut and Koleli, 1993; Kolelil et al., 1994), and sensors (Hosseini et al., 2005, 2006). Among these classes of polymers,

polyaniline, polypyrrole, polythiophene, etc. have been studied extensively because of their favorable processability and relative stability (MacDiarmid, 1997; Hosseini and Entezami, 2001, 2003). Heteroaromatic molecules containing nitrogen have very interesting properties. Polyindole is an electro active polymer, which can be obtained from electrochemical oxidation of indole or chemical oxidation using FeCl<sub>3</sub> or CuCl<sub>2</sub> (Xu et al., 2006). However, only little investigations have been made on chemically synthesized polyindole (John and

\*Corresponding author. E-mail: shhosseini@iiu.ac.ir, Tel: +98(9121374816).

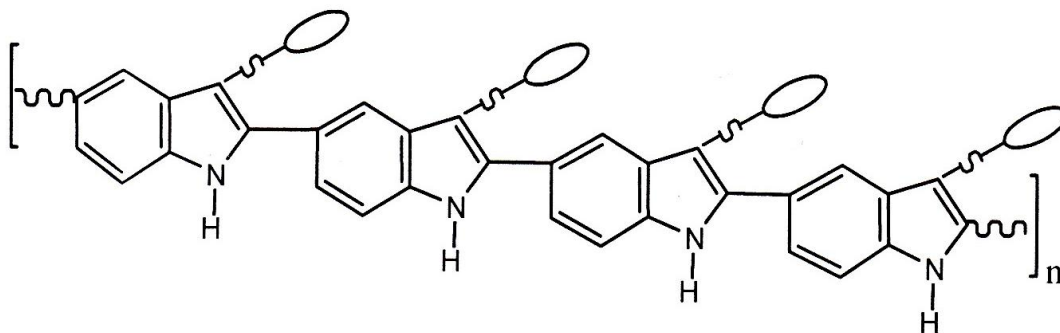


Figure 1. Side chain polyindole.

Palaniappan, 2005). The polymerization efficiency and the conductivity of polyindole are lower than the other known hetero atom containing conducting polymers such as polycarbazole, polyfuran, polyisothianaphene, polybithiophene, etc. Therefore, they did not attract much attention as the other types of conducting materials. There are two main procedures for the preparation of soluble conjugated polymers: one is the incorporation of relatively long and flexible side chains; another is the introduction of large counterions (Zaho and Wang, 2006).

Synthesis of three-substituted azobenzene-functionalized polyindoles has attracted much interest both from synthetic considerations as well as from materials science. Polyindoles with azobenzene groups in three-position will not only have better processability and stability, but also may possess novel electrical, electrochemical and optical properties. Thus, the combination of polyindole backbone with photoactive azobenzene groups can provide a new approach to develop other novel materials with unique electronic and optical properties. Azo chromophore has been demonstrated to be good photoisomerizable units (Matsui et al., 2001) for optical switching, image storage and other electrooptic devices. The introduction of photoresponsive moieties into liquid crystalline polymers is a useful method to provide the liquid crystal (LC) materials with photoresponsive properties. Hu and coworkers (Zhao et al., 2005) synthesized a series of novel LC azobenzene-functionalized polythiophenes with the aims of preparing liquid crystalline thiophene derivatives for photonic applications.

In the previous works, we synthesized a new liquid single crystal (Yousefi et al., 2008) and reported liquid crystalline polymer based N-substituted pyrrole (Hosseini and Mohammadi, 2009). This polymer exhibit liquid crystalline and electrically conductivity properties, as well. In this paper, polyindole was selected as a main chain skeleton. The side chain polyindole contains mesogenic group which shows liquid crystalline property. The 3-substituted of the indole ring was prepared and their liquid crystallinity and thermal properties investigated. Figure 1 shows side chain polyindole. So, a series of

novel LC azobenzene-functionalized polyindoles synthesized with the aims at preparation of liquid crystalline indole derivatives for photonic applications. The synthesis, characterization, and photoresponsive behavior of these chromophore-based LC polyindole derivatives were fully discussed. Molecular structure of the LC polyindole is illustrated in Figure 2, where LC group is introduced into 3-position of the indole unit. The polymer consists of main chain, flexible methylene spacer, linking group and tailing group, as shown in Figure 2.

## EXPERIMENTAL PROCEDURE

### Physical measurements

$^1\text{H}$ ,  $^{13}\text{C}$ -NMR spectra were recorded on a BRUKER 250 NMR spectrometer at 400 MHz in deuterated chloroform- $d_6$  or dimethylsulfoxide- $d_6$  with TMS as an internal standard. NMR data are reported in the following order: chemical shift (ppm), spin multiplicity (s=singlet, d=doublet, t=triplet, q=quartet, m=multiplet), and integration. Differential Scanning Calorimetry (DSC) analyses were performed at  $5^\circ\text{Cmin}^{-1}$  on a TA instruments using STA 625 DSC. FT-IR spectra were recorded on a 8101-M-Shimadzu and BRUKER-IF-66.5 spectrometer. Vibrational transition frequencies are reported in wave number ( $\text{cm}^{-1}$ ). The UV-Visible spectra were obtained using a UV-Vis recording spectrophotometer (Perkin-Elmer Lambda 15).

### Materials

Indole-3-acetic acid (Fluka), indole (Merck) and pyrrole (Fluka, 96%) were distilled prior to use. Tetrahydrofuran (Merck), petroleum ether and ethyl acetate were distilled and dried with molecular sieves ( $4\text{A}^\circ$ ) prior to use. 4-nitroaniline (Merck, 98%), dicyclohexyl carbodiimide (DCC) (Merck, 98%), 4-(dimethylamino)pyridine (DMAP) (Merck, 99%), 2-(N-ethyl aniline)ethanol (Merck, 99%), sodium nitrite ( $\text{NaNO}_2$ ) (Merck, 99%), methanol (Fluka) and the other materials used in this work were purchased from Merck chemicals and purified, or prepared according to literature methods.

### Preparation of 2-[N-ethyl-N-[4-[(4'-nitrophenyl)azo]-phenyl]amino] ethyl (Red1)

7 g (0.05 mol) of 4-nitroaniline was dissolved in a solution of 25 ml

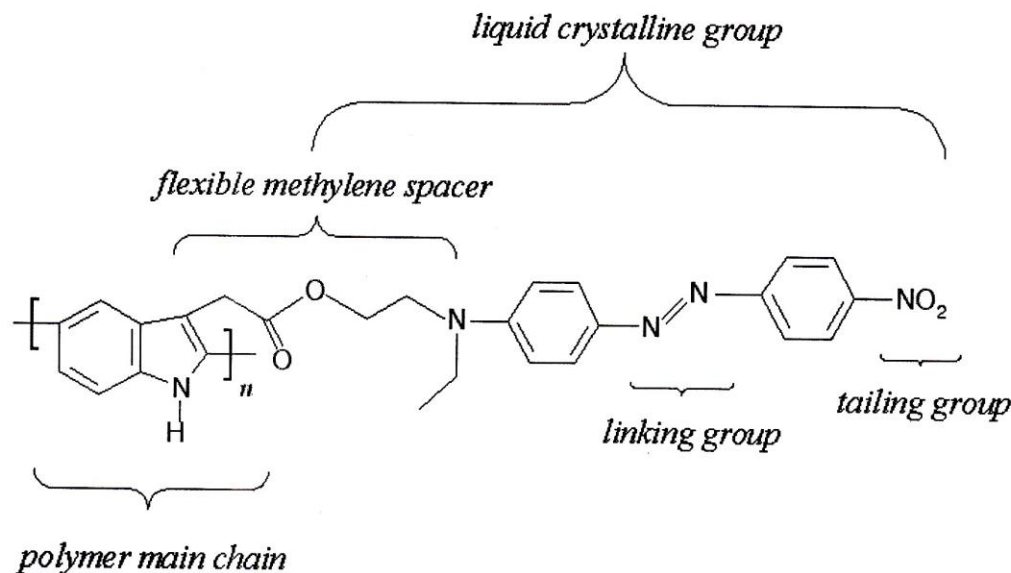


**Figure 2.** Molecular structure of liquid crystalline polyindole derivative.

of concentrated hydrochloric acid and 150 ml of water. The mixture was cooled to 0°C in an ice-water bath, and then a solution of 3.6 g (0.05 mol) of sodium nitrite in 15 ml of water was added dropwise. The resultant solution of diazonium salt was stirred for 30 min at 0–3°C. Another solution of 5 g (0.03 mol) of N-ethyl-N-hydroxyethyl aniline dissolved in 10 ml of hydrochloric acid (10%) was stirred for 5 min at 0°C. The above solution of diazonium salt was added into this solution within 30 min. The mixture was allowed to stand for 20 min. Then was neutralized with added NaOH solution with slowly and stirring. Reddish crystals were filtered on a Buchner funnel and recrystallised with 2-propanol. Compound 1 was obtained as crimson crystals. Yield 9 g-85%, mp: 170-173°C. UV (THF):  $\lambda_{\max}$ =310 nm (0.3 intensity), 470 nm (1.25 intensity). FT-IR (KBr pellets,  $\nu$  in  $\text{cm}^{-1}$ ): 3434 ( $\nu_{\text{OH}}$ ), 3200 ( $\nu_{\text{C-H}}$ , Ar), 2950 ( $\nu_{\text{C-H}}$ , Al), 1599 ( $\nu_{\text{N=N}}$ ), 1515, 1341 ( $\nu_{\text{NO}_2}$ ), 1450 ( $\nu_{\text{C=C}}$ ), 1141 ( $\nu_{\text{C-O}}$ ), 800-850 ( $\nu_{\text{C-H}}$ , OOP)  $\text{cm}^{-1}$ .  $^1\text{H-NMR}$  ( $\text{CDCl}_3$ ):  $\delta$  1.26 (3H, t), 1.75 (1H, s), 3.56 (2H, q), 3.62 (2H, t), 3.90 (2H, t), 6.81 (2H, d), 7.88 (2H, d), 7.92 (4H, d), 8.32 (2H, d) ppm.  $^{13}\text{C-NMR}$  ( $\text{CDCl}_3$ ):  $\delta$  12.1, 46.4, 52.8, 60.1, 112.3, 122.5, 124.7, 126.6, 143.8, 147.2, 151.6, 157.2 ppm.

#### Preparation of 2-[N-ethyl-N-[4-[(4'-nitrophenyl)azo]phenyl]amino]ethyl-3-indolyl acetate, (In3AA-RedI)

A total 2.275 g (0.013 mol) of indole-3-acetic acid and 3.454 g (0.011 mol) of RedI (crystallized in isopropyl alcohol) were dissolved in 50 ml of dry THF. Then 2.269 g (0.011 mol) of N, N-dicyclohexyl carbodiimide (DCC) and 0.0916 g (0.75 mmol) of 4-(dimethylamino) pyridine (DMAP) were added to the vigorously stirred solution. The stirring continued for 5 h. The mixture was then filtered, and the solvent was removed by rotary evaporator under vacuum. The product was purified by column chromatography (silica gel, petroleum ether: ethyl acetate=1:4, v/v), followed by recrystallization from petroleum ether/ethyl acetate to yield red crystals (compound 2 was obtained). Yield: 50%, mp: 138-140°C. UV (THF);  $\lambda_{\max}$  = 285 nm (0.70 intensity), 335 nm (0.4 intensity) and 535 nm (0.65 intensity). FT-IR (KBr pellets,  $\nu$  in  $\text{cm}^{-1}$ ): 3384 ( $\nu_{\text{N-H}}$ , In), 3100 ( $\nu_{\text{C-H}}$ , Ar), 2930 ( $\nu_{\text{C-H}}$ , Al), 1726 ( $\nu_{\text{C=O}}$ ), 1601 ( $\nu_{\text{N=N}}$ ), 1515, 1334 ( $\nu_{\text{NO}_2}$ ), 1627, 1458 ( $\nu_{\text{C=C}}$ ), 1139 ( $\nu_{\text{C-O}}$ ), 828 ( $\nu_{\text{C-H}}$ , OOP)  $\text{cm}^{-1}$ .  $^1\text{H-NMR}$  ( $\text{d}^6$ -DMSO):  $\delta$  1.06 (3H, t), 2.50 (2H, d), 3.43 (2H, q), 3.74

(2H, t), 4.28 (2H, t), 6.93 (2H, d), 7.81 (2H, d), 7.94 (2H, d), 8.36 (2H, d), 7-7.5 (5H indole, m) 10.85 (1H, s) ppm.  $^{13}\text{C-NMR}$  ( $\text{d}^6$ -DMSO):  $\delta$  12.4, 31.5, 45.4, 48.8, 62.2, 106.6, 111.9, 112.1, 118.4, 119, 121.6, 123, 124.6, 125.4, 126.5, 127, 137, 147.6, 149.5, 152.7, 157.5, 172 ppm.

#### Preparation of Poly{2-[N-ethyl-N-[4-[(4'-nitrophenyl)azo]phenyl]amino]ethyl-3-indolyl acetate}, Poly(In3AA-RedI)

Polymerization was carried out as follows: 0.5 g (1.06 mmol) of monomer (In3AA-RedI) in 25 ml THF was added dropwise to a suspension 1.126 g, (3.18 mmol) of  $\text{Fe}(\text{ClO}_4)_3$  in 20 ml of THF under nitrogen atmosphere. The mixture was stirred at 50°C temperature for 24 h. The polymerization mixture was added dropwise into 100 ml of methanol. The precipitates were filtered, dissolved in 5 ml of THF, and reprecipitated into 100 ml of methanol. This procedure was repeated three times until the unreacted monomer was completely removed. Finally, the polymer was dried under vacuum at 25°C to constant weight (Compound 3 was obtained). UV (THF):  $\lambda_{\max}$ =280 nm (1 intensity), 330 nm (0.3 intensity), 475 nm (0.2 intensity) and 680 nm (0.4 intensity). FT-IR (KBr pellets,  $\nu$  in  $\text{cm}^{-1}$ ): 3383 ( $\nu_{\text{N-H}}$ , indole), 3200 ( $\nu_{\text{C-H}}$ , aromatic), 2917 ( $\nu_{\text{C-H}}$ , aliphatic), 1750 ( $\nu_{\text{C=O}}$ ), 1627 ( $\nu_{\text{N=N}}$ ), 1514, 1335 ( $\nu_{\text{NO}_2}$ ), 1100 ( $\nu_{\text{C-O}}$ )  $\text{cm}^{-1}$ .  $^1\text{H-NMR}$  ( $\text{d}^6$ -DMSO):  $\delta$  1.09 (3H, t), 1.24 (2H, d), 3.63 (2H, q), 3.72 (2H, t), 4.27 (2H, t), 6.88-7.36 (6H, m), 7.82 (2H, d), 7.95 (2H, d), 8.38 (2H, d), 10.91 (1H, s) ppm.  $^{13}\text{C-NMR}$  ( $\text{d}^6$ -DMSO):  $\delta$  11.8, 30.6, 44.8, 48.2, 61.6, 106.6, 111.3, 111.6, 118.3, 118.4, 121.0, 122.4, 124.1, 124.8, 126.0, 127.0, 136.0, 142.8, 146.8, 151.5, 155.1, 171.5 ppm.

#### Preparation of Poly{2-[N-ethyl-N-[4-[(4'-nitrophenyl)azo]phenyl]amino]ethyl-3-indolyl acetate-co-indole}, Poly(In3AA-RedI-co-In)

The typical synthesis procedures utilized can be described as follows: 0.1 g (0.2123 mmol) of monomer (In3AA-RedI) and 0.0248 g (0.2123 mmol) of monomer indole in 10 ml of THF was added dropwise to a suspension 0.1503 g (0.4246 mmol) of  $\text{Fe}(\text{ClO}_4)_3$  in

10 ml of THF under nitrogen atmosphere. The mixture was stirred at 50°C temperature for 24 h. The copolymer in solution was precipitated by addition of excess methanol. The precipitate was extracted using boiling absolute ethanol. The precipitate was dried under vacuum. FT-IR (KBr pellets,  $\nu$  in  $\text{cm}^{-1}$ ),  $\nu$ : 3429 ( $\text{U}_{\text{N-H}}$ , In), 3200 ( $\text{U}_{\text{C-H}}$ , Ar), 2927 ( $\text{U}_{\text{C-H}}$ , Al), 1738 ( $\text{U}_{\text{C=O}}$ ), 1627 ( $\text{U}_{\text{N=N}}$ ), 1515, 1335 ( $\text{U}_{\text{NO}_2}$ ), 1150 ( $\text{U}_{\text{C-O}}$ )  $\text{cm}^{-1}$ .  $^1\text{H-NMR}$  ( $d^6$ -DMSO):  $\delta$  1.17-1.3 (broad), 1.3-1.9 (broad), 6.5-9 (broad) ppm.

#### Preparation of Poly(2-[N-ethyl-N-[4-[(4'-nitrophenyl)azo]phenyl]amino] ethyl-3-indolyl acetate-co-pyrrole), Poly(In3AA-Redl-co-Py)

Poly(In3AA-Redl-co-Py) was synthesized using the same synthetic procedures as for Poly(In3AA-Redl-co-In). The (In3AA-Redl) monomer (0.1 g, 0.2123 mmol) and pyrrole (0.0142 g, 0.2123 mmol) in anhydrous tetrahydrofuran (10 mL) was added dropwise to a suspension of  $\text{Fe}(\text{ClO}_4)_3$  (0.1503 g, 0.4246 mmol) in tetrahydrofuran (10 ml) under nitrogen. The mixture was stirred at 50°C temperature for 24 h. The polymer in solution was precipitated by addition of excess methanol. The precipitate was extracted using boiling absolute ethanol. The precipitate was dried under vacuum. FT-IR (KBr pellets,  $\nu$  in  $\text{cm}^{-1}$ ),  $\nu$ : 3250 ( $\text{U}_{\text{N-H}}$ , indole), 3100 ( $\text{U}_{\text{C-H}}$ , aromatic), 2989 ( $\text{U}_{\text{C-H}}$ , aliphatic), 1745 ( $\text{U}_{\text{C=O}}$ ), 1603 ( $\text{U}_{\text{N=N}}$ ), 1516, 1414 ( $\text{U}_{\text{NO}_2}$ ), 1103 ( $\text{U}_{\text{C-O}}$ ), 828 ( $\text{U}_{\text{C-H}}$ , oop)  $\text{cm}^{-1}$ .

## RESULTS AND DISCUSSION

All synthetic routes of Redl, In3AA-Redl and poly(In3AA-Redl) shown are in Scheme 1. Therefore, schematic copolymerization of In3AA-Redl with indole and pyrrole has been shown in Scheme 2.

### Structural characterization

In order to obtain polymers with higher molecular weights, the polymerization and copolymerization were carried out at 50°C temperature with dropwise addition of monomers. This polymer was found to be soluble in chloroform, THF and methylene chloride, but two copolymers synthesized by chemical oxidative copolymerization using  $\text{Fe}(\text{ClO}_4)_3$  are not soluble in common organic solvents. Figure 3 illustrates the FT-IR spectra of poly(In3AA-Redl). The peaks of about 3100-3600, 3020 and 2917  $\text{cm}^{-1}$  was related to N-H, C-H (aromatic) and C-H (aliphatic) stretching vibrations, respectively. The peaks at around 1750 and 1100  $\text{cm}^{-1}$  are due to the carbonyl (C=O) stretching vibration and C-O-C stretching vibration respectively.

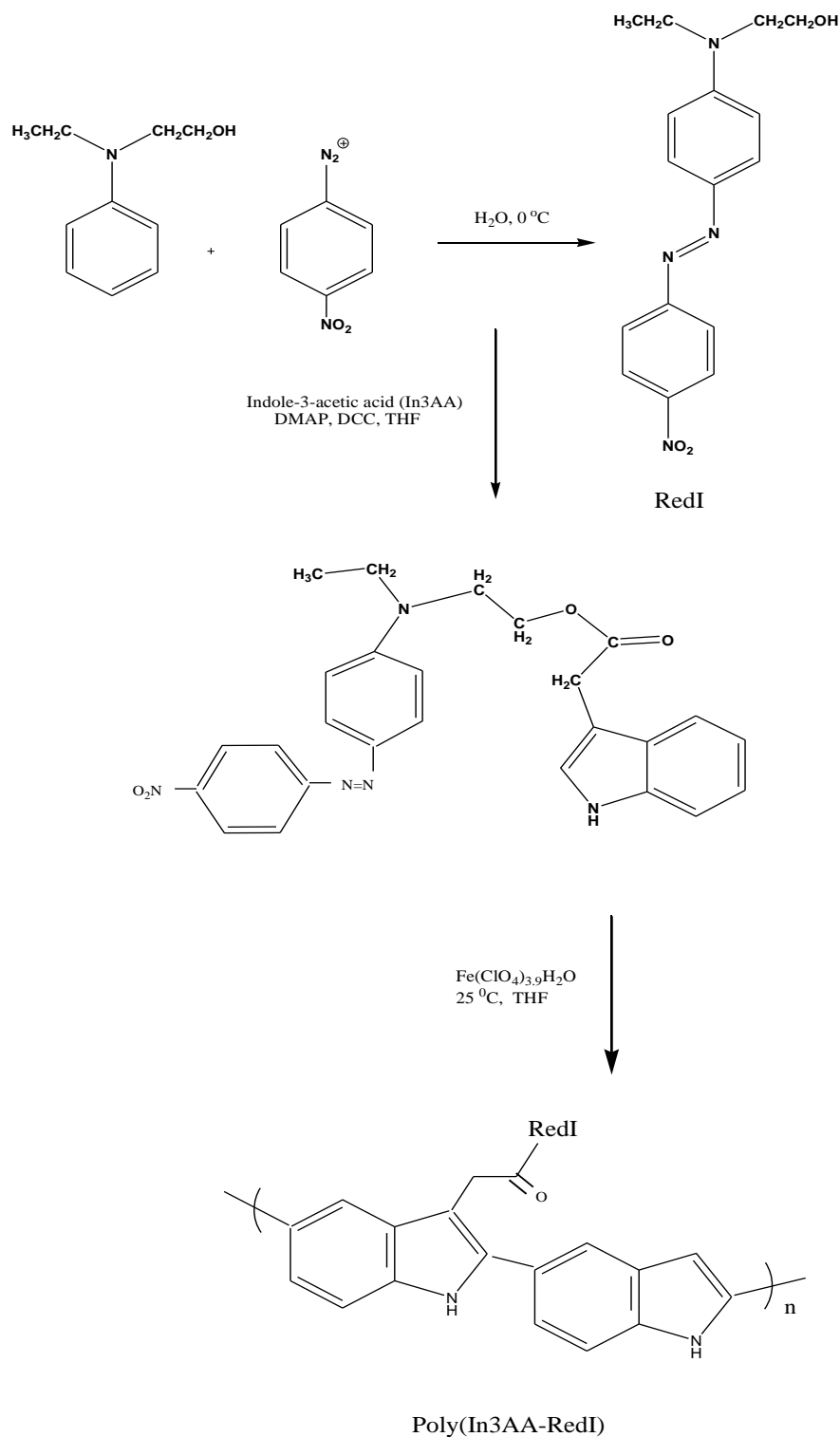
Figure 4 shows the  $^1\text{H-NMR}$  spectrum of poly(In3AA-Redl). On the basis of comparison with the spectrum of monomer, we can assign the following peaks for poly(In3AA-Redl): 1.09 ( $-\text{CH}_3$ ), 1.24 ( $-\text{CH}_2-\text{COO}-$ ), 2.52 (DMSO), 3.31 ( $\text{H}_2\text{O}$ ), 3.63 ( $-\text{CH}_2-\text{CH}_3$ ), 3.72 ( $-\text{CH}_2-\text{N}$ ), 4.27 ( $-\text{O}-\text{CH}_2-$ ), 7.37, 7.82, 7.95 and 8.38 ppm (protons of phenylene groups). The lines refer to the aromatic protons of the indole ring that are located at 6.88-7.36 and 10.85 (H-N) ppm. The oxidative polymerization of  $\beta$ -

substituted indole monomer with  $\text{Fe}(\text{ClO}_4)_3$  always leads to two different types of couplings: head-to-tail and head-to-head. Thus, the  $\alpha$ -methylene protons directly attached to the indole ring ( $\beta$ -position) and can be incorporated into a polymer chain with the above two diads. The two peaks located at 1.2-1.5 ppm arise from the methylene protons between the ester group and the indole ring, showing that poly(In3AA-Redl) has a stereo random chain structure with almost equal distribution of head-to-tail and head-to-head linkages along the polymer chain.

The  $^{13}\text{C-NMR}$  spectrum of the poly(In3AA-Redl) is shown in Figure 5. Using INEPT-pulse sequence, we were able to distinguish the proton bonded carbons from all other carbons present in the molecule. On the basis of a comparison with the spectra of poly(In3AA-Redl), the following assignments are proposed: The line at the lowest field (171.5 ppm) corresponds to the carbon of the ester group. The lines at 155.1, 151.5, 146.8, 142.8, 125.0, 124.8, 122.4 and 111.6 ppm are assigned to the aromatic carbons in the Redl moiety. The remaining eight lines at 136.0, 127.0, 124.1, 121, 118.4, 118.3, 111.3 and 106.6 ppm originate from the carbons of the indole ring. In the aliphatic part, the lines of low intensity at 11.2, 30.6, 44.8, 48.2 and 61.6 ppm correspond to the Redl substituent. The peaks are located at 38-40 ppm arise from the  $d^6$ -DMSO solvent.

Figure 6 shows  $^1\text{H-NMR}$  spectrum of the polymer poly(In3AA-Redl-co-In) in ( $d^6$ -DMSO) solvent. In this spectrum, peaks of aliphatic protons ( $-\text{CH}_3$ ), ( $-\text{CH}_2-\text{COO}-$ ) and ( $-\text{CH}_2-\text{CH}_3$ ) observed in 1.1 to 2.2 ppm. Peak of protons ( $-\text{CH}_2-\text{N}$ ) and ( $-\text{O}-\text{CH}_2-$ ) are not observed in spectra, because of overlap with peak of DMSO and water around 2.49 and 3.3 ppm, respectively. Protons of aromatic ring and indole are characterized between 6.5 to 8 ppm. Of course peaks of aromatic ring are not clear precisely because they are blocked copolymer, but they appeared in the area related to aromatic compounds. Copolymer has a low solubility, so  $^1\text{H-NMR}$  is not clear. The great adherence of peak is a result of the greater involvement of indole monomers than In3AA-Redl monomer in polymeric chain. The peaks in aromatic region confirm performance of copolymerization.

Figure 7(a) shows UV-Visible spectrum of In3AA-Redl in THF as a solvent. According to Figure 7a, the In3AA-Redl as a monomer has three peaks in 285, 335 and 535 nm. The first absorption band is related to an  $n \rightarrow \pi^*$  transition and the second one is associated with a  $\pi \rightarrow \pi^*$  transition. Upon UV irradiation, a trans-cis isomerization is induced, leading to two absorption bands centered near 335 and 535 nm, respectively. The photochemical properties of the poly(In3AA-Redl) were examined also in THF as a solvent (Figure 7b). As can be seen in Figure 7b, the poly(In3AA-Redl) exhibits an absorption band centered at 280 nm which is related to the  $\pi \rightarrow \pi^*$  transition of trans configuration of the azobenzene moieties and a broad absorption bands around 550-750 nm which can be related to the  $\pi \rightarrow \pi^*$  transition of the highly conjugated



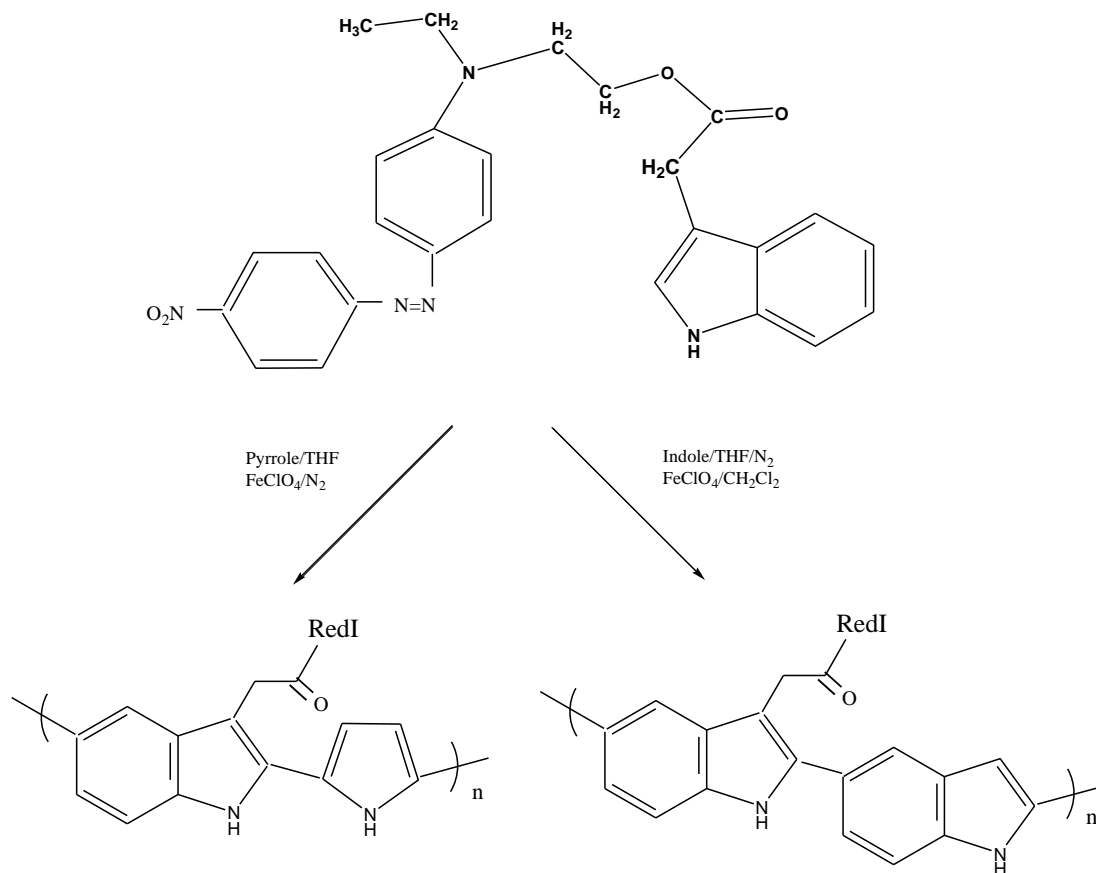
**Scheme 1.** Schematic reactions for route synthesis of Poly(In3AA-RedI).

polyindole units. Because of low solubility of poly(In3AA-RedI-co-In) and poly(In3AA-RedI-co-Py), we were not able to investigate UV-Visible or  $^{13}\text{C}$ -NMR spectra of them.

#### Liquid crystalline and thermal properties

Liquid crystallinity and thermal analysis of the polymer were conducted by optical absorption, optical polarizing





**Scheme 2.** Schematic reactions for copolymerization of poly(In3AA-RedI) with pyrrole and indole.

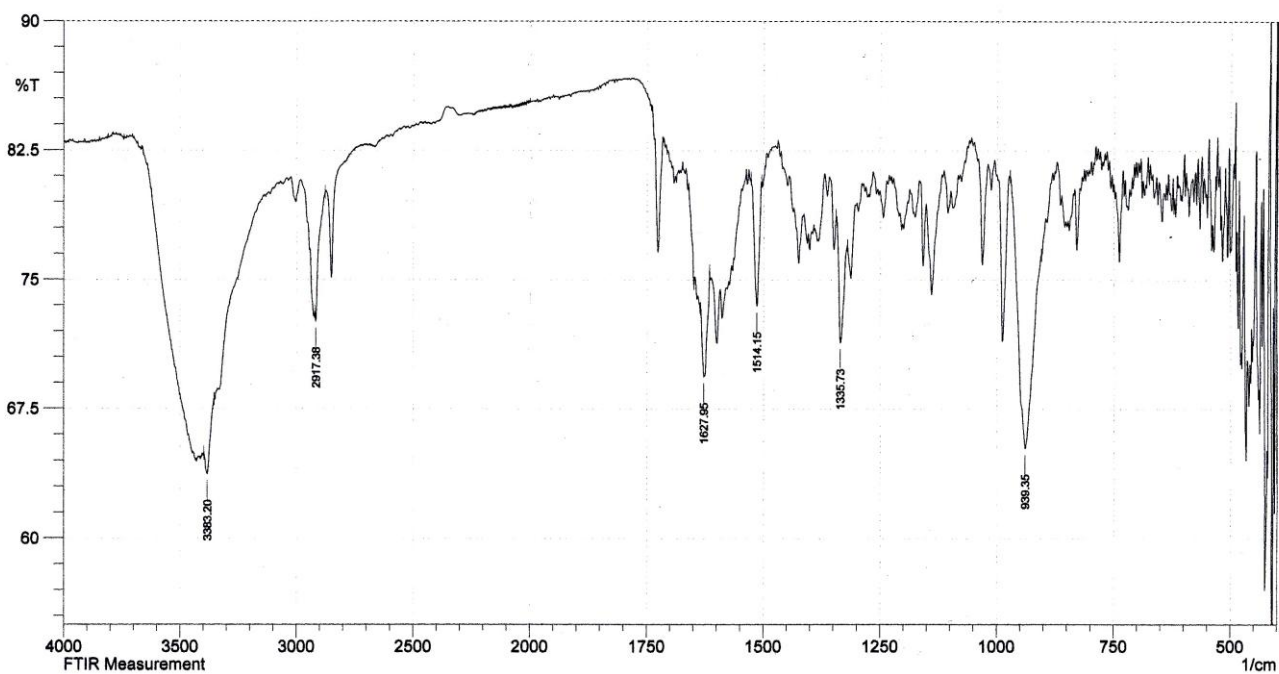


**Figure 3.** FT-IR Spectrum of poly(In3AA-RedI).

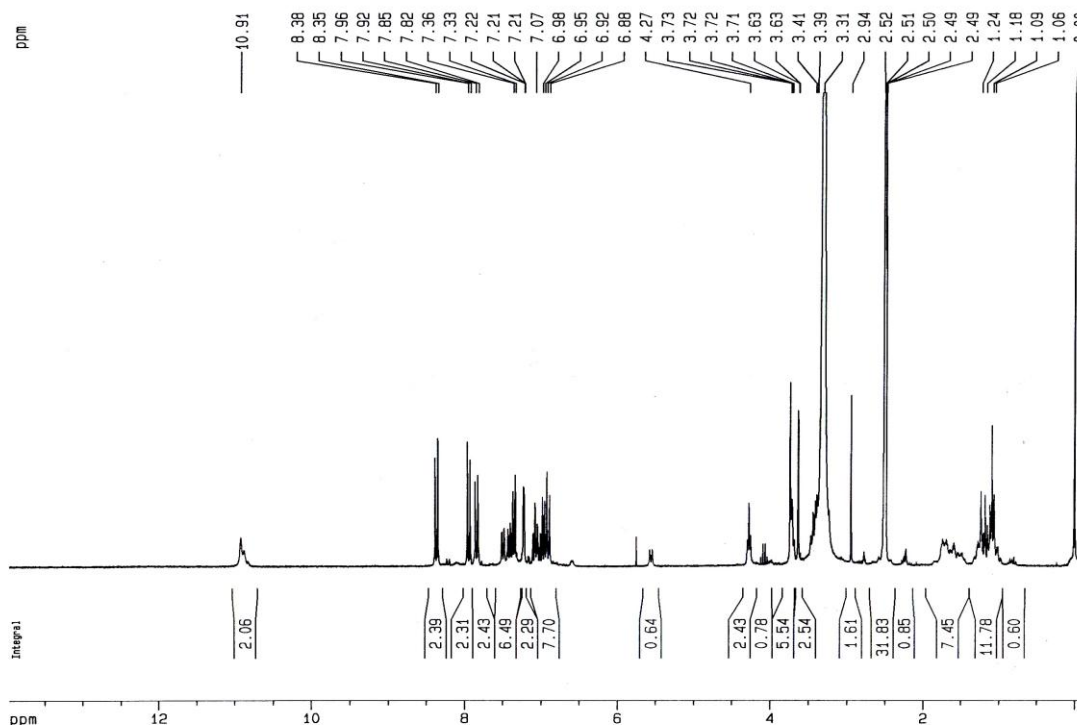


Figure 4. FT<sup>1</sup>H-NMR Spectra of poly(In3AA-RedI).

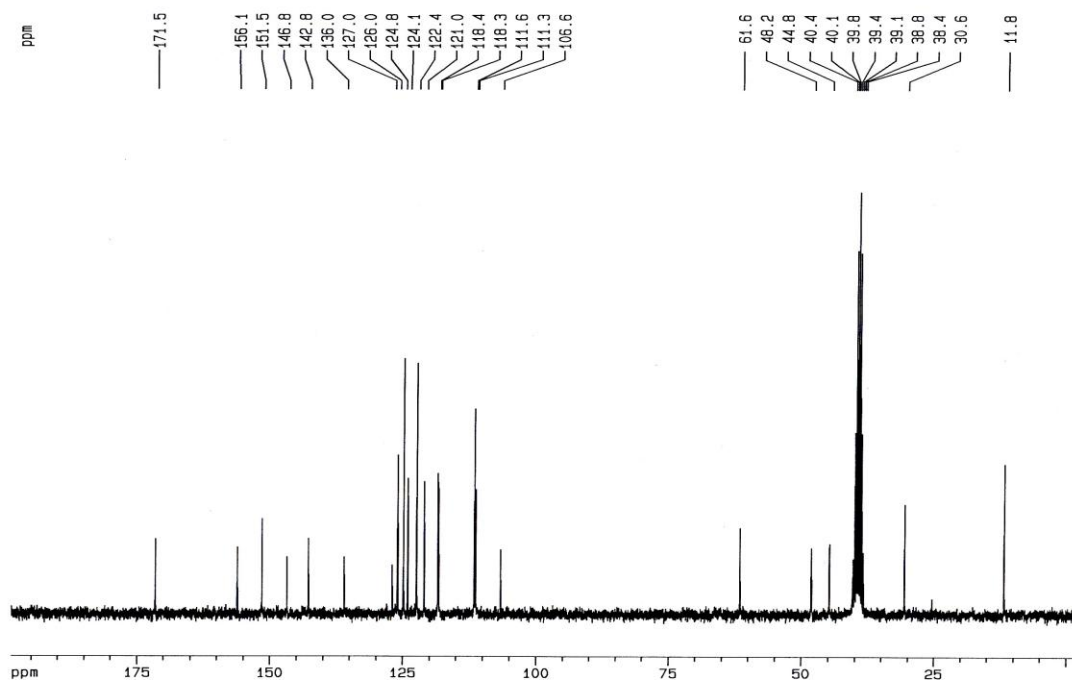


Figure 5. FT<sup>13</sup>C-NMR Spectrum of poly(In3AA-RedI).

microscope, and differential scanning calorimetry (DSC). Phase transition temperatures were determined by DSC

measurement. All DSC runs in this research were made under nitrogen atmosphere with a heating rate of

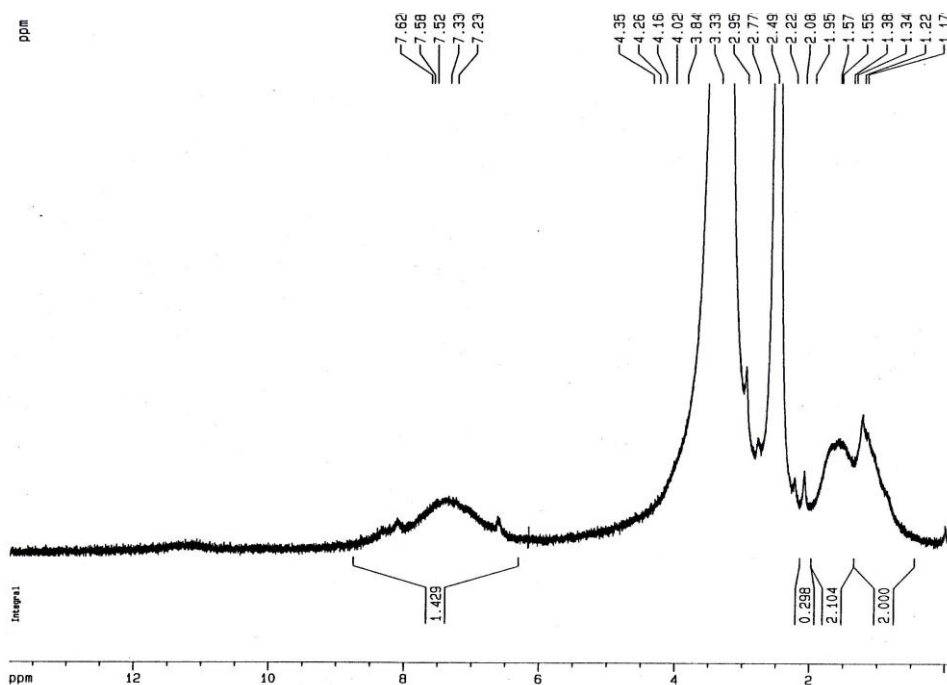


Figure 6. FT<sup>1</sup>H-NMR Spectra of poly(In3AA-Redl-co-In).

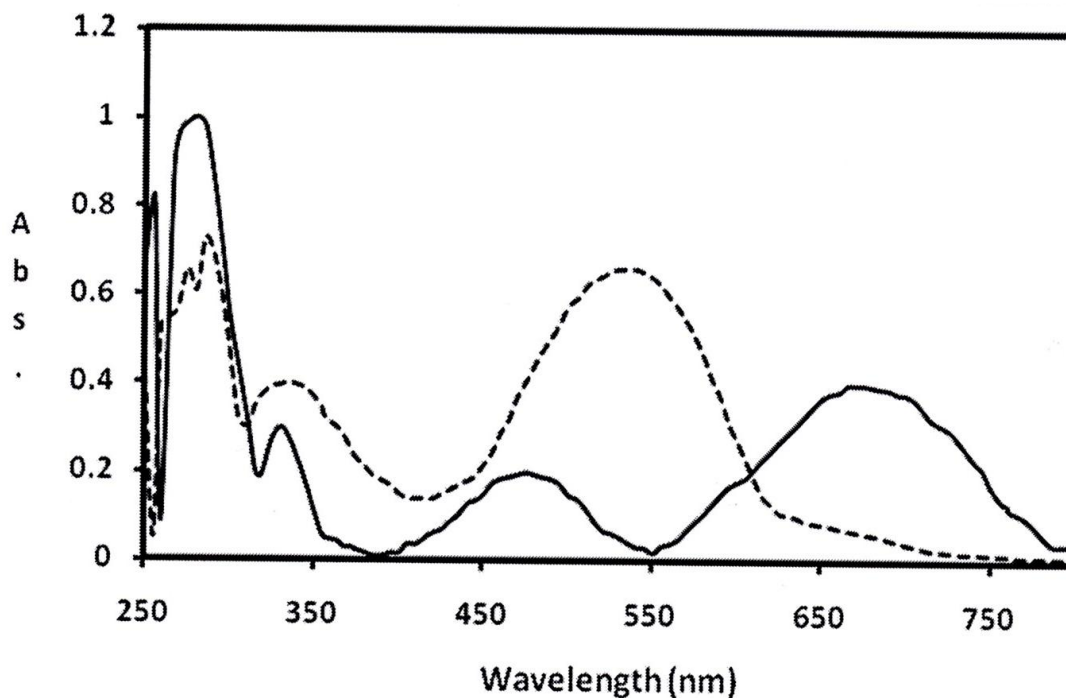
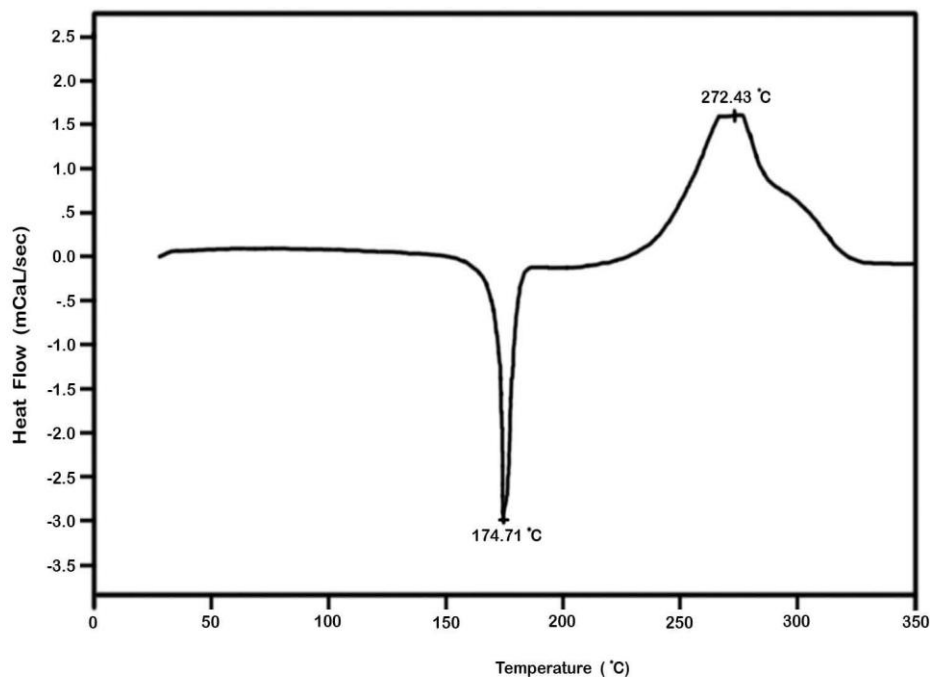


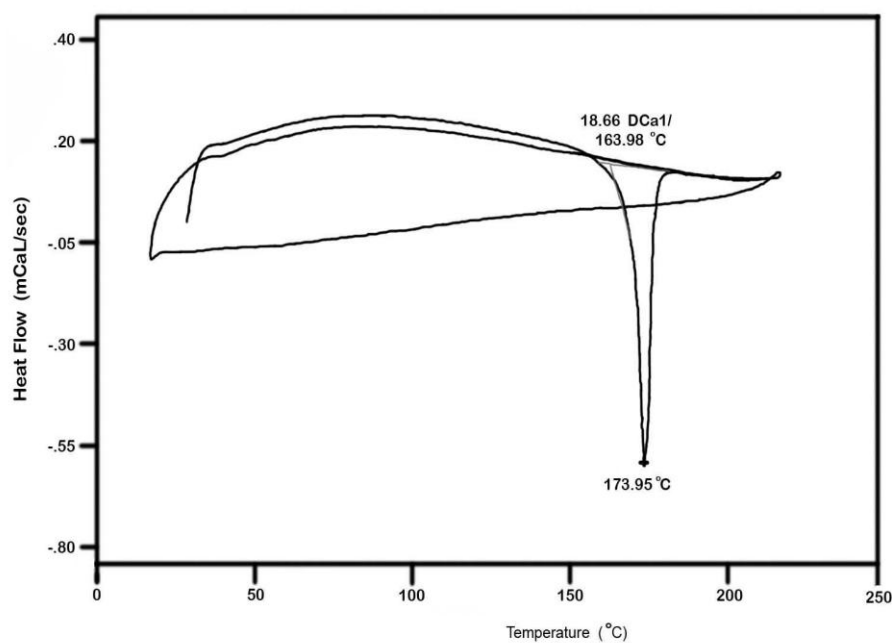
Figure 7. UV-Visible spectra of a) In3AA-Redl (...) and b) poly(In3AA-Redl) (-).

5°C/min. DSC thermograms of Redl in heating and cooling process are shown in Figures 8(a, b). Figure 8a shows thermogram and endothermic peak at 174.71°C

which is related to the melting process of Redl and also a transformation of crystalline phase to isotropic state. Crystalline phase of this compound is changed directly to



(a)



(b)

**Figure 8.** DSC Thermogram of RedI a) heating and b) heating and cooling with rate of 5°C/min.

isotropic liquid as a result of temperature effect. Therefore, it shows exothermic peak at 272.43°C which is related to the degrading process of RedI. In cooling process no peak is observed probably because the sample decomposition occurs at higher temperature or it does not have clear LC behaviour. By heating the sample

again no peak is observed, this confirms probable sample decomposition (Figure 8b).

Transition temperatures for poly(In3AA-RedI) were obtained using DSC shown as in Figure 9. DSC Thermogram of poly(In3AA-RedI) showed 5 glass transition temperature about 59, 91, 151, 181 and 231°C.

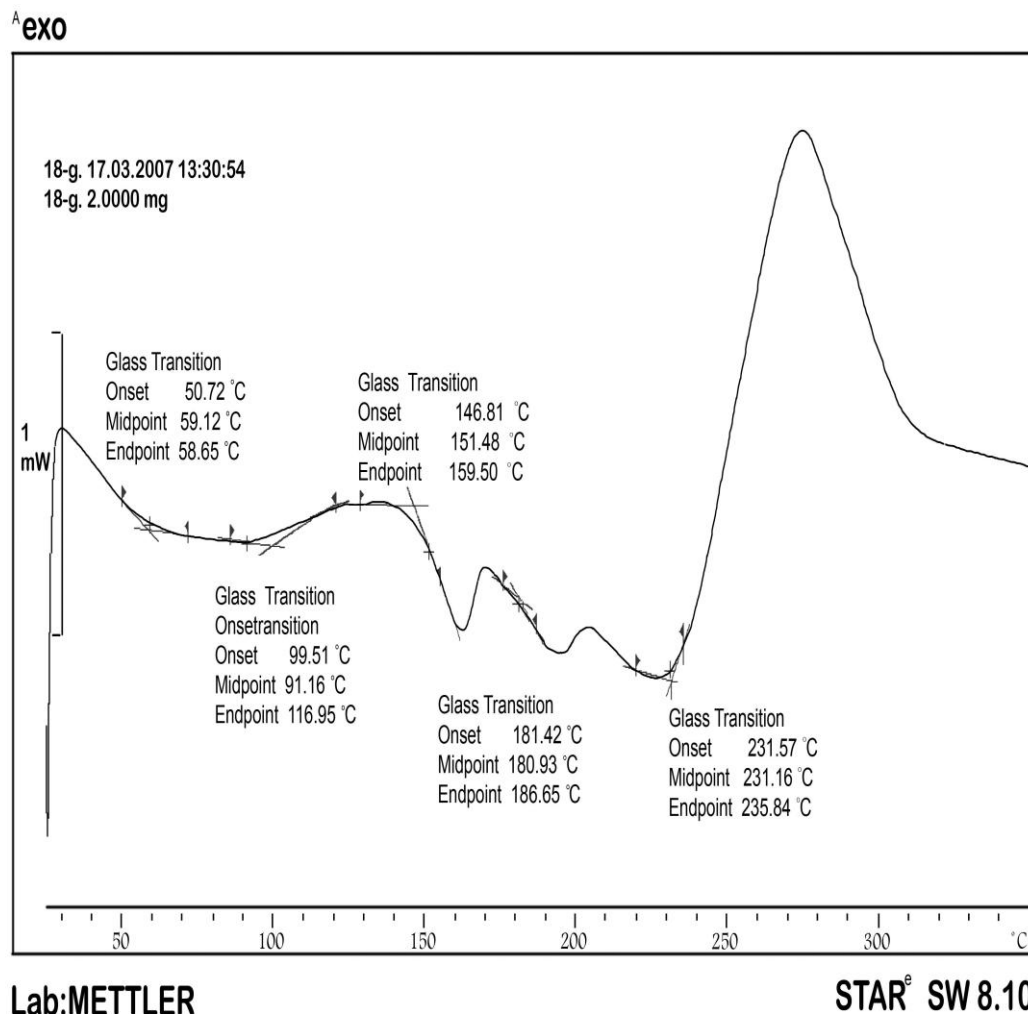


**Figure 9** DSC Thermogram of poly(In3AA-RedI) with rate of 5°C/min.

Therefore, it has three endothermic peaks. The first endothermic peak at 162°C is an indication of changing of crystalline phase to smectic A liquid crystalline state (C→S<sub>A</sub>). The second peak at 193°C is related to the changing of smectic A liquid crystalline mesophase to nematic state (S<sub>A</sub>→N). The last observed endothermic peak in this curve is about 225°C that is related to transition phase of nematic liquid crystalline to isotropic liquid (N→I). In the first and the second transitions, the stability of liquid crystalline mesophases are about 31°C and 32°C, respectively. The images of polarizing optical microscope of poly(In3AA-RedI) demonstrate the smectic A, nematic and isotropic liquid crystalline state in the ranges 150-168°C and 184-201°C and 205-236°C temperatures respectively. This indicates that poly(In3AA-RedI) is a monotropic or isotropic compound. Typical crystalline, smectic A, nematic textures and isotropic state of poly(In3AA-RedI) are shown in Figure 10(a-f).

## Conclusion

In this paper, we have described the preparation and investigation of liquid crystalline polyindole with azobenzene group in side chain. The results indicate that these azobenzene-functionalized polyindole derivatives have wide mesophase temperature ranges. DSC thermogram of poly(In3AA-RedI) showed 5 semi glass transition and three endothermic peaks. The endothermic peaks are indicative of changing of C→S<sub>A</sub>, S<sub>A</sub>→N and N→I. Images of polarizing optical microscope of poly(In3AA-RedI) demonstrated the smectic A, nematic and isotropic liquid crystalline states. Chemical, structural, thermal and morphological studies indicated that high quality polymer film can be obtained. As-formed polymer film was thoroughly soluble in polar solvent such as DMSO. According to IR and <sup>1</sup>H-NMR spectra, the existence of N-H bond implies that coupling between the monomer units occurred at the C2 and C5 positions.

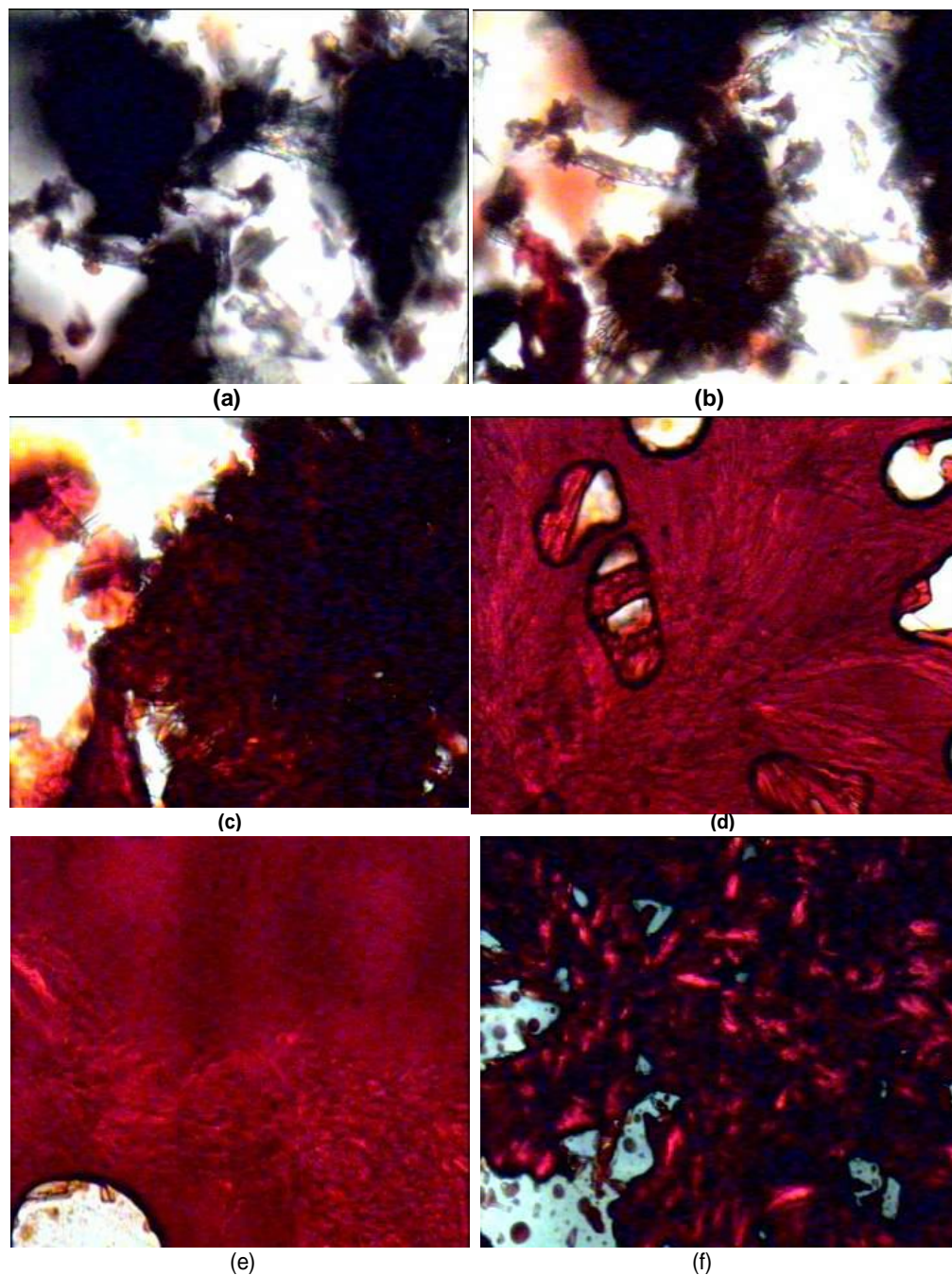


**Figure 10.** Cross-polarized optical micrograph of the polymer sample, smectic C phase a) 152°C, b) 160°C, c) 170°C, d) 185 °C, e) 195°C and f) 205°C.

## REFERENCES

- Heinze J (1991). Electrochemistry of conducting polymers. *Synth. Met.* 43(1-2):2805-2823.
- Hosseini SH (2006). Investigation of sensing effects polystyrene graft polyaniline for cyanide compounds. *J. Appl. Polym. Sci.* 101(6):3920-3926.
- Hosseini SH, Abdi Oskooe SH, Entezami AA (2005). Toxic Gas and Vapour Detection with Polyaniline Gas Sensors. *Iranian Polym. J.* 14(4):333-343.

- Hosseini SH, Entezami AA (2001). Chemical and electrochemical synthesis of polymer and copolymers of 3-methoxyethoxythiophene with aniline. *Polym. Adv. Technol.* 12:524-534.
- Hosseini SH, Entezami AA (2003). Chemical and electrochemical synthesis of conducting polyDi-heteroaromatics from pyrrole, indole, carbazole and their mixed containing hydroxamic acid groups and studies of its metal complexes. *J. Appl. Polym. Sci.* 90:63-71.
- Hosseini SH, Mohammadi M (2009). Preparation and characterization of new polypyrrole having side chain liquid crystalline moieties. *Mater. Sci. Eng. C.* 29:1503-150.

- John A, Palaniappan S (2005). Synthesis and characterization of soluble poly (N-heptylindole). *Polymer* 49:12037-12039.
- Koleli F, Saglam M, Turut A (1994). Polyindole Based Schottky. *Turk J Chem* 18(1):22-28.
- MacDiarmid AG (1997). Poly aniline and polypyrrole: Where are we headed?. *Synth. Met.* 84:27-34.
- Matsui T, Nagata T, Ozaki M, Fujii A, Onoda M, Teraguchi M (2001). Novel properties of conducting polymers containing azobenzene moieties in side chain. *Synth. Met.* 119:599-600.
- Mohammadi A, Hassan MA, Liedberg B, Hungstorm L, Saleneck R (1986). Chemical vapour deposition (cvd) of conducting polymers: polypyrrole. *Synth. Met.* 14:189-197.
- Roth S, Graupner W (1993). Conductive polymers: Evaluation of industrial applications. *Synth. Met.* 57:3623-3631.
- Turut A, Koleli F (1993). Metallic polythiophene/inorganic semiconductor Schottky diodes. *Phys. B.* 192:279-283.
- Xu J, Hou J, Zhang S, Zhang R, Nie G, Pu S (2006). Electrosynthesis of high quality poly(5-methylindole) films in mixed electrolytes of boron trifluoride diethyl etherate and diethyl ether. *Eur. Polym. J.* 42:1384-1395.
- Yousefi M, Hosseini SH, Amani V, Khavasi HR (2008). (E)-2-(N-ethyl-4-[(4-nitrophenyl)diazenyl]aniline)ethyl acrylate. *Acta. Cryst. E*64:o789.
- Zhao X, Wang M (2006). Synthesis and photoresponsive behavior of azobenzene-functionalized polythiophene film. *Eur. Polym. J.* 42:247-253.
- Zhao X, Hu X, Zheng PJ, Gan LH, Lee CKP (2005). Synthesis and characterization azobenzene as side chain. *Thin Solid Films.* 477:88-94.



Full Length Research Paper

# Almost quaternionic integral submanifolds and totally umbilic integral submanifolds

Fatma Özdemir

Department of Mathematics, Faculty of Science and Letters, Istanbul Technical University,  
 34469 Maslak-Istanbul, Turkey.

Accepted 22 August, 2013

In this work, we consider a Riemannian manifold which admits an integrable distribution  $P$  with an almost quaternionic structure  $V$ . We show that the torsion tensor of an almost quaternionic structure  $V$  is independent of the choice of bases. We prove that the integral submanifolds are totally umbilic under the condition of the conjugate shape operator  $C\tilde{L}_Z$  is skew-adjoint. We give another condition for the shape operator  $\tilde{L}_Z$  of  $P$  to be quaternionic linear.

**Key words:** Subbundle, almost complex structure, almost quaternionic structure, shape operator.

**MSC 2010.** 53C55, 53C15.

## INTRODUCTION

In literature (Kobayashi and Nomizu, 1963, 1969; Yano and Ako, 1972; Ishihara, 1974; Özdemir, 2006; Alagöz et al., 2012), almost complex and almost quaternionic structures have been investigated widely. These structures are special structures on the tangent bundle of a manifold. A detailed review can be found in Kirichenko and Arseneva (1997). Let us recall some basic facts and definitions from literature. In this work, by a manifold, we mean a smooth manifold, that is, a Hausdorff space with a fixed complete atlas compatible with the pseudo group

of transformations of class  $C^\infty$  of  $R^n$ . Also, vector fields and plane fields are all supposed to be smooth. We denote by  $\chi(M)$  the algebra of vector fields on a manifold  $M$ .

An almost complex structure on a manifold  $M$  is a tensor field  $J: TM \rightarrow TM$  satisfying the relation  $J^2 = -I$ , where  $I$  denotes the identity transformation of  $T_x(M)$ . An almost hypercomplex structure on a  $4m$ -dimensional manifold  $M$  is a bundle  $S = (F, G, H)$  of almost complex structures  $F$ ,  $G$  and  $H$  satisfying the conditions

$$F^2 = G^2 = H^2 = -I, \quad H = FG, \quad FG + GF = FH + HF = GH + HG = 0 \quad (1)$$

We now consider a  $4m$ -dimensional Riemannian manifold  $M$  admitting a three dimensional subbundle  $V$

of the bundle of (1,1) tensors such that on a neighborhood  $U$  of each  $x \in M$ ,  $V$  has a local base  $\{F, G, H\}$ . If on each such neighborhood the tensors  $F$ ,  $G$  and  $H$  satisfy the conditions 1, then the bundle  $V$  is called an almost quaternionic structure on  $M$  (Ishihara, 1974). The Nijenhuis bracket or torsion tensor of tensor fields  $A$  and  $B$  of type (1,1) is a tensor field of type (1,2) and defined by:

$$[A, B](X, Y) = [AX, BY] - A[BX, Y] - B[AX, Y] + [BX, AY] - B[AX, Y] - A[X, BY] + (AB + BA)[X, Y]. \tag{2}$$

The famous Newlander-Nirenberg Theorem states that an almost complex structure is a complex structure if and only if it is integrable; that is, it has no torsion (Yano and Ako, 1972). Thus, if the tensor fields  $F$ ,  $G$  and  $H$  are integrable, then the Nijenhuis bracket of any two of them vanish (Yano and Ako, 1972); that is,

$$[F, F] = [G, G] = [H, H] = 0 \quad \text{and} \\ [F, G] = [H, F] = [G, H] = 0. \tag{3}$$

If any two of six Nijenhuis tensors are zero, then the others vanish too. It is shown that if any of Nijenhuis tensors vanish, then there exists a torsion-free connection  $\nabla$  such that  $F$ ,  $G$  and  $H$  are covariantly constant with respect to the connection, that is,  $\nabla F = \nabla G = \nabla H = 0$ , which means that  $V$  is a trivial bundle (Yano and Ako, 1972).

In this work, we consider an almost quaternionic manifold  $M$  having an integrable distribution  $P$  with an almost quaternionic structure  $V$ , and we prove that the torsion tensor of an almost quaternionic structure  $V$  is well-defined. By defining the shape operator  $\tilde{L}_Z$  of  $P$ , we state and prove that the conjugate shape operators of the tensors  $F$ ,  $G$ , and  $H$  are skew-adjoint if and only if they are quaternionic linear. Furthermore, we prove that if the integral submanifolds are totally umbilic then conjugate shape operators are skew-adjoint.

**ALMOST QUATERNIONIC SUBSTRUCTURES**

We quote the definition of the torsion of bundle of  $V$  from (Özdemir, 2006) as:

$$[V, V] = [F, F] + [G, G] + [H, H] \tag{4}$$

where  $[, ]$  denotes the Nijenhuis bracket.

We now state the following theorem about the torsion tensor of  $V$ .

**Theorem 1**

The torsion tensor of the bundle  $V$  is well defined. That is,  $[V, V]$  is independent of the choice of bases.

**Proof**

Let  $\{F', G', H'\}$  and  $\{F, G, H\}$  be local bases for  $V$  defined on neighborhoods  $U$  and  $U'$ , respectively, and assume that  $U \cap U' \neq \emptyset$ . Since  $U$  and  $U'$  are not disjoint, then in  $U \cap U'$  we have

$$F' = a_{11}F + a_{12}G + a_{13}H, \tag{5}$$

$$G' = a_{21}F + a_{22}G + a_{23}H, \tag{6}$$

$$H' = a_{31}F + a_{32}G + a_{33}H, \tag{7}$$

where  $a_{ij}$  are functions defined on  $U \cap U'$ , and at any point  $x \in U \cap U'$ ,  $a_{ij} \in SO(3)$  (Yano and Ako, 1972; Ishihara, 1974).

By using the definition of torsion for primed coordinates, Equation 4 can be written as:

$$[V, V] = [F', F'] + [G', G'] + [H', H']. \tag{8}$$

We now compute torsion tensor term by term as follows:

$$[F', F'](X, Y) = a_{11}^2[F, F](X, Y) + a_{11}a_{12}[F, G](X, Y) + a_{11}a_{13}[F, H](X, Y) \\ + a_{12}a_{12}[G, F](X, Y) + a_{12}^2[G, G](X, Y) + a_{12}a_{13}[G, H](X, Y) \\ + a_{13}a_{13}[H, F](X, Y) + a_{12}a_{13}[H, G](X, Y) + a_{13}^2[H, H](X, Y), \tag{9}$$

$$[G', G'](X, Y) = a_{21}^2[F, F](X, Y) + a_{21}a_{22}[F, G](X, Y) + a_{21}a_{23}[F, H](X, Y) \\ + a_{22}a_{22}[G, F](X, Y) + a_{22}^2[G, G](X, Y) + a_{22}a_{23}[G, H](X, Y) \\ + a_{23}a_{23}[H, F](X, Y) + a_{22}a_{23}[H, G](X, Y) + a_{23}^2[H, H](X, Y), \tag{10}$$

and

$$[H', H'](X, Y) = a_{31}^2[F, F](X, Y) + a_{31}a_{32}[F, G](X, Y) + a_{31}a_{33}[F, H](X, Y) \\ + a_{32}a_{32}[G, F](X, Y) + a_{32}^2[G, G](X, Y) + a_{32}a_{33}[G, H](X, Y) \\ + a_{33}a_{33}[H, F](X, Y) + a_{32}a_{33}[H, G](X, Y) + a_{33}^2[H, H](X, Y). \tag{11}$$

By taking into account coordinate transformations of the local bases we see that the torsions  $[F, G]$ ,  $[G, F]$ ,  $[F, H]$ ,  $[H, F]$ ,  $[G, H]$ , and  $[H, G]$  are needed to be calculated. The torsion tensor  $[F, G]$  for any vector fields  $(X, Y)$  on  $M$  is:

$$[F, G](X, Y) = [FX, GY] + [GX, FY] + FG[X, Y] + GF[X, Y] \\ - F[X, GY] - F[GX, Y] - G[X, FY] - G[FX, Y], \tag{12}$$

and similarly, the tensors  $[G, F]$ ,  $[F, H]$ ,  $[H, F]$ ,  $[G, H]$  and  $[H, G]$  are obtained as follows

$$[G, F](X, Y) = [GX, FY] + [FX, GY] + GF[X, Y] + FG[X, Y] - G[X, FY] - G[FX, Y] - F[X, GY] - F[GX, Y], \quad (13)$$

$$[F, H](X, Y) = [FX, HY] + [HX, HY] + FH[X, Y] + HF[X, Y] - F[X, HY] - F[HX, Y] - H[X, FY] - H[FX, Y], \quad (14)$$

$$[H, F](X, Y) = [HX, FY] + [FX, HY] + HF[X, Y] + FH[X, Y] - H[X, FY] - H[FX, Y] - F[X, HY] - F[HX, Y], \quad (15)$$

$$[G, H](X, Y) = [GX, HY] + [HX, GY] + GH[X, Y] + HG[X, Y] - G[X, HY] - G[HX, Y] - H[X, GY] - H[GX, Y], \quad (16)$$

$$[H, G](X, Y) = [HX, GY] + [GX, HY] + HG[X, Y] + GH[X, Y] - H[X, GY] - H[GX, Y] - G[X, HY] - G[HX, Y]. \quad (17)$$

Then, substituting Equations 9-11 in Equation 8, we find

$$\begin{aligned} [F', F'] + [G', G'] + [H', H'] &= (a_{11}^2 + a_{21}^2 + a_{31}^2)[F, F] \\ &+ (a_{11}a_{12} + a_{21}a_{22} + a_{31}a_{32})[F, G] + (a_{11}a_{13} + a_{21}a_{23} + a_{31}a_{33})[F, H] \\ &+ (a_{12}a_{12} + a_{22}a_{22} + a_{32}a_{32})[G, F] + (a_{12}^2 + a_{22}^2 + a_{32}^2)[G, G] \\ &+ (a_{12}a_{13} + a_{22}a_{23} + a_{32}a_{33})[G, H] + (a_{13}a_{13} + a_{23}a_{23} + a_{33}a_{33})[H, F] \\ &+ (a_{22}a_{23} + a_{32}a_{33} + a_{12}a_{13})[H, G] + (a_{13}^2 + a_{23}^2 + a_{33}^2)[H, H]. \end{aligned} \quad (18)$$

Since  $a_{ij} \in \text{SO}(3)$ , then  $a_{11}^2 + a_{21}^2 + a_{31}^2 = 1$ ,  $a_{12}^2 + a_{22}^2 + a_{32}^2 = 1$ ,  $a_{13}^2 + a_{23}^2 + a_{33}^2 = 1$ , and the other components are  $a_{11}a_{12} + a_{12}a_{22} + a_{31}a_{32} = 0$ ,  $a_{11}a_{13} + a_{21}a_{23} + a_{31}a_{33} = 0$ ,  $a_{12}a_{13} + a_{22}a_{23} + a_{32}a_{33} = 0$ .

So, we find

$$[F', F'] + [G', G'] + [H', H'] = [F, F] + [G, G] + [H, H] \quad (19)$$

which shows that  $V$  is independent of the choice of bases.

We now consider an almost quaternionic manifold  $M$  having an integrable distribution  $P$  with an almost quaternionic structure  $V$  and we let  $H$  denote the division algebra of quaternions by the isomorphism  $R^{4m} \rightarrow H^m$ :

$$(x_1, \dots, x_{4m}) \mapsto (q_1, \dots, q_m); \quad q_m = x_a + x_{m+a}i + x_{2m+a}j + x_{3m+a}k; \quad 1 \leq a \leq m.$$

At  $x \in M$ , for  $q = a1 + bi + cj + dk \in H$ , and

$X \in P(x)$ , defining  $Xq$  as  $Xq = aX + bF(X) + cG(X) + dH(X)$ , we see that  $P(x)$  can be made into a quaternionic right vector space. If  $\{X_1, X_2, \dots, X_m\}$  is a basis of  $P(x)$  as a quaternionic vector space, then  $\{X_1, \dots, X_m, FX_1, \dots, FX_m, GX_1, \dots, GX_m, HX_1, \dots, HX_m\}$  is a basis of  $P(x)$  regarded as a real vector space. Thus, if  $m$  is the quaternionic dimension of  $P(x)$ , then the real dimension is  $4m$ , hence rank of  $V$  is a multiple of 4. This shows that  $V$  defines an almost quaternionic structure on the plane field  $P$ , and it is called an almost quaternionic substructure on  $M$  (Stong, 1977; Doğanaksoy, 1992; Doğanaksoy, 1993).

Let  $\{F, G, H\}$  be a basis for  $V$  in some neighborhood  $U$  of  $4m + n$  dimensional manifold  $M$ . It is proved by Stong (1977) that each of  $F, G$  and  $H$  has a constant rank on  $U$ , and from the conditions  $F = GH$ ,  $G = HF$ ,  $H = FG$ , it is observed that their ranks are all equal (Stong, 1977). Also, the rank of  $V$  is defined to be the rank of a basis element on some neighborhood  $U$ . By choosing  $q = 1 + F^2 = I - p$ , where  $I$  denotes the identity operator, it is obtained that

$$p + q = 1, \quad p^2 = p, \quad q^2 = q \quad (20)$$

and that

$$\phi p = p\phi = \phi, \quad \phi q = q\phi = 0, \quad (21)$$

for any cross-section  $\phi$  of  $V$ . This shows that  $p$  and  $q$  are complementary projection operators. Then, there exist two distributions  $P$  and  $Q$  corresponding to  $p$  and  $q$ , respectively. If the rank of  $V$  is  $4m$ , then  $P$  is  $4m$ -dimensional and  $Q$  is  $n$ -dimensional (Doğanaksoy, 1992).

Let  $g'$  be a Riemannian metric of  $M$ . Define  $g$  to be the tensor field of degree 2 on  $M$  by

$$g(X, Y) = \begin{cases} 0, & X \in P(x), Y \in Q(x) \\ g'(X, Y), & X, Y \in Q(x) \\ g'(X, Y) + g'(FX, FY) \\ + g'(GX, GY) + g'(HX, HY), & X, Y \in P(x) \end{cases} \quad (22)$$

where  $\{F, G, H\}$  is a canonical local basis of  $V$  and  $X, Y \in T_x(M)$ . Since  $g'$  is a Riemannian metric,  $g$  satisfies all the conditions for a Riemannian metric (Doğanaksoy, 1992).

We now consider a Riemannian manifold admitting integrable distribution  $P$  and introduce the shape operator of  $P$ . We give a condition for the shape operator of  $P$  to be quaternionic linear.

**TOTALLY UMBILIC INTEGRAL SUBMANIFOLDS**

Let  $V$  be an almost quaternionic substructure of rank  $4m$  on a Riemannian manifold  $M$  of dimension  $4m + n$  with the metric defined in Equation 22. Let  $P$  and  $Q$  denote the orthogonal plane fields defined by  $V$ , and let  $p, q$  be projections  $T_x(M) \rightarrow P$  and  $T_x(M) \rightarrow Q$ , respectively. Furthermore, let  $V$  be an almost quaternionic structure on  $P$  and  $\{F, G, H\}$  be a local basis for  $V$ . We define the shape operator  $\tilde{L}_Z$  of  $P$  by  $\tilde{L}_Z(X) = -p(\nabla_x Z)$  for any vector fields  $Z \in Q$  and  $X \in P$ , where  $\nabla$  is the covariant derivative operator of the Riemannian connection determined by the metric defined in Equation 22. On the other hand, it is shown that  $\tilde{L}_Z(X)$  is self-adjoint in Özdemir et al. (2002). Here, we define quaternionic linearity of  $\tilde{L}_Z(X)$  so that:  $\tilde{L}_Z$  is quaternionic linear on  $P$  if and only if  $\tilde{L}_Z F = F\tilde{L}_Z$ ,  $\tilde{L}_Z G = G\tilde{L}_Z$ , and  $\tilde{L}_Z H = H\tilde{L}_Z$ . Also, we define conjugate shape operators  $C_1\tilde{L}_Z, C_2\tilde{L}_Z, C_3\tilde{L}_Z$ , satisfying  $C_1\tilde{L}_Z = F\tilde{L}_Z$ ,  $C_2\tilde{L}_Z = G\tilde{L}_Z$  and  $C_3\tilde{L}_Z = H\tilde{L}_Z$ .

**Theorem 2**

Let  $P$  be an integrable distribution with an almost quaternionic structure  $V$ . Conjugate shape operators  $C_1\tilde{L}_Z, C_2\tilde{L}_Z$  and  $C_3\tilde{L}_Z$  are skew-adjoint if and only if  $F\tilde{L}_Z = \tilde{L}_Z F$ ,  $G\tilde{L}_Z = \tilde{L}_Z G$ , and  $H\tilde{L}_Z = \tilde{L}_Z H$ . That is, they are quaternionic linear.

**Proof**

Assume  $C_1\tilde{L}_Z, C_2\tilde{L}_Z$  and  $C_3\tilde{L}_Z$  are skew-adjoint. Using Equation 1, we see that  $F, G$  and  $H$  are skew-adjoint. As  $\tilde{L}_Z$  is self-adjoint (Özdemir et al., 2002), we get:

$$(C_1\tilde{L}_Z)^* = (F\tilde{L}_Z)^* = \tilde{L}_Z^* F^* = -\tilde{L}_Z F.$$

Since  $C_1\tilde{L}_Z$  is assumed to be skew-adjoint, we have

$$(C_1\tilde{L}_Z)^* = -C_1\tilde{L}_Z = -F\tilde{L}_Z,$$

which implies that  $\tilde{L}_Z F = F\tilde{L}_Z$ . Similarly, we see that  $\tilde{L}_Z G = G\tilde{L}_Z$  and  $\tilde{L}_Z H = H\tilde{L}_Z$ . Conversely, by the assumption, if  $F\tilde{L}_Z = \tilde{L}_Z F$  then we have

$$(C_1\tilde{L}_Z)^* = (F\tilde{L}_Z)^* = \tilde{L}_Z^*(F)^* = -\tilde{L}_Z F \tag{23}$$

$$= -F\tilde{L}_Z = -C_1\tilde{L}_Z. \tag{24}$$

In a similar way, since  $G\tilde{L}_Z = \tilde{L}_Z G$ , and  $H\tilde{L}_Z = \tilde{L}_Z H$ , we get  $(C_2\tilde{L}_Z)^* = -(C_2\tilde{L}_Z)$  and  $(C_3\tilde{L}_Z)^* = -(C_3\tilde{L}_Z)$ . That is,  $C_1\tilde{L}_Z, C_2\tilde{L}_Z$  and  $C_3\tilde{L}_Z$  are skew-adjoint.

**Theorem 3**

Let  $P$  be an integrable distribution with an almost quaternionic structure  $V$ . If the integral submanifolds are totally umbilic, then the conjugate shape operators  $C_1\tilde{L}_Z, C_2\tilde{L}_Z$  and  $C_3\tilde{L}_Z$  are skew-adjoint.

**Proof**

Let  $\tilde{L}_Z = \lambda I$  where  $\lambda \in P$ , that is, the integral submanifolds are totally umbilic. By Proposition 1, we have

$$F(\lambda) = (\lambda)F, G(\lambda) = (\lambda)G, \text{ and } H(\lambda) = (\lambda)H.$$

Then, we obtain

$$(C_1\tilde{L}_Z)^* = (F\tilde{L}_Z)^* = (F(\lambda I))^* = (\lambda I)(F)^* = -(\lambda)F = -F(\lambda) = -F(\tilde{L}_Z) \tag{25}$$

which shows that the conjugate shape operator  $C_1\tilde{L}_Z$  is skew-symmetric. Similar results can be obtained for the tensors  $G$  and  $H$ .

**Theorem 4**

Let  $P$  be an integrable distribution. Integral submanifolds

are totally umbilic if and only if  $\tilde{L}_Z$  is self-adjoint,  $\tilde{L}_Z$  is quaternionic linear, and every quaternionic subbundle of  $P$  is  $\tilde{L}_Z$  invariant for every vector field  $Z \in Q$ , where  $Q$  denote the orthogonal plane fields defined by  $V$ .

**Proof**

( $\Rightarrow$ ) Assume that integral submanifolds are totally umbilic, that is,  $\tilde{L}_Z = \lambda I$ ,  $\lambda \in P$ . We have  $\langle \tilde{L}_Z X, Y \rangle = \langle \lambda X, Y \rangle = \langle X, \lambda Y \rangle = \langle X, \tilde{L}_Z Y \rangle$ , implying that  $\tilde{L}_Z = \tilde{L}_Z^*$ .

Since integral submanifolds are totally umbilic, that is,  $\tilde{L}_Z = \lambda I$ , then  $(\lambda I)F = F(\lambda I)$ ,  $(\lambda I)G = G(\lambda I)$  and  $(\lambda I)H = H(\lambda I)$ . This shows that  $\tilde{L}_Z$  is quaternionic linear. We now take any quaternionic subbundle  $R$  of  $P$ , ( $R \subset P$ ). For any  $X \in R$ , we get  $\tilde{L}_Z(X) = \lambda X$  which concludes that  $\tilde{L}_Z(X)$  is in  $R$ .

( $\Leftarrow$ ) Conversely, we assume that  $\tilde{L}_Z = \tilde{L}_Z^*$ ,  $\tilde{L}_Z F = F \tilde{L}_Z$ ,  $\tilde{L}_Z G = G \tilde{L}_Z$ , and  $\tilde{L}_Z H = H \tilde{L}_Z$  for any quaternionic subbundle  $R$  of  $P$ ,  $X \in R$  implies that  $\tilde{L}_Z(X) \in R$ .

Assume for a moment that  $\tilde{L}_Z$  is not totally umbilic, that is,  $\tilde{L}_Z \neq \lambda I$ . Since  $\tilde{L}_Z$  is self-adjoint, it has eigenvalues. Let  $\lambda$  and  $\mu$  be two real distinct eigenvalues corresponding eigenvectors  $X$  and  $Y$  such as  $\tilde{L}_Z X = \lambda X$ ,  $\tilde{L}_Z Y = \mu Y$ . Let  $R$  be the quaternionic subbundle of  $P$  spanned by  $X + Y$ . We observe that  $\tilde{L}_Z(X + Y) = (\lambda X + \mu Y) \in R$  if and only if  $\lambda = \mu$ . Hence, if  $\tilde{L}_Z$  is self adjoint, quaternionic linear, and  $R$  is  $\tilde{L}_Z$  invariant, then  $\tilde{L}_Z$  has to be totally umbilic.

**Conclusion**

In this work, by considering Riemannian manifolds admitting integrable distribution  $P$  with an almost quaternionic structure  $V$ , we show that the torsion tensor of  $V$  is independent of choice of the bases. We introduce the shape operator  $\tilde{L}_Z$  and conjugate shape operators

$C\tilde{L}_Z$  of  $P$  and prove that the conjugate shape operators are quaternionic linear if and only if the conjugate shape operators are skew-adjoint. Furthermore, we prove that integral submanifolds are totally umbilical if and only if the shape operator  $\tilde{L}_Z$  is self-adjoint, quaternionic linear, and every quaternionic subbundle of  $P$  is  $\tilde{L}_Z$  invariant for every vector field in the orthogonal plane fields defined by  $V$  under a suitable metric.

**ACKNOWLEDGEMENTS**

Author would like to thank the referees for their valuable suggestions.

**REFERENCES**

Alagöz Y, Oral KH, Yüce S (2012). Split Quaternion Matrices, Miskolc Mathematical Notes. 13:223-232.  
 Doğanaksoy A (1992). Almost Quaternionic Substructures. Turkish J. Math. 16:109-118.  
 Doğanaksoy A (1993). On Plane Fields With An Almost Complex Structure. Turk. J. Math. 17:11-17.  
 Ishihara S (1974). Quaternion Kahlerian Manifolds. J. Diff. Geom. 9:483-500.  
 Kirichenko VF, Arseneva OE (1997). Differential geometry of generalized almost quaternionic structures. I, dg-ga/9702013.  
 Kobayashi S, Nomizu K (1963, 1969). Foundations of Differential Geometry, A Wiley-Interscience Publication. 1:2.  
 Özdemir F, Doğanaksoy A, Crasmareanu M (2002). Almost Complex Integral Submanifolds and Totally Umbilic Integral Submanifolds, Memoirs of the scientific sections of the Romanian Academy. Ser. IV(23):45-49.  
 Özdemir F (2006). A Global Condition for the Triviality of an almost quaternionic structure on complex manifolds. Int. J. Pure Appl. Math. Sci. 3(1):1-9.  
 Stong RE (1977). The Rank of an  $f$ -Structure. Kodai Math. Sem. Rep. 29:207-209.  
 Yano K, Ako M (1972). Integrability conditions for almost quaternion structure. Hokaido Math J. 1:63-86.

Full Length Research Paper

# Multiband fractal based reconfigurable antenna with introduction of RF MEMS switches for next generation devices

Paras Chawla\* and Rajesh Khanna

Department of Electronics and Communication Engineering, Thapar University, Patiala, Punjab, India.

Accepted 18 August, 2011

Next generation network's main requirements are compact size and also support to heterogeneous network. Fractal antennas have useful applications in cellular telephone and microwave communications. Video conferencing, streaming video are main applications that are included in next generation networks and requirements for these applications are high data rates require to have high bandwidth. But as size of antenna reduces, bandwidth support also reduces. So it is required to have small size with high bandwidth. Fractal antennas are proposed in this paper for different applications as it is compact and also has good bandwidth. In this paper, we propose a reconfigurable fractal shape antenna for *Ku* and *Ka* band. Its performance analysis shows these antennas are multiband antennas support *Ku* and *Ka* bands and also support mobile terminal applications which are sight to be used in next generation networks. Different number of iteration is performed for its support to different bands. Re-configurability in antenna is another important concept and in this work; the reconfigurability is achieved by using radio frequency microelectromechanical system (RF MEMS) switches.

**Key words:** Meander, RF MEMS switch, reconfigurable antenna, fractal antenna.

## INTRODUCTION

Rapid developments in the wireless communication industry continue to drive the requirements for small, compatible, and affordable reconfigurable antennas and antenna arrays. Reconfigurable multiband antennas are attractive for many military and commercial applications where it is desirable to have a single antenna that can be dynamically reconfigured to transmit and/or receive on multiple frequency bands (Brown, 1998; Weedon et al., 1999; Kiriazi et al., 2003). Such antennas find applications in space-based radar, unmanned aerial vehicles, satellites, electronic intelligence aircraft and many other communications and sensing applications. The technology of design and fabrication of MEMS for RF circuits had a major positive impact on reconfigurable antennas (Cetiner et al., 2003; Chiao et al., 1999). Next

generation network aims at high data rates requires wide bandwidth. Antennas performance in a communication system requires being highly efficient. But today's miniaturization technologies need antennas size to be less as well. Both requirements at a time first for small size and wider bandwidth can be fulfilled by using antenna fractal shape (Song et al., 2004; Wu et al., 2007; Werner and Ganguly, 2003). Re-configurability antenna can be further used to improve overall system performance.

Pattern-reconfigurable antennas can either increase capacity or extend radio coverage by increasing the carrier-to-interference ratio. In this paper, we analyze antennas which explore their potentials for different emerging frequency bands.

Puente et al. (1996; 1998) introduces fractal multiband antenna based on the Sierpinski gasket. Reconfigurability to these fractal antennas will enhance the performance and this reconfigurability is achieved by using RF MEMS. Anagnostou et al. (2006) defines an RF MEMS based self similar shaped reconfigurable antenna which has potential of multiband antenna with small size and reconfigurability. In this paper, proposed antenna with RF MEMS support shows an improvement in insertion loss and isolation loss offered by switches. In this paper, we propose a switch which uses meander shape beam rather than cantilever beam for improvement in scattering parameters. It has wide potential with multiband support for different applications like *Ku* and *Ka* band which is to be sight for different satellite communication (Pacheco et al., 2001). It is also supposed to support mobile terminal applications.

## ANTENNA AND RF MEMS SWITCH DESIGN

Reconfigurability in antennas offers us tunability of frequency, so that we can use single antenna for different range of frequencies. Electric switching proved useful in assuring re-configurability for frequency tuning in antenna. MEMS switches are used in this paper to achieve frequency tuning of antenna. As size and bandwidth requirement is achieved by fractal shape, we propose here fractal shaped reconfigurable antenna which is reconfigured by RF MEMS switch and it supports bands including *Ku*, *Ka* band and also mobile terminal applications.

### RF MEMS switch

MEMS are the integration of mechanical elements, sensors, actuators, and electronics on a common silicon substrate through micro-fabrication technology. The micro-fabrication process normally involves a lithography-based micromachining, fabricated on batch basis, which offers great advantages of low cost when manufacturing in large volume (Rebeiz, 2003). MEMS are also built on high-resistivity gallium arsenide (GaAs) wafers, and quartz substrates using semiconductor micro fabrication technology. From a mechanical point of view, MEMS switches can be a thin metal cantilever, air bridge, or diaphragm; from RF circuit configuration point of view, it can be series connected or parallel connected with an RF transmission line. The contact condition can be capacitive (metal-insulator-metal) or resistive (metal-to-metal), polar ceramics such as (Ba,Sr)TiO<sub>3</sub> - BST and designed to open the line or shunt it to ground upon actuation of the MEMS switch. Each type of switch has certain advantages in performance or manufacturability. Tunable ferroelectrics have great potential applications in tunable microwave devices. Main mechanical operations of RF MEMS switches depends mainly on spring constant of

material used, that is, *k*. We always require to have less *k*, that is, less stiff material because the deflection of beam depends on spring constant *k* and we need more deflection with given force for a given RF MEMS switch. In this paper, we have used Serpentine flexure type meander shape to lower the *k* value.

Calculation for spring constant for meander shaped beam (Rebeiz, 2003), is given as:

Serpentine flexure

$$k \approx \frac{48GJ}{l_a^2 \left( \frac{GJ}{EI_x} l_a + l_b \right) n^3} \quad \text{for } n \gg \frac{3l_b}{\frac{GJ}{EI_x} l_a + l_b} \quad (1)$$

where *n* is the number of meanders in the serpentine flexure,  $G = E/2(1+\nu)$  is the torsion modulus,  $I_x = wt^3/12$  is the moment of inertia, *E* = elasticity,  $\nu$  = poison ratio and the torsion constant is given by

$$J = \frac{1}{3} t^3 w \left( 1 - \frac{192}{\pi^5} \frac{t}{w} \sum_{i=1, \text{odd}}^{\infty} \frac{1}{i^5} \tanh\left(\frac{i\pi w}{2t}\right) \right) \quad (2)$$

For the case where  $l_a \gg l_b$ , the spring constant of the serpentine flexure becomes

$$k \approx 4Ew(t/(nl_a)^3) \quad (3)$$

## DESIGN OF A COPLANAR WAVEGUIDE

Coplanar waveguide (CPW) is a one-sided three-conductor transmission line. Coplanar waveguide have two grounds in the same plane of center conductor, reducing the coupling effects and allows for easy inclusion of series and shunt elements. Since microwave integrated circuits are basically coplanar in structure, coplanar waveguide lines are used widely as circuit elements and as interconnecting lines. At millimeter-wave frequencies, coplanar waveguide offers the potential of lower conductor and radiation losses as compared to microstrip lines (Payne and Weedon, 2000). Coplanar waveguide also allows for varying the dimensions of the transmission line without changing the characteristic impedance.

An approximate formula, for the characteristic impedance of the coplanar waveguide, assuming *t* is small,  $0 < k < 1$ , and  $h \gg w$ , is

$$Z_o = \frac{30 \pi^2}{\sqrt{(\epsilon_r + 1)/2}} \left[ \ln\left(2 \frac{1 + \sqrt{k}}{1 - \sqrt{k}}\right) \right]^{-1} \text{ohms} \quad (4)$$

where  $k = \frac{w}{w+2s}$  and *w* = center strip width; *s* = slot width;  $\epsilon_{re}$  = relative dielectric constant of the dielectric substrate.



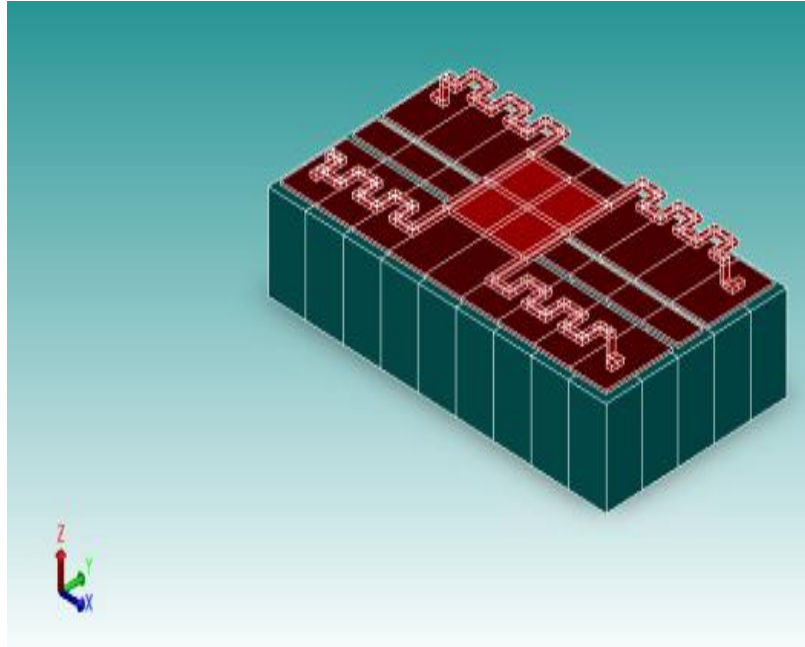


Figure 1. Serpentine flexure beam based RF MEMS switch.

An empirical equation for effective relative dielectric constant  $\epsilon_{re}$  is given as

$$\epsilon_{re} = \frac{\epsilon_r + 1}{2} \left[ \tanh \left( 1.785 \log \left( \frac{h}{w} + 1.75 \right) + \frac{kw}{h} \left( 0.04 - 0.7k + (1 - 0.1\epsilon_r) \frac{(0.25 + k)}{100} \right) \right) \right] \quad (5)$$

As shown in Figure 1, the silicon substrate of  $\epsilon_r = 11.8$  was chosen, and CPW center conductor width  $w = 2 \mu\text{m}$  and ground spacing  $s = 0.8 \mu\text{m}$ , nearly thickness is 0.5 mm and nearly infinite compared to width. The outer CPW ground wave conductor width is 14  $\mu\text{m}$ . The effective dielectric constant is 4.4. Microwave parameters that should be optimized for any RF switch are the insertion loss, isolation, and switching frequency and return loss (Reid, 1999; Smith, 1999). The insertion loss is due to mismatch the characteristic impedance of the line and switch. The contact resistance and beam metallization loss will also contribute to the insertion loss. Switch influence on these microwave parameters will be discussed subsequently.

**ACTIVATION MECHANISM FOR ELECTROSTATIC ACTUATION**

When the voltage is applied between a fixed-fixed or cantilever beam and the pull down electrode, an electrostatic force is induced on the beam, the electrostatic force applied to the beam is found by considering the power delivered to a time-dependent capacitance and is given by,

$$F_e = \frac{1}{2} V^2 \frac{dC(g)}{dg} = -\frac{1}{2} \frac{\epsilon_0 W w V^2}{g^2} \quad (6)$$

where  $V$  is the voltage applied between the beam and electrode.  $W$  is the electrode area.

The electrostatic force is approximated as being distributed evenly across the beam section above the electrode. Equating the applied electrostatic force with the mechanical restoring force due to the stiffness of the beam ( $F = kx$ ),

$$\frac{1}{2} \frac{\epsilon_0 W w V^2}{g^2} = k(g - g_0) \quad (7)$$

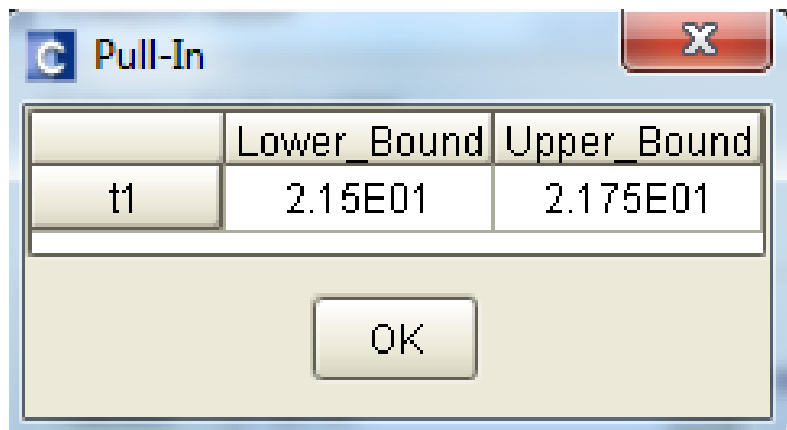
where  $g_0$  is the zero-bias bridge height. At  $(2/3g_0)$ , the increase in the electrostatic force is greater than the increase in the restoring force, resulting in the beam position becoming unstable and collapse of the beam to the down-state position. The pull-down (also called pull-in) voltage is found to be

$$V_p(V) = V \left( \frac{2g_0}{3} \right) = \sqrt{\frac{8k}{27\epsilon_0 W \cdot w} g_0^3} = \sqrt{\frac{8k}{27\epsilon_0 A} g_0^3} \quad (8)$$

As shown in Equation (8), the pull down voltage depends on the spring constant of beam structure, and, beam gap  $g_0$  and electrode area  $A$ . To reduce the actuation voltage, the key is beam structure of low spring constant  $k$ . The pull-in voltage was investigated in terms of beam structure (different  $k$ ), beam thickness, gap and beam materials.

**Table 1.** Parameters for capacitive RF MEMS shunt switch.

Parameter	Value	Parameter	Value
Length ( $\mu\text{m}$ )	160	Actuation area ( $\mu\text{m}^2$ )	20 * 80
Width ( $\mu\text{m}$ )	80	Actuation voltage (V)	21.5 V (20-30 V)
Height ( $\mu\text{m}$ )	2	$C_d$ (pF)	50
Membrane type	Aluminium (film)	Poision ratio	3.0e-001
Thickness ( $\mu\text{m}$ )	0.5	Young's modulus	7.7e+004
Residual stress (MPa)	0	Isolation (dB) > 20 GHz	20 dB
Spring constant (Nm)	10-50	Isolation (dB) 20-55 GHz	35 dB
Holes ( $\mu\text{m}$ )	No	Loss (dB) (0.2-55 GHz)	0.2-0.4
Sacrificial layer	BPSG (2 $\mu\text{m}$ )	$C_d$ (pF)	50
Dielectric ( $\text{\AA}$ )	SiN (0.2 $\mu\text{m}$ )		

**Figure 2.** Pull-in voltage for capacitive MEMS switch.

## FRACTAL ANTENNA

From the antenna side, microstrip antennas are well known for their features such as low profile, light weight, low cost, conformability to planar and non-planar surfaces, rigid, and easy installation. They are most commonly incorporated into mobile communications devices because of low cost and versatile designs. An emphasis has been given in microstrip antenna structures and reconfigurable aperture (recap), in order to achieve multiple octave tunability. Reconfigurable multiband slot antennas are receiving a lot of attention lately due to the emergence of RF-MEMS switches. In recent years neural networks and genetic algorithms are being used extensively for new reconfigurable multiband antenna designs.

The feature of self-similarity of a fractal antenna can also provide a basis for the design of multiple-frequency antennas. These antennas have the advantage that they radiate similar patterns in a variety of frequency bands. The major predecessor is the widely studied Sierpinski gasket (Puente et al., 1996, 1998). Benoit Mandelbrot,

the pioneer of classifying this geometry, first coined the term “fractal” in 1975 from the Latin word fractal, which means “broken or irregular fragments”. The various fractals shape that posse self-similarity have been applied to multi-band or miniaturized antenna design. Many fractal geometries such as Sierpinski gasket, Sierpinski carpet, Koch island, Hilbert curve and Minkowski etc has been used in fractal antennas.

## RESULTS AND DISCUSSION

### RF MEMS design and analysis

Table 1 shows the various parameters calculated and measured for meander based RF MEMS switch. Since coventorware software could synthesize the multiply factors, such as electrostatic-forces, pull-down voltages, Young's modulus, and other vector values could be obtained, and the result is intuitionistic. So, we also used coventore software to know the relationship shape, material and actuated voltage of switch. Figure 2 shows

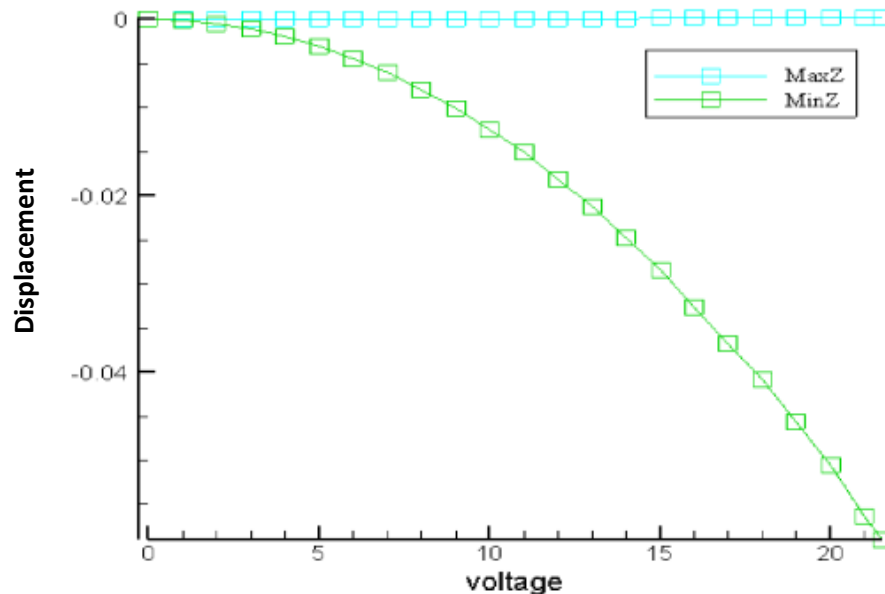


Figure 3. Displacement versus voltage graph for capacitive MEMS switch.

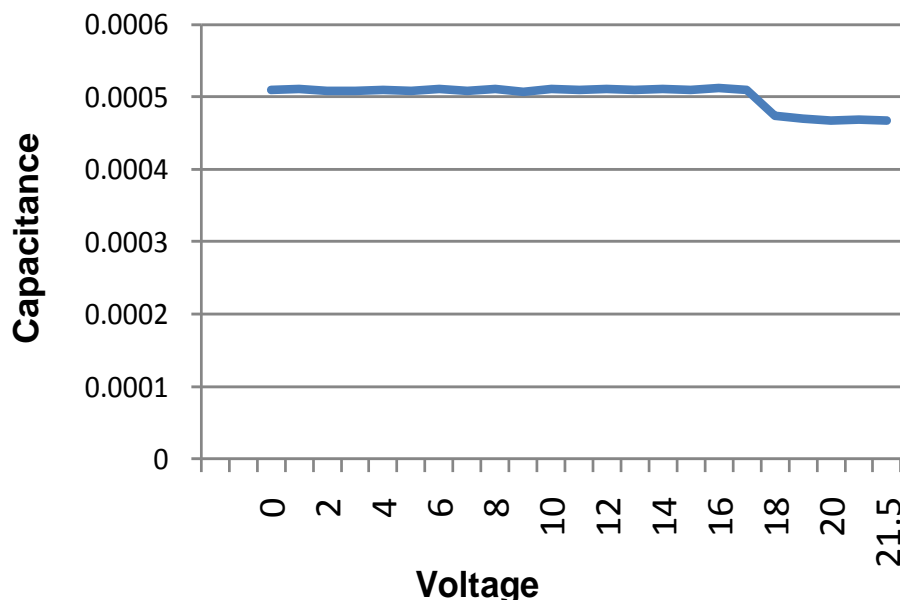
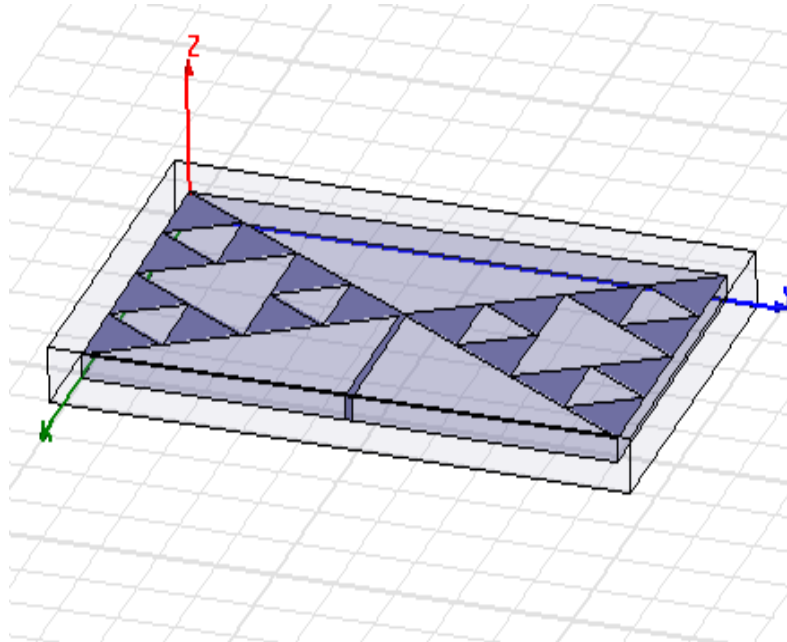


Figure 4. Voltage versus capacitance graph for meander based RF MEMS switch.

the pull-in voltage for RF MEMS switch which ranges from 21.5 to 21.7 V. Variation of displacement, that is, from maximum to minimum z-direction with respect to voltage is shown next in Figure 3, when the switch is electrostatically actuated. The next graph (in Figure 4) shows change in capacitance value with different values of voltages. In off-state, its value is 509.09 μF and at pull-in voltage, that is, in on-state comes out to be 467.9 μF.

### FRACTAL ANTENNA DESIGN AND ANALYSIS

We have design Sierpinski gasket shaped patch on FR4 substrate having dielectric constant is equal to 4.4 and thickness is 1.6 mm. The size of substrate has dimensions of 26 × 30 mm<sup>2</sup>. Figure 5 shows the geometry of designed planar antenna in finite element based electromagnetic solver HFSS software. Figure 6 shows the result of return loss, which show designed



**Figure 5.** Fractal Sierpinski gasket shape for antenna.

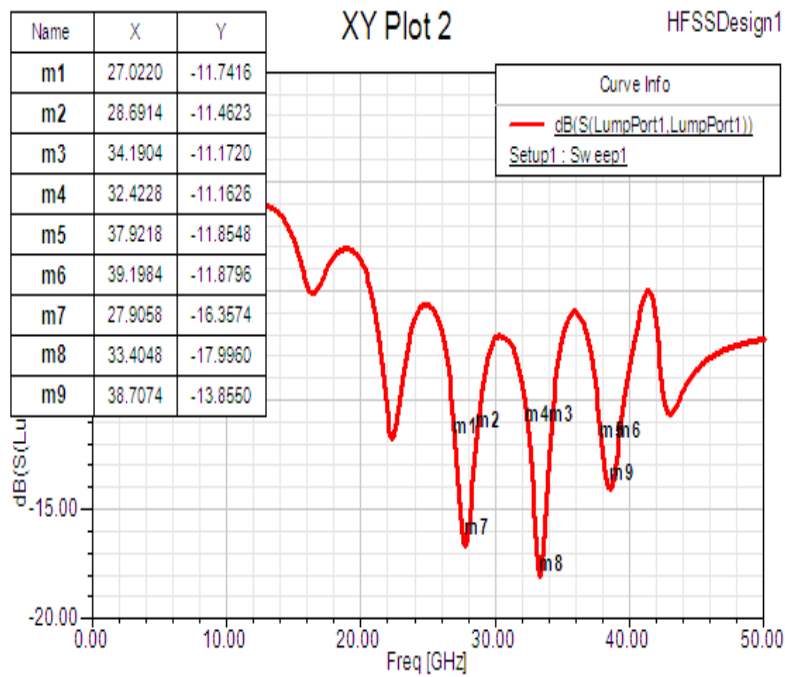


**Figure 6.** Return loss (different mark points to measure bandwidth and resonant frequencies).

antenna are resonating on three bands. Resonant frequencies are marked as 7, 8, 9 m, that is, 27.9056, 33.4048 and 38.7074 GHz, respectively.

The aforementioned multi-band antenna having bandwidth (in GHz) are given as:

$$m2 - m1 = 28.6914 - 27.0220 = 1.6694$$

$$m3 - m4 = 34.1904 - 32.4228 = 1.8676$$

$$m6 - m5 = 39.1984 - 37.9218 = 1.2766$$

Further, as expected from geometry (Figure 7) show that

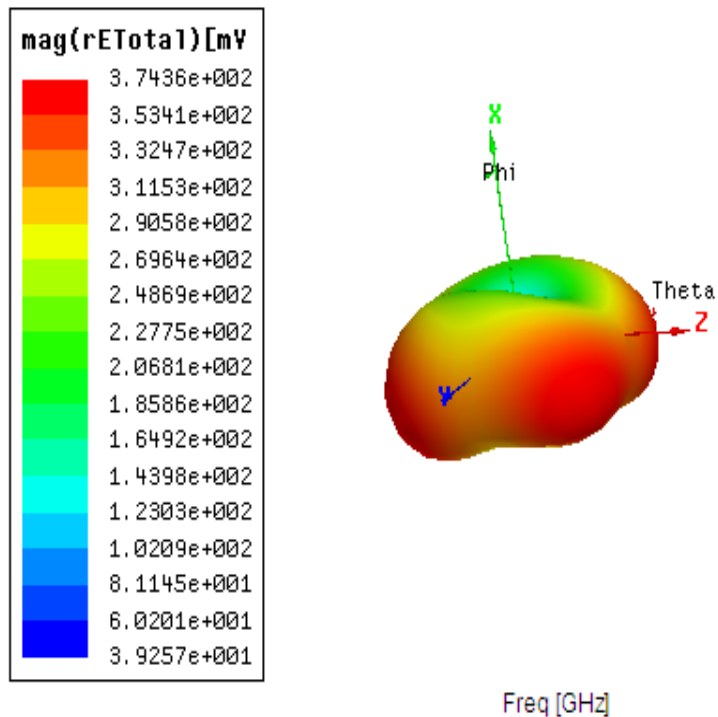


Figure 7. Radiation pattern and polar plot for proposed antenna.

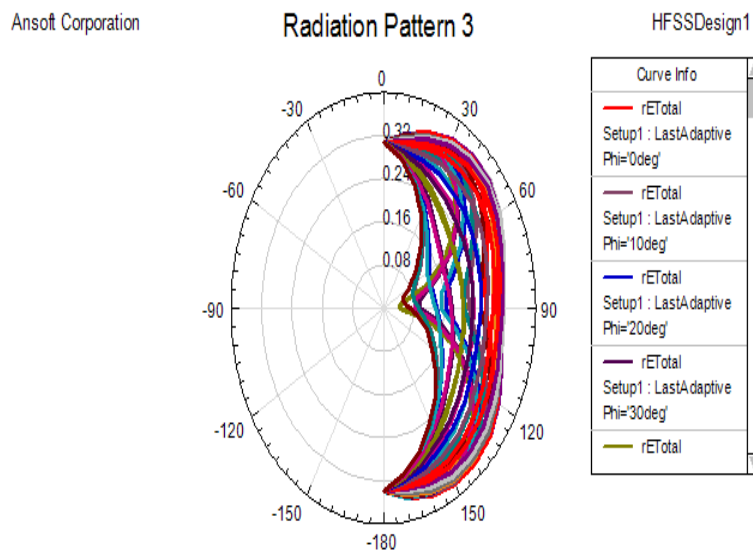


Figure 8. Simulated total normalized electric field intensities of the designed antenna.

antenna radiates equally in all directions and defining the properties of omnidirectional radiation pattern. There is not much difference in radiation patterns of all cases namely, with/without switches of designed antennas. Simulated result of Figure 8 show the total normalized electric field intensities of the designed antenna for all

possible values of  $\phi$  and  $\theta$ . A Table 2 result signifies that at resonant frequencies, the voltage standing wave ratio (VSWR) is less than 2.

Figure 9 to 14 show the geometries and results of return loss for 3rd to 1st iteration. Figure 15 shows the fabricated structure of all antennas for proof of concept.

**Table 2.** VSWR at different selected frequencies shows value less than 2.

S/N	Frequency in (GHz)	VSWR (less than 2)
1	27.218437	1.544088
2	27.316633	1.480224
3	27.414830	1.427252
4	27.513026	1.386671
5	27.611222	1.359630
6	27.709419	1.346528
7	27.807615	1.346741
8	27.905812	1.358768
9	28.004008	1.380758
10	28.102204	1.411079
11	28.200401	1.448609
12	28.298597	1.492732
13	28.396794	1.543145
14	28.494990	1.599635

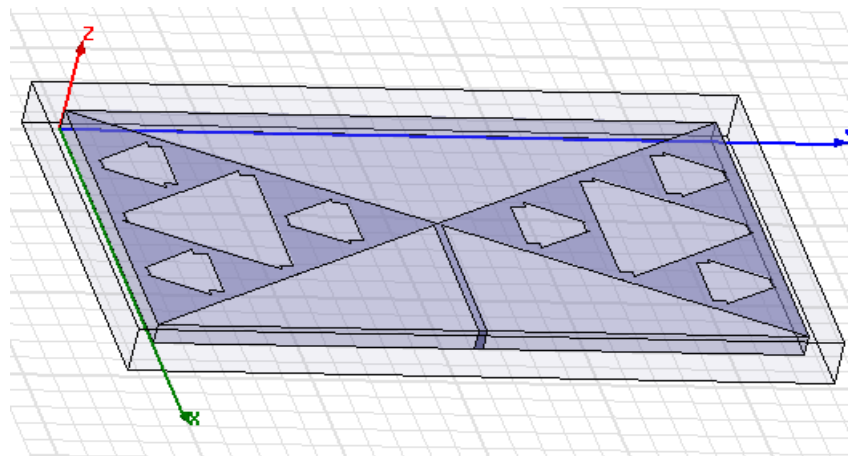


**Figure 9.** 3<sup>rd</sup> iteration Sierpinski fractal antenna.

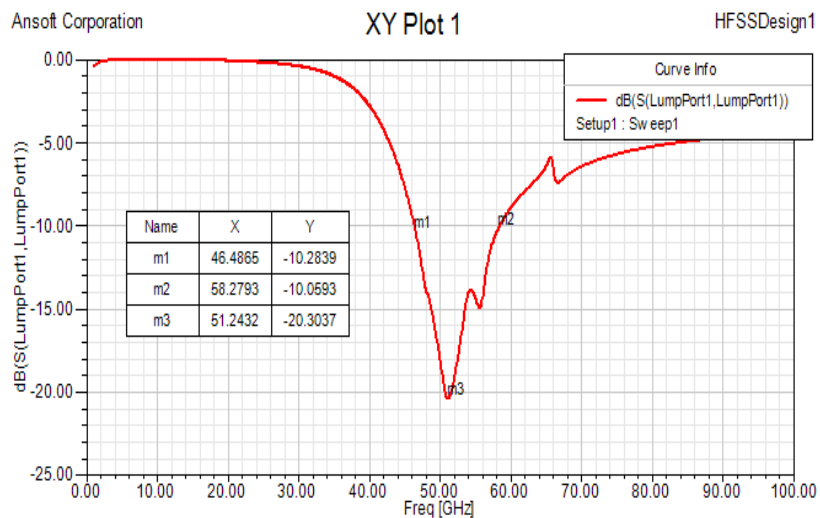


**Figure 10.** Different mark points to measure bandwidth and resonant frequencies.

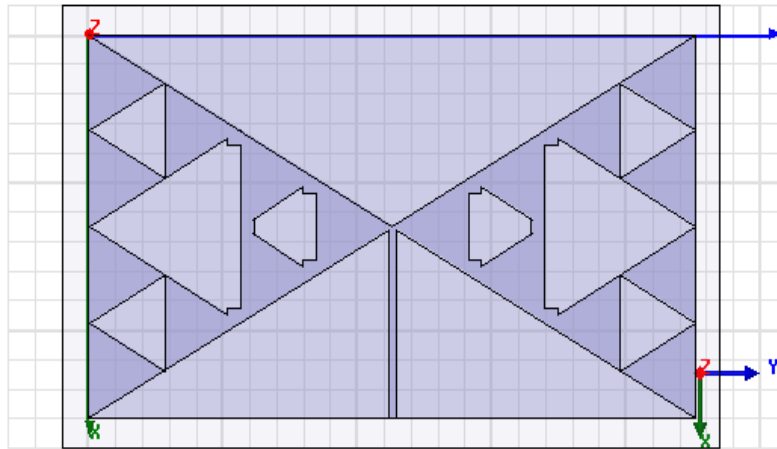


Figure 11. 2<sup>nd</sup> iteration Sierpinski fractal antenna.

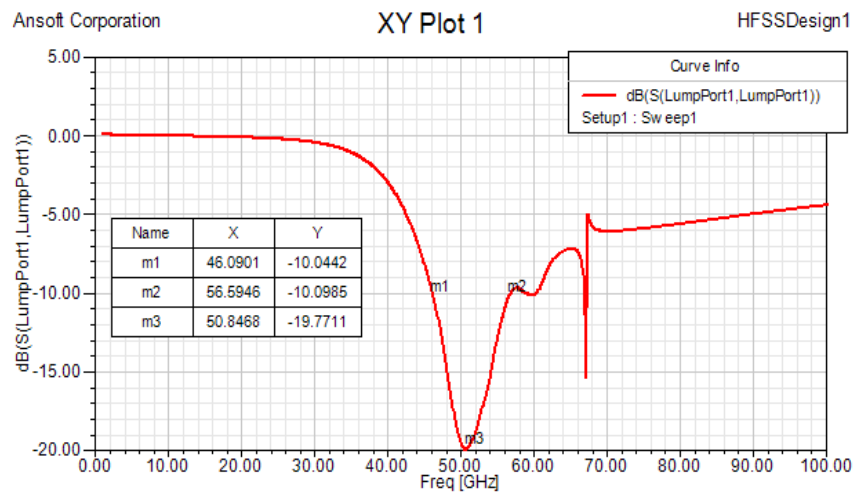


Figure 12. Different mark points to measure bandwidth and resonant frequencies.

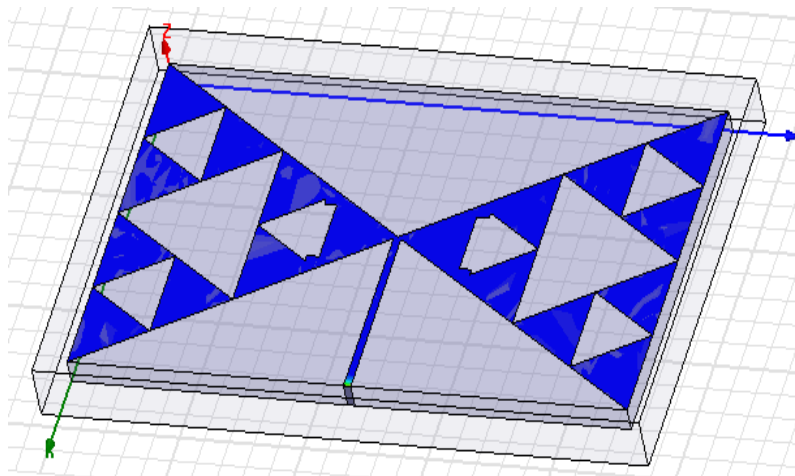
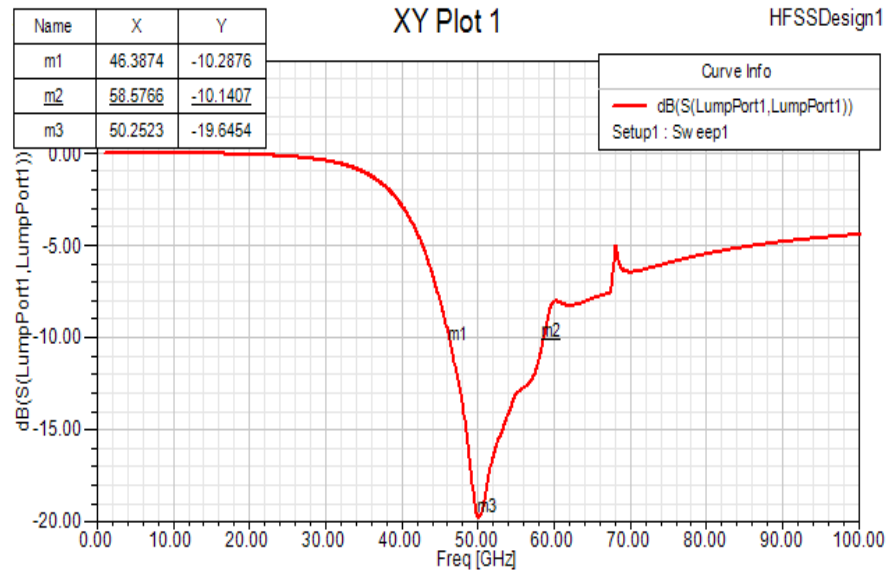
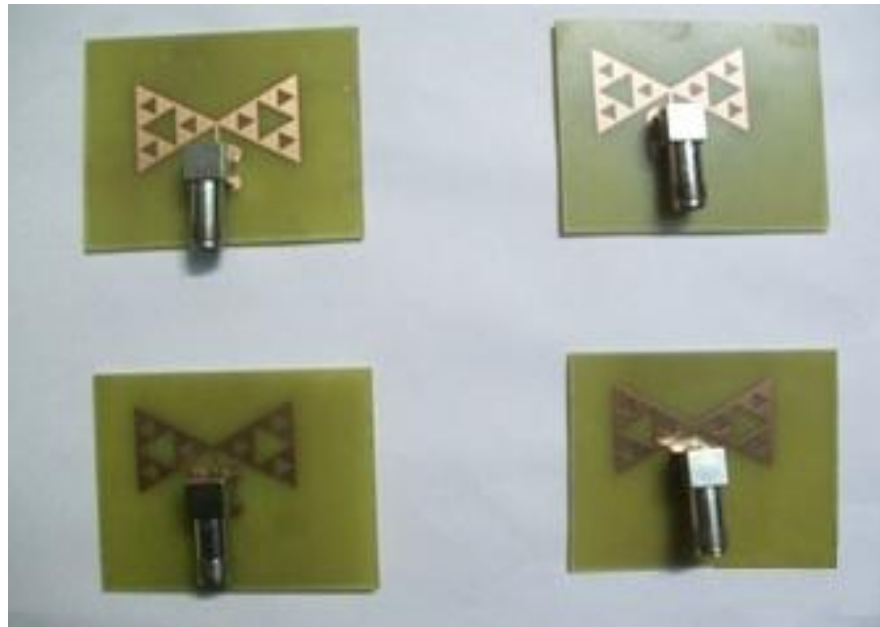


Figure 13. 1<sup>st</sup> iteration Sierpinski fractal antenna.



**Figure 14.** Different mark points to measure bandwidth and resonant frequencies.



**Figure 15.** Fabricated 1<sup>st</sup> to 3<sup>rd</sup> iteration Sierpinski Fractal Antenna.

## Conclusion

In this paper, meander based RF MEMS switches has been designed and simulated for a multiple-frequency fractal antenna. Further, the frequency tunability is achieved by the reconfiguring the antenna electronically or changing the order of iteration. By using MEMS switches, the losses are kept to a minimum. This is very important to obtain high reconfigurability and because the

connection/ disconnection of a switch may lead to mismatched systems. Also, the integration of the switches to the antenna imposes restrictions on the system design. The antenna structure should be compatible with the switch structure and made with specific materials. The dimensions of the switches often cannot be altered and thus put a low-bound in the size of the antenna system and a high-bound in the power the system can handle. This technology can be applied to



many other devices, including tunable filters, other antenna geometries, signal splitters or military applications.

Further in this paper, fractal shaped microstrip antenna is proposed with its return loss, radiation pattern and voltage standing wave ratio (VSWR) as shown in the result. As can be analyze from the result, it shows good characteristics to work for many wireless communication applications. It is offering return loss to be less than -10 dB for many frequencies so supporting multiband applications. For proof of concept open and short path are provided instead of switches. Radiation pattern being omnidirectional and VSWR is also less than 2. As it is microstrip antenna, its size is small. So requirements for multiband support and small size are met with the proposed antenna.

## REFERENCES

- Anagnostou DE, Zheng G, Chryssomallis MT, Lyke JS, Ponchak GE, Papapolymerou J, Christodoulou CG (2006). Design, fabrication, and measurements of an RF-MEMS-based self-similar Reconfigurable Antenna. *IEEE Trans. Antennas Propag.* 54(2):422-432.
- Brown ER (1998). RF-MEMS switches for reconfigurable integrated circuits. *IEEE Trans. Microw. Theory Tech.* 46(11):1868-1880.
- Cetiner BA, Qian JY, Chang HP, Bachman M (2003). Monolithic integration of RF MEMS switches with a diversity Antenna on PCB substrate. *IEEE Trans. Microw. Theory Tech.* 51:332-335.
- Chiao JC, Fu Y, Chio IM, Lisio MD, Lin LY (1999). MEMS reconfigurable Vee antenna. *Proceeding IEEE MTT-S Int. Microw. Symp. Dig.* 4:1515-1518.
- Kiriazis J, Ghali H, Ragaie H, Haddara H (2003). Reconfigurable dual band dipole Antenna on Silicon using series MEMS switches. *Proc. Antennas Propag. Soc. Int. Symp.* 1:403-406.
- Pacheco SP, Peroulis D, Katehi LPB (2001). MEMS single-pole double-throw (SPDT) X and K-band switching circuits. *Microwave Theory Tech -S Int. Microw. Symp.* 1:165-168.
- Payne WJ, Weedon WH (2000). Stripline feed networks for reconfigurable patch antennas. *Proceedings for the Antenna Applications Symposium.* Allerton Park Monticello, Illinois.
- Puente C, Romeu J, Pous R, Garcia X, Benitez F (1996). Fractal multiband antenna based on the Sierpinski gasket. *Electr. Lett.* 32(1):1-2.
- Puente C, Romeu J, Pous R, Cardama (1998). On the Behavior of the Multiband Sierpinski Fractal Antenna. *IEEE Trans. Antennas Propagation.*
- Rebeiz GM (2003). *RF MEMS Theory, Design, and Technology.* New Jersey: John Wiley & Sons Publication.
- Reid JR (1999). An Overview of micro-electro-mechanical systems (MEMS). *Tutorial Session on MEMS for antenna applications antenna applications symposium.* Allerton Park Monticello, Illinois.
- Smith JK (1999). MEMS and advanced radar. *Tutorial session on MEMS for antenna applications. antenna applications symposium.* Allerton Park Monticello, Illinois.
- Song CTP, Hall PS, Ghafouri-Shiraz H (2004). Shorted Fractal Sierpinski Monopole Antenna. *IEEE Trans. Antennas Propag.* 52 (10).
- Wu W, Wang BZ, Yang XS, Zhang Y (2007). A Pattern- Reconfigurable Planar Fractal Antenna and its Characteristic-Mode Analysis. *IEEE Antennas Propag. Mag.* 49(3).
- Werner DH, Ganguly S (2003). An Overview of Fractal Antenna Engineering Research. *IEEE Antennas Prop. Mag.* 45(1):38-57.
- Weedon WH, Payne WJ, Rebeiz GM, Herd JS, Champion M (1999). MEMS-Switched reconfigurable multi-band antenna: Design and modeling. *Proceedings for the 1999 Antenna Applications Symposium.* Allerton Park Monticello, Illinois.

*Full Length Research Paper*

## Synthesis and characterization of nano-hydroxyapatite (n-HAP) using the wet chemical technique

Arunseshan Chandrasekar, Suresh Sagadevan and Arivuoli Dakshnamoorthy\*

Crystal Growth Centre, Anna University, Chennai-600 025, India.

Accepted 8 August, 2013

Hydroxyapatite nanoparticles were synthesized, using a wet chemical technique with diammonium hydrogen phosphate and calcium nitrate tetrahydrate precursors, respectively. The pH of the system was maintained at 10.8 throughout the stirring process, by using 0.1 M sodium hydroxide. The mixture was allowed to remain stirred overnight and a white precipitate was formed. The precipitate was vacuum dried and cleaned with distilled water and ethanol simultaneously three or four times. The prepared powder was used for further characterization. The prepared nano-hydroxyapatite powder was characterized for phase composition, using X-ray diffractometry; elemental dispersive X-ray and Fourier transform infrared spectroscopy. The elemental compositions of the nano-hydroxyapatite were analyzed and confirmed by elemental dispersive X-ray (EDX). The particle size and morphology were studied using the scanning electron microscope (SEM) and transmission electron microscopy (TEM). The particle size of the nano-hydroxyapatite was also analyzed, using the dynamic light scattering (DLS) experiment.

**Key words:** Hydroxyapatite, wet chemical, elemental dispersive X-ray (EDX), Fourier transform infrared spectroscopy (FTIR), scanning electron microscope (SEM), transmission electron microscopy (TEM).

### INTRODUCTION

Tissue engineering is a multidisciplinary science, encompassing diverse fields like materials engineering and molecular biology, in the effort to develop biological substitutes for failing tissues and organs. Tissue engineering thus seeks to replace diseased and damaged tissues of the body. An important factor for the success of tissue engineering is the ability of developing materials, which can interface with tissues structurally, mechanically, and bio functionally (Yang et al., 2001). Many biomaterials lack the desired functional properties to interface with biological systems, in spite of numerous uses of materials in tissue engineering. Thus, developing new materials to reach these issues is necessary. Composites of hydrophilic polymers and inorganic minerals like hydroxyapatite can be good materials for biomedical applications. Bone apposition and differentiation of mesenchymal cells to osteoblasts can

be promoted by the attachment of hydroxyapatite nanoparticles to a polymer surface (Sinha and Guha, 2008). Hydroxyapatite is a significant biomaterial in the health care industry. Its chemical and mineral phases are analogous to those of natural bone and hence, its usage in the field of dentistry and orthopedics has been explored (Zhao and Ma, 2005; Chen et al., 2002; Hornez et al., 2007). Properties like osteoconductivity and osteoinductivity enhance bone regeneration and make hydroxyapatite an important material in tissue engineering (Burg et al., 2000), and its biocompatibility leads to its use as bioactive coating over implants (Wang et al., 2006; Ye et al., 2007). Bone is considered as a nanocomposite of minerals and proteins, and recently nano-level hydroxyapatite has been investigated and demonstrated as having a good impact on cell biomaterial interaction (Elliot, 1994; Webster et al., 2000).

\*Corresponding author. E-mail-arivuoli@gmail.com.

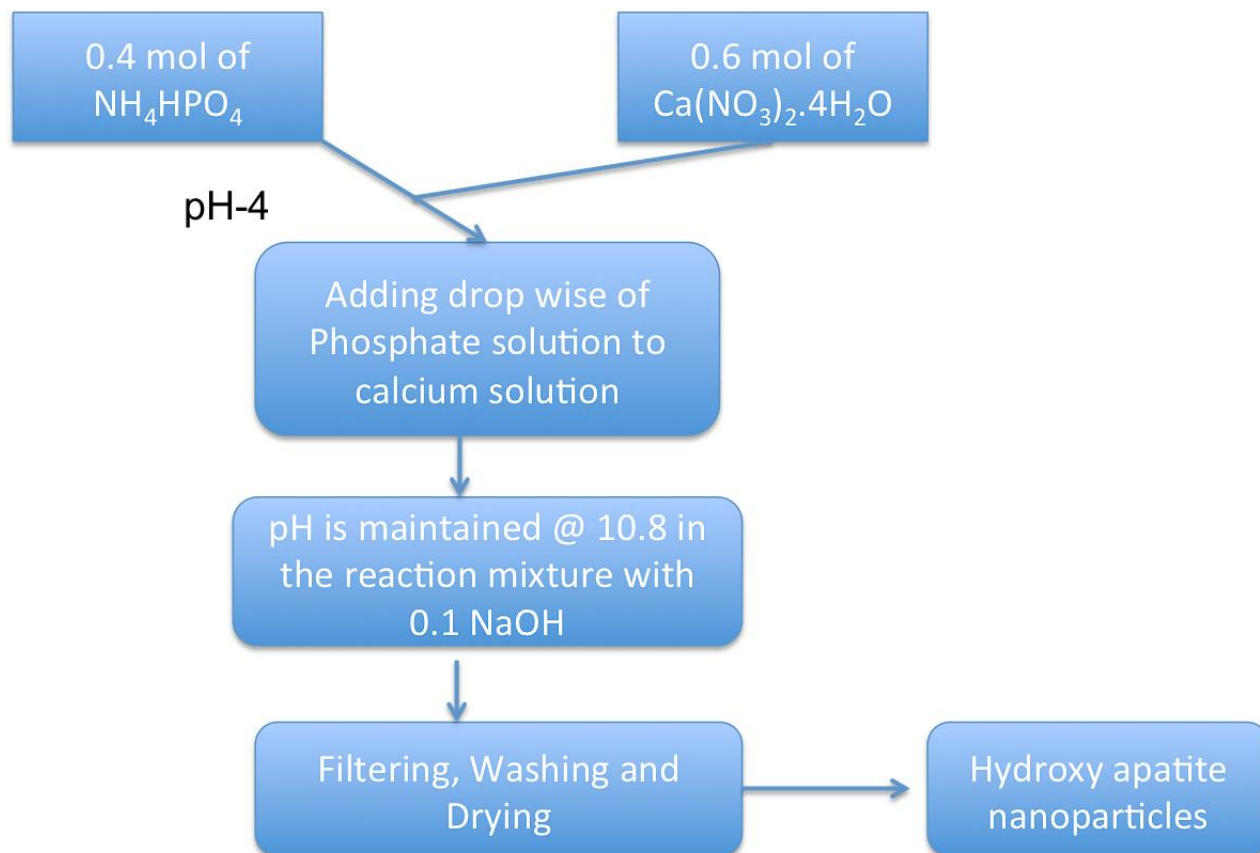


**Figure 1.** Flow chart of hydroxyapatite nanoparticles preparation by wet chemical method.

However, the migration of the nano- hydroxyapatite particles from the implanted site into the surrounding tissues might cause damage to healthy tissue (Miyamoto et al., 1998). To find a solution, composites of nano-hydroxyapatite and polymers were researched to find a material that retained the good properties of nano-hydroxyapatite and prevented the nano- hydroxyapatite particles from migrating. In the present investigation, we report the synthesis and characterization of nano-hydroxyapatite by a wet chemical synthesis technique. The as prepared hydroxyapatite nanoparticles are characterized by X- ray diffraction, Fourier transform infrared spectroscopy (FTIR), elemental dispersive X-ray (EDX) analysis, scanning electron microscopy (SEM), transmission electron microscopy (TEM), and dynamic light scattering (DLS) analysis.

## EXPERIMENTAL PROCEDURES

### Synthesis of hydroxyapatite nanoparticle

Hydroxyapatite nanoparticles were synthesized by the wet chemical method. 500 ml of 0.4 mol of diammonium hydrogen phosphate with pH-4.0 was vigorously stirred in 2 L beaker at room temperature and 500 mL of 0.6 mol calcium nitrate tetrahydrate with

pH=7.4 was added drop-wise over 4 h. The pH of the system was maintained at 10.8 throughout the stirring process, by using 0.1 M sodium hydroxide. The mixture was allowed to remain stirred overnight. A white precipitate was formed. The precipitate was vacuum dried and cleaned with distilled water and ethanol simultaneously for three or four times. The prepared powder was used for further characterization. The schematic presentation of the procedure is given in Figure 1. This precipitation reaction for synthesis of hydroxyapatite nanoparticles was first proposed by Yagai and Aoki, as indicated by Bouyer et al. (2000).

## RESULTS AND DISCUSSION

### XRD analysis

The structural analysis of sample was done by the powder X-ray diffraction. The XRD patterns of the synthesized nano hydroxyapatite are shown in Figure 2. The XRD pattern of nano hydroxyapatite shows sharper peaks which indicate better crystallinity. The peak positions are in good agreement with the JCPDS (896438). As can be seen, hydroxyapatite XRD patterns, with the diffraction peaks, obtained with d-spacing values of  $2.82\text{\AA}$ ,  $2.79\text{\AA}$  and  $2.72\text{\AA}$  and the other d-spacing values match exactly with the hexagonal system with

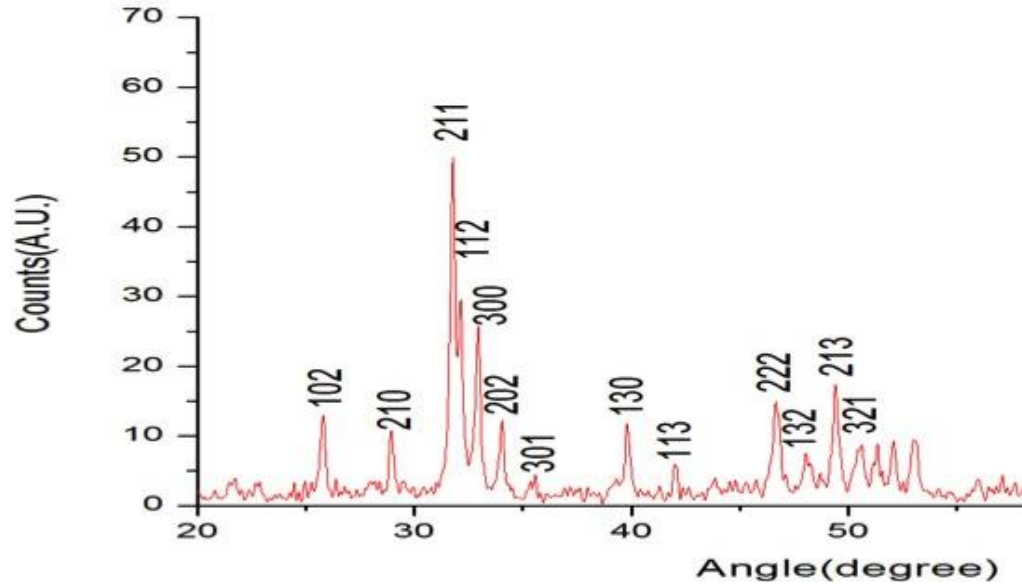


**Figure 2.** XRD spectra of hydroxyapatite nanoparticles.

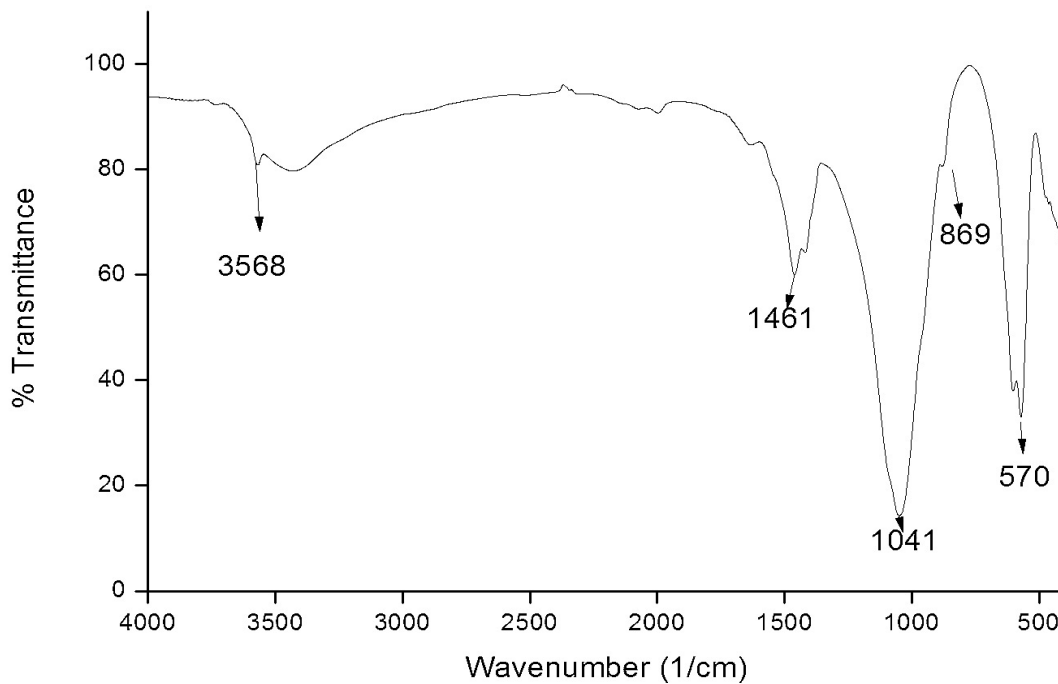


**Figure 3.** FTIR spectrum of nano- hydroxyapatite.

primitive lattice. The results of XRD analysis obtained in the present investigation are in good agreement with the reported results (Bouyer et al., 2000).

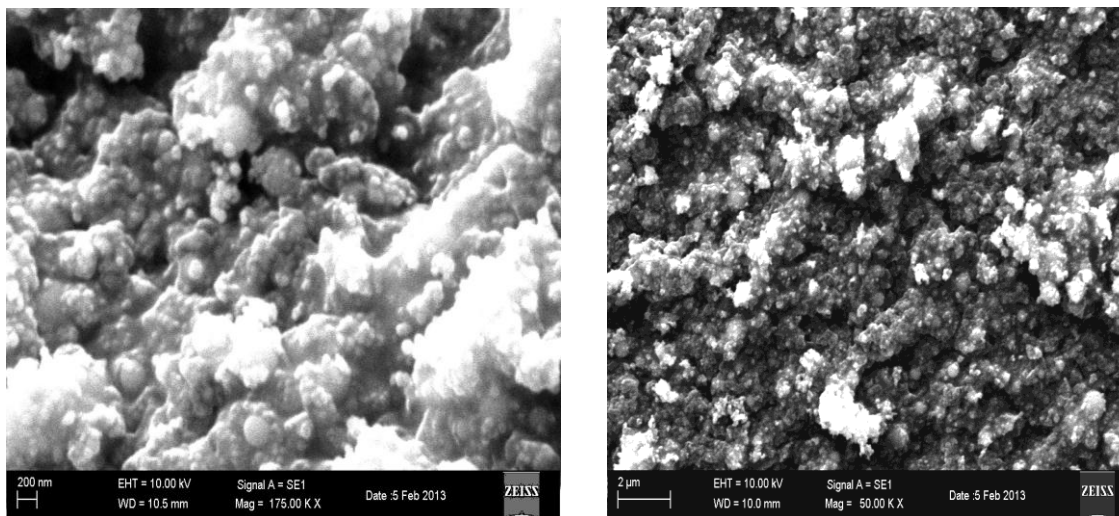
### FTIR analysis

Functional groups associated with hydroxyapatite were

identified by FTIR spectroscopy. The FTIR spectra of the prepared samples are given in Figure 3. The ion stretching vibration around  $3568\text{ cm}^{-1}$  confirms the presence of a hydroxyl group. Likewise, the other stretching vibrations for carbonyl and phosphate groups were also observed as reported earlier (Cengiz et al., 2008). The observed functional groups and their corresponding assignments are presented in Table 1.

**Table 1.** Some important functional group assignments of hydroxyapatite nanoparticles.

Wavenumber $\text{cm}^{-1}$	Stretching mode	Functional group
3568	Ion Stretching	$\text{OH}^-$
1461	Asymmetric stretching	$\text{CO}_3^{2-}$
1041	Asymmetric stretching	$\text{PO}_4^{3-}$
869	Out of plane bending mode	$\text{CO}_3^{2-}$
570	Asymmetric bending vibration	$\text{PO}_4^{3-}$

**Figure 4.** SEM Image of the hydroxyapatite nanoparticle.

The functional groups of the hydroxyapatite powder predicted from FTIR spectra analysis are compared with the results of Choi et al. (2004) for the confirmation.

### SEM analysis

The scanning electron microscope (SEM) was used for the morphological study of nanoparticles of hydroxyapatite. Figure 4 shows the SEM images of the as-prepared hydroxyapatite nanoparticles. The hydroxyapatite nanoparticles formed were highly agglomerated. The agglomeration of the nanoparticles might be because of Ostwald ripening. The spherical shaped particles with clumped distributions are visible from the SEM analysis. The SEM images show the spherical shaped particles as confirmed by Ferraz et al. (2004) for reported results of hydroxyapatite nanoparticles.

### EDX analysis

In Figure 5a and b, and Table 2, the standard EDX spectra recorded on the examined nano-hydroxyapatite

are shown. The presented spectrum shows the Ca/P value of the synthesized nano-hydroxyapatite to be 1.68, which is quite close to the Ca/P ratio of the human bone (Trommer et al., 2007).

### TEM analysis

The structure and morphology of the samples were further confirmed by the TEM and TEM images of the prepared nano-hydroxyapatite, as shown in Figure 6. The transmission electron microscopic analysis confirms the presence of the spherical shape morphology of the prepared hydroxyapatite nanoparticle with the particle size of around 60 to 70 nm (Figure 7). The particle size is also found to be in agreement with the report results of Ferraz et al. (2004).

### DLS studies

Dynamic light scattering (DLS) is an important tool for characterizing the size of nanoparticles in a solution. The DLS measures the light scattered from a laser that passes through a colloidal solution and by analyzing the

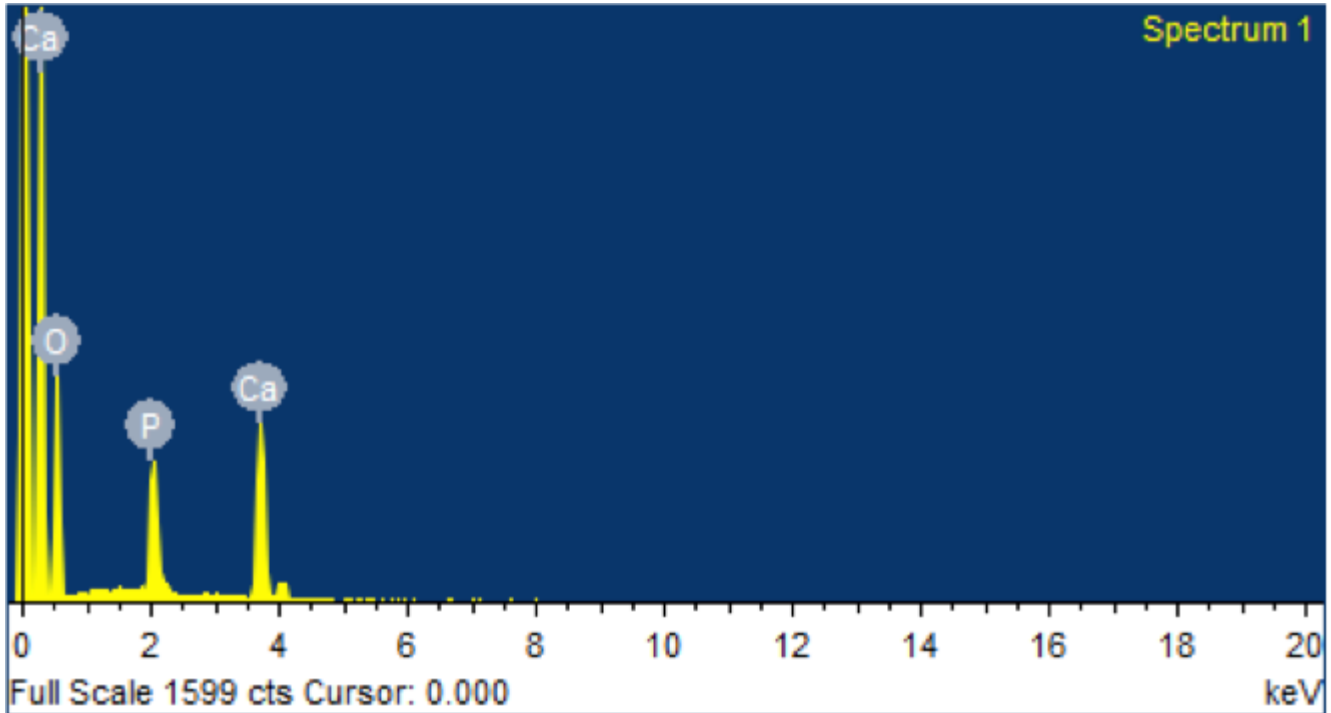


Figure 5a. EDX spectrum of nano-hydroxyapatite.

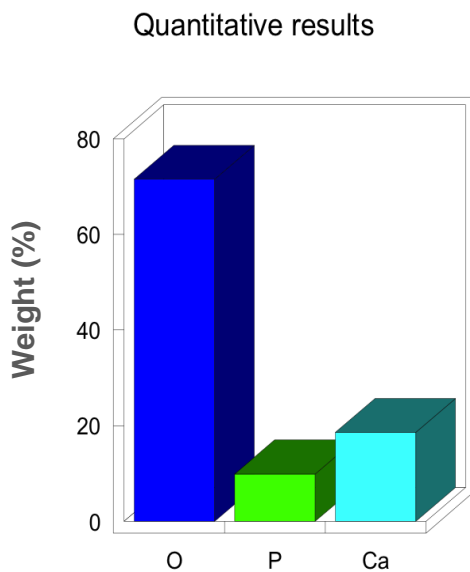


Figure 5b. Chart showing the weight % and quantitative results of EDX spectrum of nano-hydroxyapatite.

modulation of the scattered light intensity as a function of time, the hydrodynamic size of the particles and particle agglomerates can be determined. Larger particles will diffuse slower than smaller particles, and the DLS instrument measures the time dependence of the

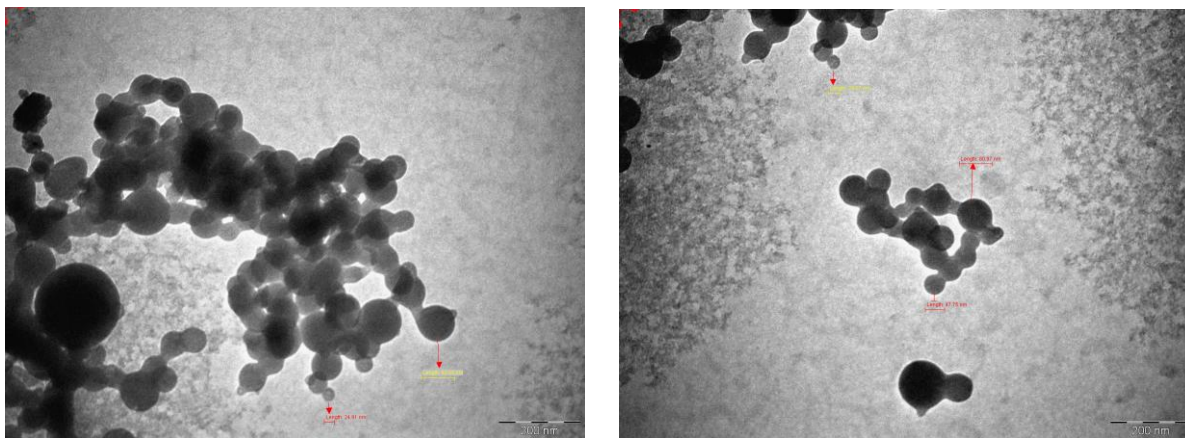
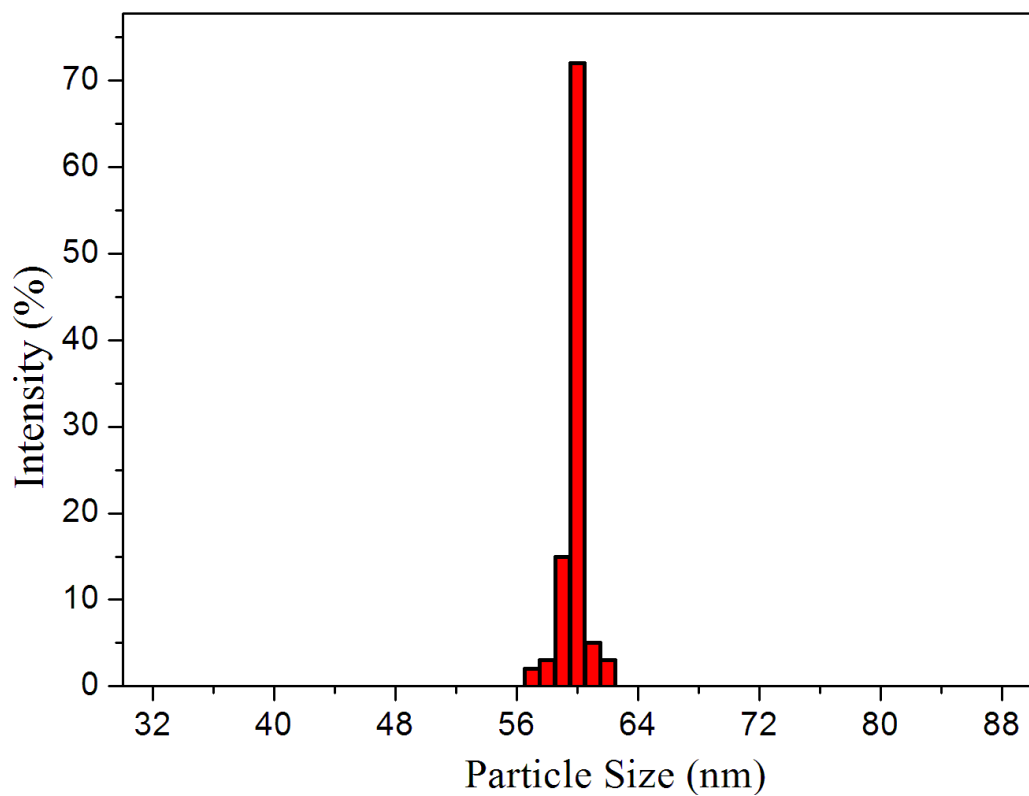
scattered light, to generate a correlation function that can be mathematically linked to the particle size. The DLS is a valuable tool for determining and measuring the agglomeration state of the nanoparticles as a function of time or suspending solution. When the DLS sizing data is compared to the transmission electron microscopy images, the aggregation state of the particles can be determined. In an unagglomerated suspension, the DLS measured diameter will be similar or slightly larger than the TEM size. If the particles are agglomerated, the DLS measurement is often much larger than the TEM size, and can have a high polydispersity index (large variability in the particle size). The dynamic light scattering experiment shows that the particle size distribution is in the range of 50 to 70 nm, which is well supported by the TEM analysis. Dynamic light scattering is used to monitor the size of the precipitating particles and to provide information about their concentration (De Bruyn et al., 2013).

## Conclusion

Nano-hydroxyapatite has been successfully synthesized using the wet chemical technique. The formation of hydroxyapatite nano particles was confirmed by X-ray diffraction (XRD) and Fourier transform infrared spectroscopy (FT-IR). The elemental compositions were examined using the EDX analysis. The size and morphology of the samples were characterized using

**Table 2.** Elemental composition of nano-hydroxyapatite.

Element	App	Intensity	Weight (%)	Weight (%)	Atomic (%)
	Conc.	Conc.		Sigma	
OK	2.26	0.7087	73.52	0.96	85.09
PK	0.56	1.2858	9.88	0.55	6.07
Ca K	0.82	0.9935	16.60	0.70	8.84
Total			100.00		

**Figure 6.** TEM images of hydroxyapatite nanoparticles.**Figure 7.** Particle size of hydroxyapatite nanoparticles.



scanning and transmission electron microscopy (SEM and TEM). The spherical shaped particles were confirmed through the SEM analysis. The transmission electron microscopic analysis confirms the prepared hydroxyapatite nanoparticles with the particle size of around 60 to 70 nm. The particle size of the nano-hydroxyapatite range of 50 to 70 nm was determined using the dynamic light scattering (DLS) experiment which is in good agreement with the TEM analysis.

## ACKNOWLEDGEMENTS

One of the authors (Arunseshan Chandrasekar) acknowledges with thanks to the support rendered by the Council of Scientific and Industrial Research, India for providing him the Senior Research Fellowship (CSIR-SRF).

## REFERENCES

- Bouyer E, Gitzhofer F, Boulos MI (2000). Morphological study of hydroxyapatite nanocrystal suspension. *J. Mater. Sci. Mater. Med.* 11: 523-531.
- Burg KJL, Porter S, Kellam JF (2000). Biomaterial developments in bone tissue engineering. *Biomaterials.* 21:2347-2359.
- Cengiz B, Gokce Y, Yildiz N, Aktas Z, Calimli A (2008). Synthesis and characterization of hydroxyapatite nanoparticles. *Colloids and Surfaces A: Physicochemical and Engineering Aspects*, 322(1-3):29-33.
- Chen F, Wang ZC, Lin CJ (2002). Preparation and characterization of nano-sized hydroxyapatite particles and hydroxyapatite/chitosan nano-composite for use in biomedical materials. *Mater. Lett.* 57(4):858-861.
- Choi D, Marra K, Kumta PN (2004). Chemical synthesis of hydroxyapatite/poly (caprolactone) composite. *Materials Research Bulletin.* 39:417-432.
- De Bruyn JR, Goiko M, Mozaffari M, Bator D, Dauphinee RL (2013). Dynamic light scattering study of inhibition of nucleation and growth of hydroxyapatite crystals by osteopontin. *Plus One.* 8(2):e 56764.
- Elliot JC (1994). Amsterdam: Structure and Chemistry of the Apatites and Other Calcium Orthophosphates. Elsevier Science.111.
- Ferraz MP, Monteiro FJ, Manuel CM (2004). Hydroxyapatite nanoparticles: A review of preparation methodologies. *J. Appl. Biomater. Biomech.* 2:74-80.
- Hornez JC, Chai F, Monchau F, Blanchemain N, Descamps M, Hildebrand HF (2007). Biological and physico-chemical assessment of hydroxyapatite (HA) with different porosity. *Biomol. Eng.* 24:505-509.
- Miyamoto Y, Ishikawa KI, Takechi M, Toh T, Yuasa T, Nagayama M, Suzuki K (1998). Basic properties of calcium phosphate cement containing atelocollagen in its liquid or powder phases. *Biomaterials.* 19:707-715.
- Sinha A, Guha A (2008). Biomimetic patterning of polymer hydrogels with hydroxyapatite nanoparticles. *Mater. Sci. Eng. C.* 29:1330-1333.
- Trommer RM, Santos LA, Bergmann CP (2007). Alternative technique for hydroxyapatite coatings. *Surface Coatings Technol.* 201(24):9587-9593.
- Wang YJ, Chen JD, Wei K, Zhang SH, Wang XD (2006). Surfactant-assisted synthesis of hydroxyapatite particles. *Mater. Lett.* 60:3227-3231.
- Webster TJ, Ergun C, Doremus RH, Siegel RW, Bizios R (2000). Enhanced functions of osteoblasts on nanophase ceramics. *Biomaterials.* 21:1803-1810.
- Yang S, Leong KF, Du Z, Chua CK (2001). The design of scaffolds for use in tissue engineering. Part I. Traditional factors. *Tissue Engineering.* 7:679-689.
- Ye W, Wang XX (2007). Ribbon-like and rod-like hydroxyapatite crystals deposited on titanium surface with electrochemical method. *Mater. Lett.* 61:4062-4065.
- Zhao YF, Ma J (2005). Triblock co-polymer templating synthesis of mesostructured hydroxyapatite. *Micro. Meso. Mater.* 87:110-117.



**UPCOMING CONFERENCES**

**International Conference on Mathematical Modeling in  
Physical Sciences Prague, Czech Republic, September 1-  
5, 2013**



**14th International Conference on Accelerator and  
Large Experimental Physics Control Systems. The Hyatt Regency  
Embarcadero Center San Francisco, California October 6-11,  
2013**



## Conferences and Advert


### **September 2013**

International Conference on Mathematical Modeling in Physical Sciences  
Prague, Czech Republic, September 1-5, 2013

### **October 2013**

14th International Conference on Accelerator and Large Experimental  
Physics Control Systems. The Hyatt Regency Embarcadero Center San  
Francisco, California October 6-11, 2013

# International Journal of Physical Sciences



## *Related Journals Published by Academic Journals*

- *African Journal of Pure and Applied Chemistry*
- *Journal of Internet and Information Systems*
- *Journal of Geology and Mining Research*
- *Journal of Oceanography and Marine Science*
- *Journal of Environmental Chemistry and Ecotoxicology*
- *Journal of Petroleum Technology and Alternative Fuels*

**academicJournals**